Using Phase Response Curves to Understand Neuronal Synchronization and Sleep

by

Timothy Christian George Fink

A dissertation submitted in partial fulfillment
of the requirements for the degree of
Doctor of Philosophy
(Physics)
in The University of Michigan
2012

Doctoral Committee:

Assistant Professor Victoria Booth, co-Chair
Associate Professor Michal R. Zochowski, co-Chair
Professor Leonard M. Sander
Professor Robert S. Savit
Assistant Professor William Charles Stacey

"The important thing is not to stop questioning. Curiosity has its own reason for existing. One cannot help but be in awe when he contemplates the mysteries of eternity, of life, of the marvelous structure of reality. It is enough if one tries merely to comprehend a little of this mystery every day. Never lose a holy curiosity." $\sim$ Einstein

© Timothy Christian George Fink 2012
All Rights Reserved

To Chrissie: I never would have made it to this point without you. And to my parents, who gave me the gift of curiosity.

ACKNOWLEDGEMENTS

The last few years spent working toward my Ph.D. have been the best of my life, and I have a number of people to thank for that. First of all, my wife: thank you, Chrissie, for your encouragement and wisdom throughout this journey. Whenever two paths diverged and I was uncertain of which to take, you were always by my side, helping me to think clearly and bolstering my attitude with the comfort that no matter what happened, we would enjoy the adventure together.

My parents have helped me reach this point through innumerable acts of sacrifice and love, many of which I'm sure I am unaware of. But two things do stand out: the joy of learning that they instilled, and the freedom they gave to pursue my passions. My parents were constantly posing riddles and math problems to me as a child, and they struck a good balance between making it fun while at the same time pushing me to improve. I still remember my mom getting me to count all the way up to 28 (but not a number higher–it was too hard!) in kindergarden. And I remember my dad taking me out to breakfast my senior year of high school to make sure I knew it was all right with him if I deviated from the family tradition by becoming a physicist instead of a physician. Thanks for everything, Mom and Dad.

My two advisors, Michal Zochowski and Victoria Booth, are by far the biggest reason that working toward my Ph.D. has been an enjoyable process. They have guided my investigation of very interesting problems while treating me as a colleague, giving me the freedom to disagree and to explore my own ideas. They have taught me

to communicate scientific ideas efficiently and with excitement, both when writing and giving talks. They have also been enormously helpful with my career, introducing me to many important people in the field and helping me prepare for my first job interview. And through it all, they have been two of the nicest people I know. Thanks so much, Michal and Victoria.

Thanks also to Bill Stacey, who gave me the opportunity to squeeze in one last project before walking out the door. I am fortunate to have worked with my office/lab mates, Dan Maruyama, Sima Mofakham, and Liz Shtrahman. Among many other things, I owe Liz for patiently teaching me experimental techniques and sometimes sharing delicious granola with the office, Dan for taking Quantum Information with me and always being willing to talk Michigan football, and Sima for never failing to lift our spirits with a smile and a piece of chocolate. Thanks to Tony and Troy as well, for the great conversations over the years, and to Cameron and Nicole, for their friendship throughout graduate school.

Finally, I must also acknowledge the teachers who have made a lasting impact. Mr. Holste, my high school physics teacher, first taught me what it means to be precise as a scientist, and Bob Davis, Matt DeLong, and Ken Kiers will always stand out as models of clarity, patience, and dedication as college professors. I will look to their examples often as I embark on my own academic career. I am also deeply appreciative of the many lunches I have spent with Ron Larson, who has been a wonderful mentor to me throughout my time at Michigan.

TABLE OF CONTENTS

DEDICATION . . . . . **ii**

ACKNOWLEDGEMENTS . . . . . **iii**

LIST OF FIGURES . . . . . **vii**

CHAPTER

I. Introduction 1

1.1 Information processing in the brain 1
1.1.1 The neuron 2
1.1.2 Neuronal circuits 4
1.1.3 Rate coding and population coding 7
1.2 Synchronization in the brain 9
1.2.1 Phase response curves 12
1.2.2 Network connectivity 17
1.3 Synaptic plasticity 19
1.3.1 Long-term potentiation 19
1.3.2 Synaptic plasticity and memory 20
1.3.3 Spike-timing dependent plasticity 23
1.4 Sleep and synaptic renormalization 24
1.4.1 Sleep stages 25
1.4.2 Synaptic renormalization 27
1.5 Outline 29

II. Effects of the frequency dependence of phase response curves on network synchronization 31

2.1 Introduction 31
2.2 Type I and Type II dynamics of Morris-Lecar model neurons 33
2.3 Network Model 35
2.3.1 Network structure 36
2.3.2 Measuring network synchronization 37
2.4 Effects of the PRC Frequency Dependence on Network Synchronization . . . 38
2.5 Discussion and summary 41

III. Cellularly-driven differences in network synchronization propensity are differentially modulated by firing frequency 45

3.1 Introduction 45
3.2 Methods 47
3.2.1 Morris-Lecar neuron model 47

3.2.2 Cortical pyramidal neuron model with simulated acetylcholine modulation . . . 48
3.2.3 PRC Calculation . . . 50
3.2.4 Network simulations . . . 50
3.3 Results . . . 53
3.3.1 Frequency modulation of neuronal phase responses . . . 54
3.3.2 Network correlates of PRC modulation . . . 58
3.4 Discussion and summary . . . 63

IV. Acetylcholine, network dynamics, and synaptic renormalization . . . 77

4.1 Introduction . . . 77
4.2 Materials and Methods . . . 80
4.2.1 Cortical neuron model . . . 80
4.2.2 PRC Calculation . . . 82
4.2.3 Network simulations . . . 83
4.3 Results . . . 86
4.4 Discussion and summary . . . 93

V. Summmary and conclusions . . . 105

BIBLIOGRAPHY . . . **109**

LIST OF FIGURES

Figure

1.1 Illustration of different phases of a neuronal action potential. 3

1.2 Primary anatomical features of a neuron. 4

1.3 Neuronal circuit which generates the knee-jerk reflex. 5

1.4 Firing rates of sensory neurons versus weight applied to frog muscle. 8

1.5 Example of a tuning curve. 9

1.6 Difference between complete synchronization and phase locking 10

1.7 Examples of Type I and Type II PRCs. 14

1.8 Intuition for effects of phase response curve type on neuronal synchronization . . . 15

1.9 Illustration of small-world network connectivity. 18

1.10 Neuronal basis of memory formation in *Aplysia* 21

1.11 Experimental data depicting the effects of spike-timing dependent plasticity 24

1.12 Typical EEG traces of the different stages of sleep. 26

1.13 Overview of the synaptic renormalization hypothesis. 28

2.1 Characteristics of Type I and Type II Morris-Lecar neurons 32

2.2 Frequency-dependent attenuation of PRC amplitude 35

2.3 Effects of frequency modulation on network synchrony 43

2.4 Differential effects of frequency modulation on Type I and Type II network synchrony 44

2.5 Effects of frequency and connectivity density on network synchrony 44

3.1 Neuronal response characteristics of Type I and Type II neurons for Morris-Lecar and cortical pyramidal cell models 67

3.2 Effects of modifying speed of intracellular currents upon depth of PRC delay in Type II neurons 68

3.3 Type II PRC profiles with the same delay depth for different levels of external current. 69

3.4 Differential effects of frequency modulation on Morris-Lecar network synchronization 70

3.5 Differential effects of frequency modulation on network frequency and synchronization of cortical pyramidal cells. 71

3.6 Differential effects of frequency modulation upon phase-zero synchronization in Types I and II cortical pyramidal cell networks. 72

3.7 Time to synchronization for differentially-driven Type II cortical pyramidal cell networks. 73

3.8 Differential effects of frequency modulation upon phase locking in cortical pyramidal neuronal networks. 74

3.9 Average network frequency was directly modulated by noise frequency in stochastic input simulations. 75

3.10 Differential effects of frequency modulation upon synchronization in stochastically-driven cortical pyramidal cell networks. 76

4.1 Effects of acetylcholine on phase response curves, network synchrony, and overall network synaptic potentiation. 97

4.2 Effects of acetylcholine on network potentiation and synchronization for varied network parameters. 98

4.3 Structure of neuronal firing of pre- and post-synaptic cell pairs in cholinergic and non-cholinergic cortical networks. 99

4.4 Effects of noise amplitude on the difference in network potentiation between networks with and without cholinergic modulation. 100

4.5 Effects of connectivity density upon network potentiation. 100

4.6 Effects of the modulation of the STDP window, τ_{stdp}, upon network potentiation. . 101

4.7 Effects of acetylcholine on network potentiation and synchronization for varied network parameters with an asymmetric STDP rule. 102

4.8 Effects of acetylcholine on network potentiation and synchronization for varied network parameters with a multiplicate STDP rule. 103

4.9 Effects of alternately switching between the presence and absence of cholinergic modulation in a cortical network with an embedded cluster. 104

CHAPTER I

Introduction

The human brain is the physical foundation of all sensations, desires, emotions, memories, and thoughts. How this 1.5-kilogram mass of neural tissue supports such complex phenomena has been debated at least since the Greek philosopher Alcmaeon first suggested that the brain is the seat of intelligence. It was barely one hundred years ago, however, that the study of the brain entered the modern scientific era with the pioneering experiments of Santiago Ramón y Cajal. Cajal discovered that the brain is composed of neurons which connect with one another to form circuits which unidirectionally transmit electrochemical signals [1]. This laid the foundation for the modern paradigm of computational neuroscience, which views the brain as a powerful computational organ which produces cognition and motor output by processesing information, much like a computer.

1.1 Information processing in the brain

The analogy between brains and computers should not be pushed too far, however. For one, there are many tasks in which computers far outperform brains (such as performing fast mathematical computations, manipulating images, and searching for words in documents), just as there are many tasks in which brains far outperform computers (such as discovering new mathematical theorems, composing music, and

conducting coherent conversations). The striking disparity in computational ability between brains and computers is at the very least a result of their vastly different construction. Computers and brains differ in their fundamental components, the interactions between those components, and the ways in which those interactions are harnessed to process information.

1.1.1 The neuron

Whereas transistors are the elementary processing units in computers, the brain is fundamentally composed of neurons. The basic physical function of each of the $\sim 10^{11}$ neurons in the brain is the same: to transmit electrochemical signals. To serve as a signaling device, the neuron establishes an electrical potential difference across its cell membrane by tightly regulating the passage of various ions. Specialized transmembrane proteins known as ion pumps actively establish transmembrane concentration gradients of Na^+, K^+, Cl^-, Ca^{2+}, and other ionic species. Crucially, the cell membrane is selectively permeable to just one ionic species, K^+, when resting. This results in K^+ ions passively flowing down their concentration gradient, from inside to outside the cell. This leaves a small excess of negative charge within the cell, which attracts the exited K^+ ions to the external surface of the cell membrane, thereby establishing a transmembrane electrical potential difference.

The resting membrane potential of a neuron typically lies between -60 mV and -80 mV. A neuron's membrane potential will typically fluctuate around this resting membrane potential until the neuron receives input from another neuron. Such input may cause the neuron's membrane potential to increase; if it breaches a certain threshold, voltage-gated ion channels will open and allow Na^+ ions to flow into the cell, thereby causing the membrane potential to rise even more quickly. After a very short time (approximately 1 ms), a different set of voltage-gated ion channels will

open and allow K^+ ions to flow out of the cell, causing the membrane voltage to return to its resting state. This process is illustrated in Fig. 1.1.

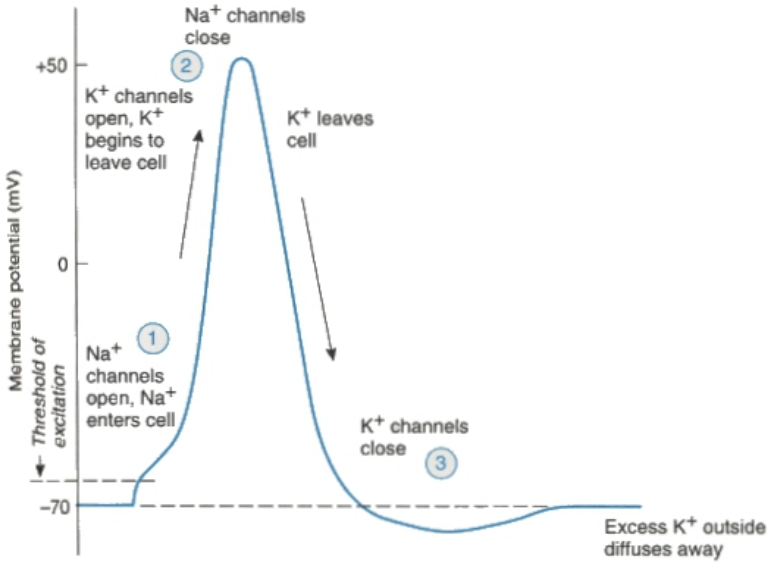

Figure 1.1: Illustration of different phases of a neuronal action potential.

Action potentials constitute the electrical phase of the electrochemical signals that are transmitted from neuron to neuron. Action potentials are initiated in the axon hillock (which connects the cell body and the axon) and propagate down the neuron's axon to various connections that the neuron makes with other neurons, known as synapses (see Fig. 1.2). At these synapses the propagating electrical signal is transduced to a chemical signal as the spike in membrane potential initiates a molecular cascade that results in the release of neurotransmitter molecules from the neuron. These neurotransmitter molecules diffuse across a short space between the pre-synaptic neuron (the neuron that "sends" the neurotransmitter) and the post-synaptic neuron (the neuron that "receives" the neurotransmitter) and induce changes in the membrane potential of the dendrites of the post-synaptic neuron. Dendrites constitute the "input" units of a neuron, and they transmit their altered membrane potentials to the soma, where the incoming signals from various dendrites

are summated. If the membrane potential of the soma increases beyond a certain threshold, an action potential is generated, and the entire process repeats itself.

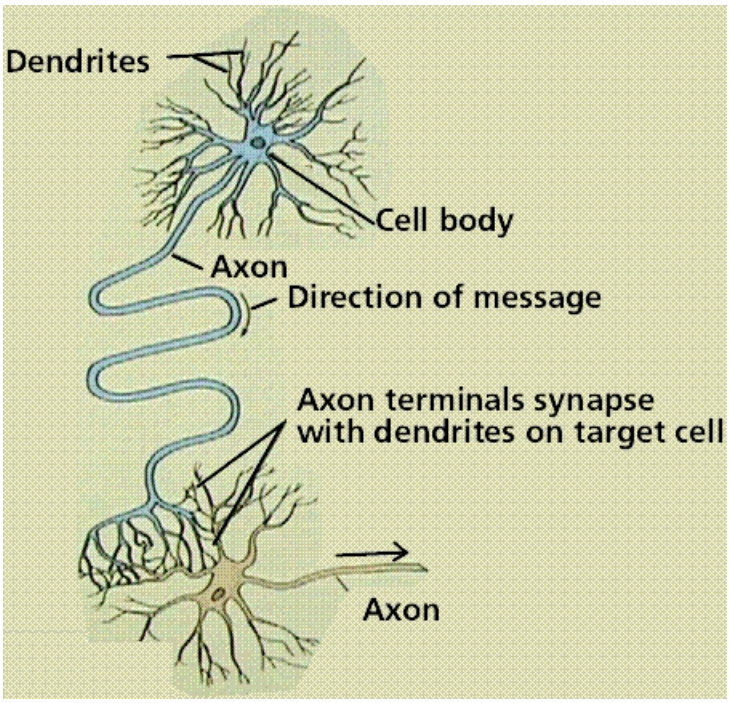

Figure 1.2: Primary anatomical features of a neuron. Neurotransmitter released from pre-syanptic neurons alters the membrane potential of a given neuron's dendrites. These dendritic signals propagate to the neuron's cell body, or soma, where they are summated. If the soma's membrane potential breaches a certain threshold, an action potential is generated and propagates down the neuron's axon. At the end of the axon, this electrical signal induces the release of neurotransmitter, and the entire process is renewed in downstream neurons.

One crucial point is that when a neuron generates an action potential, it will release one of two kinds of neurotransmitter: one kind causes the membrane potential of post-synaptic neurons to *increase*, while the other kind causes the membrane potential of post-synaptic neurons to *decrease*. Neurons which do the former are called *excitatory*, and neurons which do the latter are called *inhibitory*. Both kinds are essential to normal brain function.

1.1.2 Neuronal circuits

In order to process information, neurons in the brain are connected in highly complex but specific patterns which are capable of producing appropriate motor

output in response to varying sensory input. A simple example of input-output neuronal processing is found in the knee-jerk reflex, which serves to stabilize the body when balance is temporarily lost (see Fig. 1.3). When a physician taps below a patient's knee with a reflex hammer, this pulls a tendon, which in turn stretches the patient's quadriceps femoris muscle. This muscle must subsequently contract in order for the familiar reflexive response–the extension of the lower leg–to occur. The neuronal circuit which mediates this response starts with a bundle of *sensory neurons* (so called because they respond to sensory input) which have ion channels that are sensitive to stretching of the quadriceps femoris, thus resulting in these neurons firing a barrage of action potentials in response to the hammer tap.

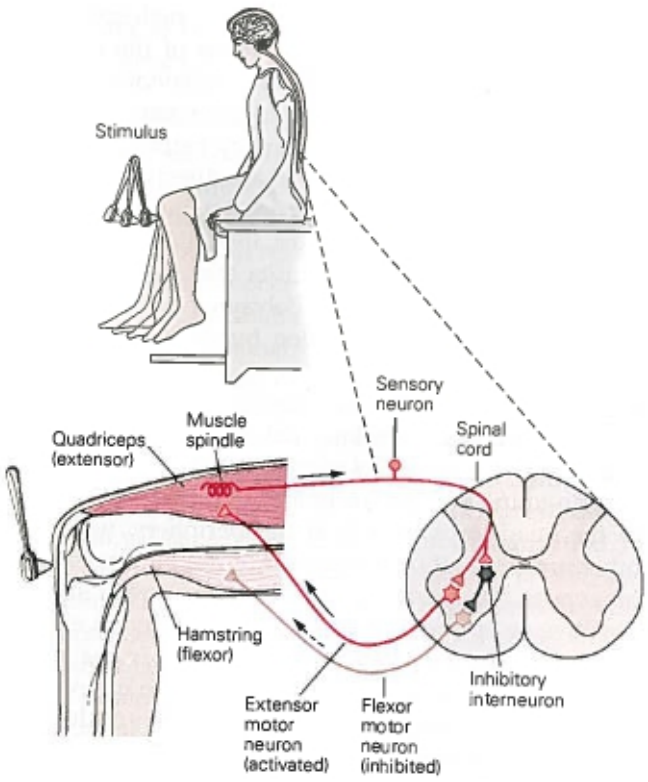

Figure 1.3: Neuronal circuit which generates the knee-jerk reflex. Note the parallel pathways in this circuit. One involves the sensory neurons directly stimulating the motor neurons which cause the quadriceps to contract, while the other involves inhibitory interneurons which prevent the hamstring from contracting. This image taken from [2].

These sensory neurons are very long, projecting from the quadriceps femoris all the way to the spinal cord, where they form connections with *motor neurons*, which in turn project all the way back to the quadriceps. Motor neurons are an important class of neurons which connect directly to muscles and cause muscles to contract by firing action potentials. In the knee-jerk circuit, contraction of the quadriceps is a result of increased activity of motor neurons, which is a result of increased activity of pre-synaptic sensory neurons, which is a result of muscle stretching due to the hammer tap.

This chain of events describes only half the circuit, however, for there is a parallel pathway which ensures that the muscle group antagonistic to the quadriceps, the hamstring, does *not* contract. The sensory neurons originating in the quadriceps accomplish this by forming a second set of connections in the spinal cord with inhibitory neurons. These inhibitory neurons in turn connect to the motor neurons responsible for causing the hamstring to contract. The inhibitory neurons therefore prevent contraction of the hamstring when they fire at a high rate, which they do upon receiving elevated input from the pre-synaptic sensory neurons projecting from the quadriceps. These inhibitory neurons belong to a general class of neurons known as *interneurons*, a broad term which encompasses all neurons that are not sensory or motor neurons. Interneurons are crucial in processing information, as this simple circuit illustrates: without the inhibitory interneurons, there would be no mechanism to prevent simultaneous contraction of both the quadriceps and the hamstring.

The circuit mediating the knee-jerk reflex is extremely simple in comparison to the morass of neural circuitry which comprises the brain. Each neuron in the human cerebral cortex is estimated to receive between 5,000 and 50,000 connections from other neurons [3]. Despite this enormous complexity, all behavior can still be

understood as a product of the three stages described in the knee-jerk circuit: 1) encoding of stimuli by sensory neurons, followed by 2) processing of sensory signals by intermediate neuronal networks, and finishing with 3) behavioral output generated by motor neurons.

It is, of course, an enormous challenge to decipher how the billions of neurons in the brain process incoming sensory signals, and not just because there are so many connections to untangle. The structure of these connections is very complicated, rarely being organized in a strictly feed-forward manner as in the knee-jerk circuit, but instead exhibiting massive feedback from higher processing centers to lower ones (such as from primary visual cortex to the lateral geniculate nucleus). It has been conjectured that the ubiquitous feedback observed in the brain facilitates top-down processing to support anticipatory memory systems, and that this enhanced ability to anticipate future events is the primary distinction between brains and our predominantly feed-forward modern computers [4, 5].

1.1.3 Rate coding and population coding

Neurons represent, or *encode*, sensory information in a variety of ways. One of the simplest was discovered by Edgar Adrian in 1926, when he observed increased firing rates of sensory neurons in a frog's leg muscle as the muscle was stretched [6] (see Fig. 1.4). This is precisely how sensory information is encoded in the first stage of the human knee-jerk reflex: a hammer tap stretches the quadriceps, which results in a transient increase in the firing rates of sensory neurons projecting from the muscle to the spinal cord. The increase in firing rate serves the functional purpose of inducing action potentials in the post-synaptic motor neurons, which results in a jerk of the knee. Rate coding operates in many neuronal systems, such as neurons in the skin that fire more frequently as greater pressure is applied or as temperature increases

[2], as well as motor neurons which induce more forceful muscle contraction by firing at a higher rate.

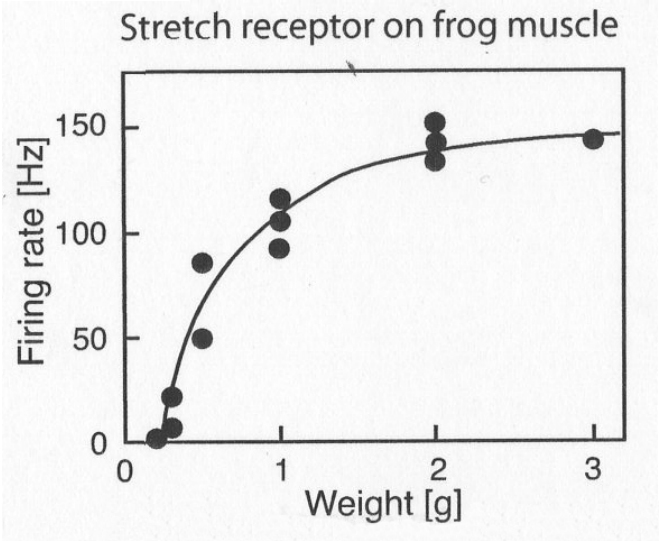

Figure 1.4: Firing rates of sensory neurons versus weight applied to frog muscle. The muscle stretched more as greater weight was applied, which led to increased neuronal firing rates. Image taken from [5].

Closely related to rate coding is *population coding*, in which neuronal firing rates are tuned to one specific value of a stimulus. For example, many neurons in primary visual cortex and the middle temporal area fire at elevated rates only when light bars are swept across their receptive fields at particular orientations. This results in what is known as a tuning curve, in which the functional relationship between firing rate and stimulus orientation is well-approximated by a Gaussian centered upon the "preferred orientation" of a given cell (see Fig. 1.5). This contrasts with the monotonic relationship between firing rate and stimulus intensity observed in rate coding (as in Fig. 1.4).

Population coding is essential to many fundamental functions of the brain. The mental map of a rat's physical environment, for example, depends upon place cells in the hippocampus which are tuned to fire when the rat is located within a circumscribed area [8]. There is strong evidence that the human brain also makes use of

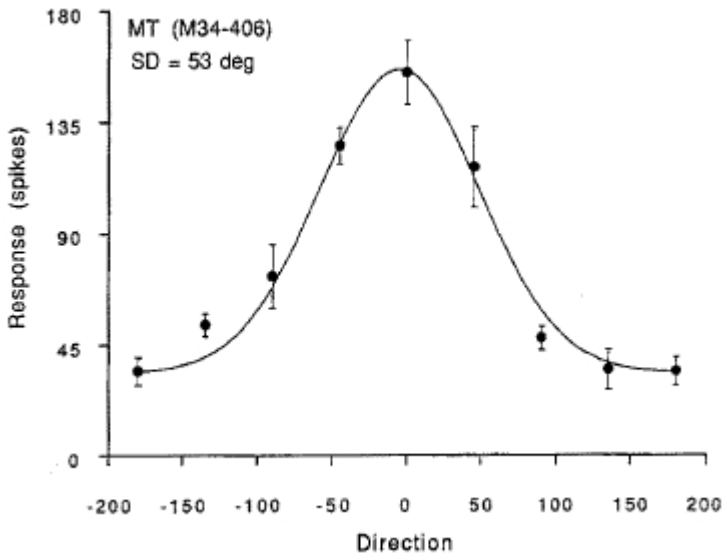

Figure 1.5: Firing rate as a function of stimulus orientation for a specific neuron in the middle temporal area of the macaque brain [7]. Note how maximum firing rate occurs at a preferred value of the stimulus, unlike the monotonic nature of firing rates displayed in Fig. 1.4.

hippocampal place cells [9]. Population coding is also responsible for coordinating movement. Georgopoulos showed that neurons in primary motor cortex of rhesus monkeys are each tuned to specific directions of the monkey's arm movements [10]. This knowledge has enabled the design of algorithms which decode recorded neuronal activity to control prosthetic limbs for monkeys [11] and humans [12]. Population coding is also associated with the cricket's sense of wind direction [13], the macaque monkey's numerosity representation [14], and the direction of saccades in the rhesus monkey's visual system [15].

1.2 Synchronization in the brain

In many cases firing rate is not the only quantity used to process information in the brain. Rate coding is often augmented by *temporal coding* [16], in which relative spike timing conveys information about a stimulus [17]. For example, neurons in the nucleus laminaris of the barn owl encode the azimuthal position of sound sources by

responding to small differences in the arrival time of afferent signals arriving from either ear [18]. In another study, disruption of neuronal synchrony in the insect antennal lobe resulted in diminished ability to discriminate different odors [19, 20].

Temporal precision appears to be important not only for sensory encoding but also in higher-order processing, as neuronal synchrony is associated with many high-level cognitive processes. One study showed a significant link between synchrony and attention by recording from the secondary somatosensory cortex of monkeys that were trained to perform two tasks, one requiring attention to tactile input and the other requiring attention to visual input. The monkeys received both input types simultaneously, and trials which required attention to tactile input resulted in higher pairwise synchrony between cortical neurons compared to trials requiring attention to visual input [21]. The authors showed that a specific kind of synchronization known as *complete synchronization*, in which neurons fire spikes at the same time (see Fig. 1.6), was enhanced.

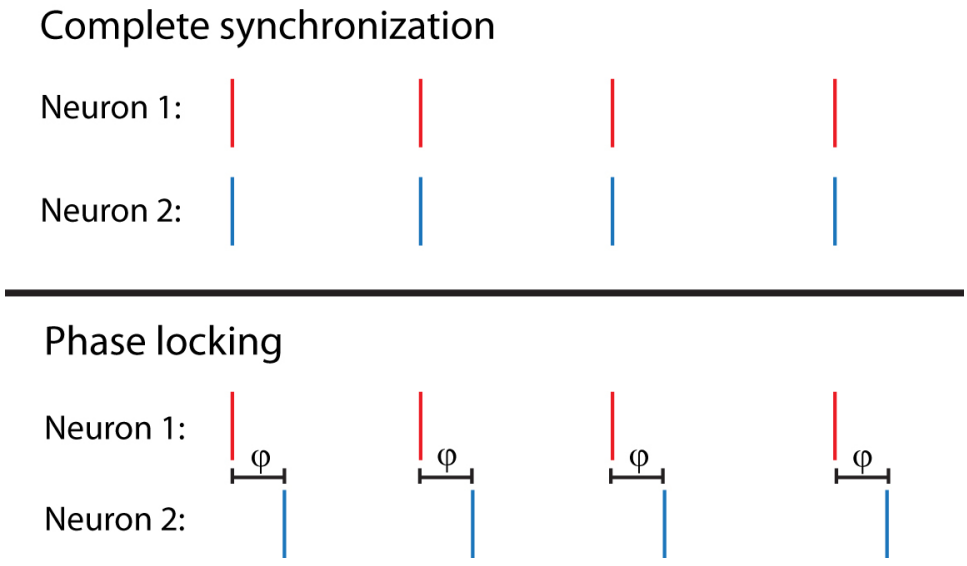

Figure 1.6: Cartoon depiction of the difference between complete synchronization and phase locking. Spikes are represented by vertical lines, and the horizontal axis represents time. Complete synchronization occurs when neurons fire at the same time, whereas phase locking occurs when one neuron leads another by constant phase. Complete synchronization is the special case of phase-zero phase locking.

A more general form of synchronization known as *phase-locking* was found to be predictive of successful memory storage [22]. Rutishauser et. al. conducted an experiment in which subjects were presented 100 novel images for one second each. They were later shown another set of 100 images, 50 of which were taken from the first set, and asked to declare whether or not they had seen each image before. The activities of individual neurons in the medial temporal lobe were recorded in response to the 100 novel images when they were first presented, and the authors then compared the recordings associated with successfully-recalled images to those associated with recall failure. They found that phase-locking synchrony was significantly higher in response to images that were later recalled correctly.

The most debated possible function for neuronal synchronization concerns its relation to the binding problem.This problem addresses how visual features are combined, or *bound*, to form a unified perception, such as how another person's nose, eyes, mouth, chin, etc., are bound into the unitary perception of their face. The "temporal correlation hypothesis" asserts that neuronal assemblies which respond to individual features must synchronize in order for the features to be bound [23]. This idea was proposed independently by Milner [24] and von der Malsburg[25], and it was supported by a 1989 experiment performed by Gray and Singer. They showed that the synchronization of two neurons with adjacent (but non-overlapping) receptive fields was higher when a single, long light bar was swept across the two receptive fields than when two disconnected light bars were simultaneously swept across the same receptive fields [26]. Simple though this observation was, it demonstrated that neuronal synchronization could encode global stimulus properties, and may therefore be essential to visual binding. Whether or not synchronization is actually involved in visual binding has not yet been resolved and remains an issue of contentious debate

[27].

While synchronization has been linked to many higher-order brain processes, it has also been implicated in several pathologies of the brain. The characteristic tremor associated with Parkinson's disease, for example, is associated with highly-synchronized neuronal activity in the subthalamic nucleus [28]. Epileptic seizures have traditionally been thought to result from extensive hypersynchronous neuronal activity [29], though some recent studies have called this into question [30, 31]. There is also evidence that abnormal synchronization is associated with schizophrenia, autism, and Alzheimer's disease [32, 33].

Taken together, the preponderance of the evidence suggests that neuronal synchronization is enormously important to proper brain function, though many details (such as whether synchrony is definitely necessary for binding, how synchrony facilitates memory formation, and what constitues "abnormal" synchrony) are still unknown. Understanding the factors that determine the level of neuronal synchronization is therefore critical both to understanding how the brain operates and to finding treatments for various diseases of the brain.

A wide variety of factors are known to influence synchronization, but they can generally be grouped into one of two categories: cellular properties or network properties. The work presented in this dissertation focuses on a specific measure of cellular properties known as the phase response curve, and also considers the influence of network connectivity upon network synchrony.

1.2.1 Phase response curves

The phase response curve (PRC) is an important tool for understanding the propensity of a group of neurons to synchronize. The PRC characterizes the response of one periodically firing neuron to a brief current pulse (which can be excitatory or

inhibitory), and it is calculated as the normalized time difference between the firing of the neuron when it is perturbed by the external pulse relative to its firing when it is unperturbed:

$$\Delta = \frac{T - T_{pert}(\theta)}{T}, \tag{1.1}$$

where $\theta = t/T$ denotes the normalized phase of the neuron when the external pulse is applied (with $\theta \equiv 0$ at a voltage peak), t is the time of pulse application, T is the firing period of the unperturbed neuron and T_{pert} is the period of a perturbed cycle. Thus, the value of Δ is negative if the perturbed period is longer than the unperturbed one (constituting a phase delay) and, conversely, it is positive if the perturbed period is shorter than the unperturbed one (constituting a phase advance). Neuronal PRCs typically belong to one of two groups. Type I PRCs show phase advances in response to external stimuli for almost all stimulus phases, while Type II PRCs show a region of phase delay for early excitatory stimulus phases and a region of phase advance for late excitatory stimulus phases (see Fig. 1.7).

Properties of PRCs and their implications for neuronal responses have been studied extensively for single neurons as well as for small networks composed of a few cells [35, 36, 37, 38, 39, 40]. Theoretical results have shown that two mutually-coupled excitatory neurons with Type II PRCs tend to completely synchronize more readily than two neurons with Type I PRCs [35, 36]. This may generally be attributed to the absence of a phase delay region in the Type I PRC, which leaves Type I neurons with only one method of adapting to the signal of a coupled neuron. For a heuristic explanation of this phenomenon, see Fig. 1.8. Formally, consider the simplified model of two phase oscillators with identical natural frequencies and which interact via a prescribed PRC [36], so that their dynamics are described by

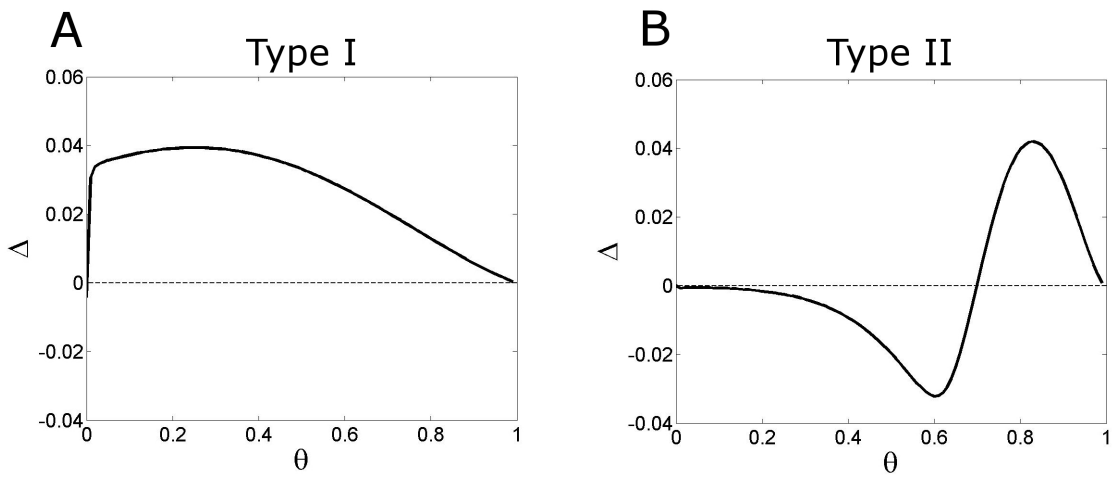

Figure 1.7: Examples of Type I and Type II PRCs. (A) Neurons with Type I PRCs respond to a brief excitatory perturbation by advancing their phase, regardless of when in the oscillatory cycle the perturbation is received. (B) Neurons with Type II PRCs show phase delays when input is received relatively early in the oscillatory cycle, and they switch to phases advances when the input is received late. The PRCs shown here are calculated for the model cortical pyramidal neurons presented in [34].

$$\phi_1' = \omega + PRC(\phi_1 - \phi_2) \tag{1.2}$$

$$\phi_2' = \omega + PRC(\phi_2 - \phi_1). \tag{1.3}$$

Define $\theta = \phi_2 - \phi_1$ and subtract Eq. 1.2 from Eq.1.3 to obtain

$$\theta' = PRC(\theta) - PRC(-\theta) \equiv H(\theta). \tag{1.4}$$

Because the PRC is periodic over 2π, phase-locked solutions exist at $\theta = 0$ and $\theta = \pi$ (since $PRC(\pi) = PRC(-\pi)$). For a solution θ_s to be stable, $H(\theta)$ must have a positive slope,

$$\left.\frac{dH(\theta)}{d\theta}\right|_{\theta=\theta_s} > 0. \tag{1.5}$$

This condition is always met by Type II PRCs at $\theta = 0$, since they by definition have a negative slope at $\phi = 0$, which corresponds to a positive slope of $H(\theta)$ at $\theta = 0$.

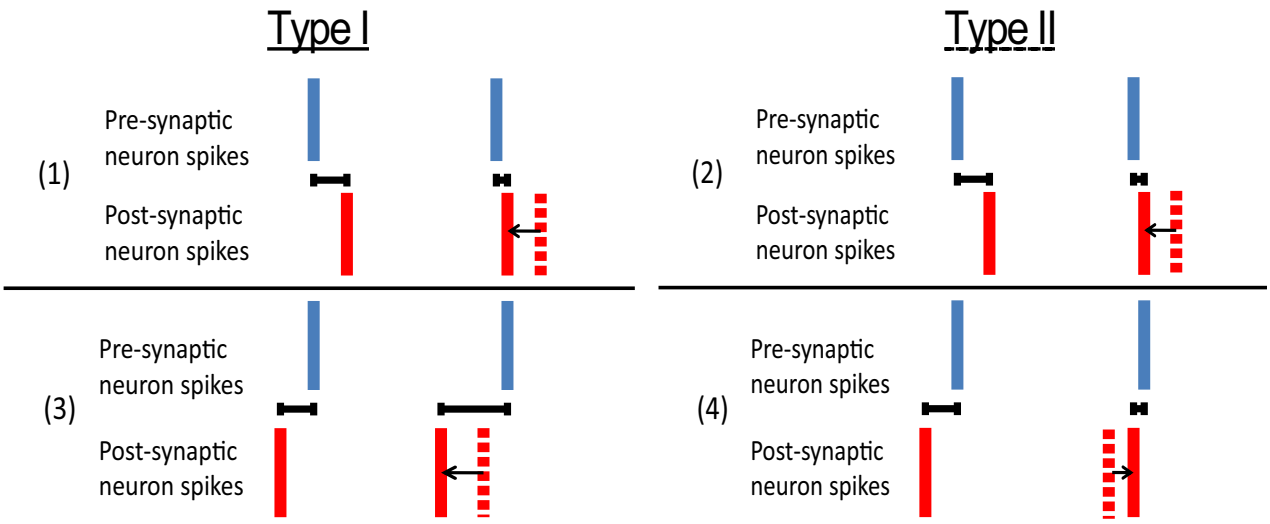

Figure 1.8: Heuristic explanation of why excitatory neurons with Type II PRCs have a greater propensity for synchronization than excitatory neurons with Type I PRCs. Consider two neurons coupled with a unidirectional excitatory synapse and being driven to fire periodically at similar frequencies. For cases (1)-(4), vertical ticks represent spike times of the pre-synaptic (blue) and the post-synaptic (red) neuron during an unperturbed cycle (dashed tick) and a perturbed cycle (solid tick, with black arrows indicating the change in spike time). In cases (1) and (2), the pre-synaptic neuron fires near the end of the post-synaptic neuron's oscillatory cycle, which induces a phase advance in both Type I and Type II neurons. The phase advance results in the post-synaptic spike occurring closer in time to the next pre-synaptic spike, thereby enhancing synchrony. In cases (3) and (4), the pre-synaptic neuron fires near the beginning of the post-synaptic neuron's oscillatory cycle. This induces a phase advance in the Type I post-synaptic neuron but a *phase delay* in the Type II post-synaptic neuron. The phase advance of the Type I neuron increases the separation in time between spikes of the pre- and post-synaptic neurons, resulting in diminished synchrony. In contrast, the phase delay of the Type II neuron decreases the separation in time between spikes of the pre- and post-synaptic neurons, resulting in enhanced synchrony. Thus, input to Type II neurons at both early and late phases promotes synchrony, while input to Type I neurons only promotes synchrony when received at late phases.

Type I PRCs do not have a negative slope at $\phi = 0$ and therefore are not guaranteed to completely synchronize; their peaks may be skewed toward later phases in order for the slope of $H(\theta)$ to be positive at $\theta = 0$. Theoretically, therefore, two-neuron networks coupled with excitation will always completely synchronize if they are both Type II, but if they are Type I they will only completely synchronize if their PRCs take a special form, such as being skewed to the right. Other theoretical work has shown that inhibitory coupling between two Type I neurons strongly favors complete synchrony, opposite the case of excitatory coupling [41, 42].

Experimental exploration of these predictions is made possible by the dynamic clamp technique, which enables the application of computer-controlled synaptic conductance pulses to biological neurons [43, 44]. This allows for the construction of hybrid networks, typically composed of either one biological neuron and one model neuron, or of two biological neurons. Netoff et. al. used dynamic clamp to investigate the synchronization of pairs of entorhinal stellate cells whose PRCs were Type I and shifted to the right when stimulated with excitation [45]. They found that these cells completely synchronized when coupled with excitation, but fired out of phase when coupled with inhibition. The first finding was in line with theoretical predictions, but the second was not. The authors conjectured that synchronization was not achieved under inhibitory coupling because inhibitory effects are more susceptible to noise, suggesting that PRC theory may be more biologically relevant to excitatory than to inhibitory coupling.

One might also question whether PRC theory is biologically relevant for networks of more than two neurons. While experimental investigation is currently infeasible, simulations of large-scale neuronal networks have shown that PRC theory is a good predictor of synchronization in large-scale networks [46], with excitatory Type II networks demonstrating a much greater propensity for synchronization than excitatory Type I excitatory networks. But what else can PRC theory tell us about the synchronization of large-scale networks? Surprisingly little work has been done to answer this question. A theme for the work presented in this thesis is to investigate the robustness of the more detailed predictions made by PRC theory for synchronization in large-scale networks.

1.2.2 Network connectivity

While the PRC may be a powerful tool for understanding and predicting neuronal synchronization, it is far from the only factor to influence network dynamics. Given a set of neurons whose PRC properties are fixed, network activity can still be dramatically altered by changing network connectivity. Simulations of hippocampal networks, for example, show that a phase transition occurs in network synchrony as the average in-degree (number of incoming connections per neuron) increases [47]. And even when the mean in-degree is above the critical threshold required for synchrony, network coherence can still be diminished by increasing in-degree *heterogeneity* [48].

Perhaps one of the most striking features of connectivity structure in the brain is the high proportion of short-range connections (projecting within clusters), complemented by a minority of long-range connections (which project between clusters) [49]. Watts and Strogatz devised a very useful method of modeling such structure [50]. Start with a group of neurons (or "nodes," in the more general terminology of network theory) that are each connected to their r nearest neighbors, forming a lattice-like structure. Then individually consider each connection in the network, and with probability p re-wire it to a new, random target. The Watts-Strogatz method is simple, requiring only three parameters (the number of neurons in the network N, the radius of connectivity r, and the re-wiring probability p), yet it is extremely useful because it interpolates between lattice-like, locally coupled networks and completely random networks (see Fig. 1.9). Between these two extremes lies the so-called "small-world" regime, where network structure is highly clustered (as quantified by a measure called the clustering coefficient), yet the average path length between any two nodes is relatively small. It is within this small-world regime that neuronal networks typically transition from asynchronous to synchronous dynamics,

for the introduction of even a small number of long-range connections can have a very strong synchronizing effect [51].

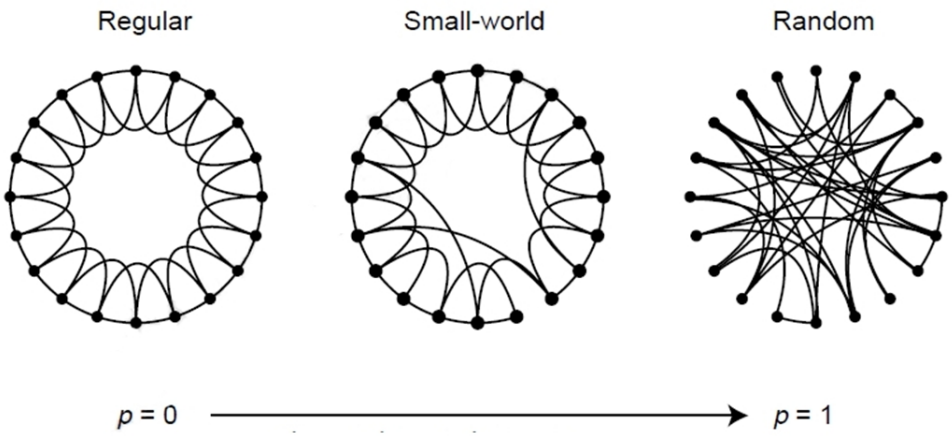

Figure 1.9: Illustration of how the re-wiring probability of the Watts-Strogatz model interpolates between a regular, lattice-like network and a random network. Image taken from [50].

Studies indicate that cortical connectivity structures in many species exhibit "small-world" connectivity, as defined by clustering coefficient and average path length [52]. This has led to widespread use of the Watts-Strogatz method to model connectivity in the brain, which is fine as long as the modeler recognizes that this method certainly does not capture all features of the rich and complex structure of real-world neuronal networks. In the work presented in this dissertation, the Watts-Strogatz method is used as a way to explore a wide range of network structures while scanning just a few parameters. Since we do not know the exact parameter set which best replicates connectivity structure in various areas of the brain, we are interested in results which hold for large regions of parameter space, and are therefore likely to apply to the specific network structures realized in the brain.

1.3 Synaptic plasticity

Part of the difficulty in modeling the brain is that even if its connectivity could be determined down to each and every synapse, such knowledge would almost instantly be obsolete, for the brain constantly reconfigures its connections. The ability to grow, purge, and modify the strength of connections in response to neuronal activity is known as *synaptic plasticity*, and it enables the brain to adapt to ever-changing environments. The concept was famously postulated by Donald Hebb in 1949 when he conjectured that "when an axon of cell A is near enough to excite cell B or repeatedly or persistently takes part in firing it, some growth process or metabolic change takes place in one or both cells such that A's efficiency, as one of the cells firing B, is increased" [53]. Hebb's postulate was dramatically confirmed by Terje Lomo's work investgating the rabbit brain in 1973.

1.3.1 Long-term potentiation

Lomo was interested in how neurons in the dentate gyrus (a region of the hippocampus) would respond to activity from a bundle of fibers known as the perforant path, which is the primary input to the hippocampus. Lomo stimulated the perforant path with a brief electrical pulse, then characterized the response of neurons in the dentate gyrus by recording their excitatory post-synaptic potentials (EPSP's). Lomo next stimulated the perforant pathway with high-frequency (100 Hz) electrical activity, inducing action potentials in the dentate gyrus, then returned to the initial protocol of administering a brief electrical pulse and measuring EPSP's in the dentate gyrus. To his surprise, the EPSP's increased dramatically in both magnitude and slope after the high-frequency stimulation, indicating that the synapses between the perforant pathway and the dentate gyrus had grown much stronger. Crucially,

this increase in synaptic efficacy lasted for at least several hours, and in some cases for days [54].

This phenomenon was christened *long term potentiation* (LTP), and it convincingly demonstrated that correlated activity between pre- and post-synaptic neurons may result in potentiation of their intervening synapses. Subsequent work revealed that post-synaptic NMDA receptors function as molecular "coincidence detectors," since they open to allow calcium influx only when glutamate is released by pre-synaptic neurons *and* the post-synaptic cell is depolarized. The calcium influx induces a complex molecular cascade which ultimately results in AMPA receptors being added to the post-synaptic cell membrane, thereby strengthening the synapse [1, 55].

LTP is not merely an intellectual curiosity, for it has a role to play in a very important cognitive function: memory. Various studies have shown that mice which are genetically modified in ways which disrupt hippocampal LTP suffer severe spatial memory impairment [56, 57]. Why is synaptic plasticity essential to proper memory function? The answer to this question is best understood by considering a simpler system.

1.3.2 Synaptic plasticity and memory

The giant marine snail *Aplysia* is a fairly simple invertebrate organsim that has proven invaluable to investigation of the neuronal correlates of memory formation. The gill is an exposed organ which *Aplysia* uses to breathe, and which it reflexively withdraws for protection when the nearby siphon is lightly touched (see Fig. 1.10(a)). The neurons mediating this behavior are very large and therefore quite accommodating to electrophysiological recording, a fact which Eric Kandel exploited to map their connectivity. Kandel wanted to understand the biological changes which supported two learned behaviors: in habituation, repeated stimulation of the siphon

leads to diminished gill withdrawal, while in sensitization, pairing siphon stimulation with a sharp shock to the tail leads to increased gill withdrawal in response to siphon stimulation alone [1].

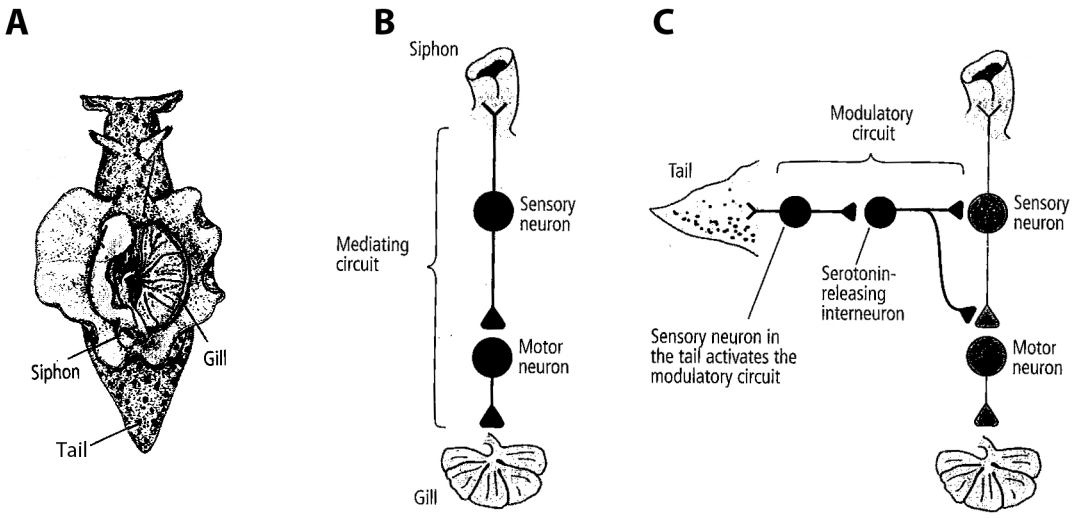

Figure 1.10: Neuronal basis of memory formation in *Aplysia*. (a) The three main structures involved in the behavioral modification protocols induced by Kandel. (b) Neuronal circuit mediating habituation of the gill withdrawal reflex. If the siphon is repeatedly stimulated, the gill will respond less and less due to a weakening of the sensory-motor synapse depicted here. (c) Neuronal circuit mediating sensitization of the gill withdrawal reflex to tail shock. Repeated shocks to the tail result in serotonin being released at the same sensory-motor synapse as in (b), resulting in siphon stimulation eliciting a greater gill withdrawal response. This image was adapted from [1].

Kandel found that both instances of learning result from modification of synaptic strength. Habituation occurs due to weakening of the connections between sensory neurons (which respond to siphon stimulation) and motor neurons (which induce gill withdrawal–see Fig. 1.10(b)). On the molecular level, this weakening results from decreased pre-synaptic release of glutamate. Sensitization depends upon a modulatory circuit which originates in the tail and terminates at the synapses between the siphon sensory neurons and the gill withdrawal-inducing motor neurons (see Fig. 1.10(c)). Repeated shocks to the tail result in serotonin being released at these synapses, which in turn induces a molecular cascade which increases pre-synaptic

glutamate release. This effectively strengthens the sensory-motor synapses so that the gill withdrawal reflex becomes more sensitive to stimulation of the siphon.

These two learned behaviors illustrate how memory formation depends upon synaptic plasticity. It is hypothesized that higher forms of memory, such as semantic and episodic memory, also result from synaptic modification, which carves out neural pathways to ensure that specific assemblies of neurons activate in response to appropriate stimuli [58]. The location of these assemblies in the brain remained a mystery for much of the twentieth century, until the enlightening but unfortunate case of Henry Molaison emerged. Henry battled intractable epilepsy after suffering a bike accident as a child, and in a desperate move to cure him doctors removed his entire hippocampus in 1953, when he was twenty-seven years old [59]. The procedure succeeded in controlling his epilepsy, but it had a dramatic and unforeseen side effect: Henry was unable to form new declarative memories. His knowledge of facts and episodes before the surgery remained intact, but he was largely unable to acquire any declarative memories after the operation (though he could form new procedural memories).

The case of Henry Molaison convincingly demonstrated that the hippocampus is essential to the formation of new memories. At the same time, it showed that the hippocampus does not store memories in their final, long-term state, since Henry's pre-1953 memories were unaffected by the operation. The prevailing modern theory suggests that the hippocampus serves as a temporary repository for new memories, which are then transferred to the cortex during sleep [60, 61]. This view is supported by studies showing that spike sequences observed in awake organisms during tasks that require memory formation (such as maze navigation by a rat) are replayed in both the hippocampus [62] and various regions of the cortex [63] during sleep.

Furthermore, suppression of replay events has been shown to impair memory consolidation [64, 65]. Other studies have shown that the hippocampus and cortex replay the same events simultaneously [66, 67], indicating that they engage in a dialogue that is essential to memory consolidation. It is unknown exactly how this dialogue transfers memory traces from the hippocampus to the cortex, but it is assumed that plasticity mechanisms enable the replay of spike sequences to facilitate information transfer through the modification of cortical connections.

1.3.3 Spike-timing dependent plasticity

There exist many forms of activity-dependent synaptic plasticity, but one that has generated significant interest in the last decade is known as spike-timing dependent plasticity (STDP). While most other forms of plasticity depend upon simple increased activity of pre- and post-synaptic neurons, STDP depends upon the fine temporal structure of neuronal spiking. This phenomenon was demonstrated convincingly by Bi and Poo, who persistently paired pre- and post-synaptic spiking of cultured hippocampal neurons while enforcing strict timing differences between spikes [68]. They found that synapses almost exclusively increased in strength when pre-synaptic spiking preceded post-synaptic spiking, while they predominantly decreased in strength when spike ordering was reversed (see Fig. 1.11).

This experimental data is often mathematically modeled as two decaying exponential curves which give the change in synaptic weight as a function of the difference in pre-post spike timing. This model is then used in network simulations to govern the activity-dependent evolution of synaptic strength. STDP models have been used to provide a possible explanation for the development of ocular dominance columns [69], as well as to suggest that neuronal networks may perform a crude form of principal component analysis [70, 71]. Chapter IV of this dissertation describes work

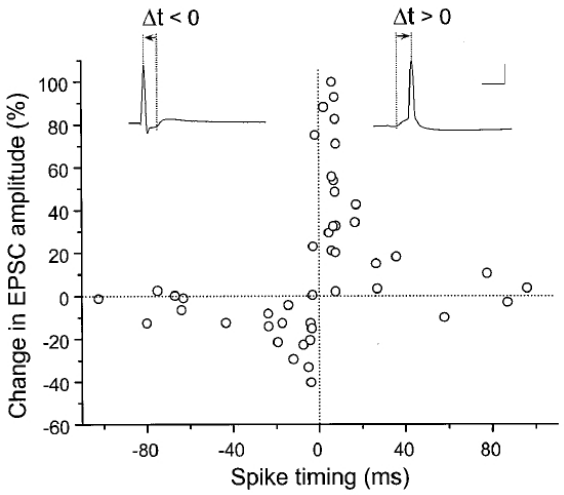

Figure 1.11: Experimental data from cultured hippocampal neurons shows that synaptic strength increases or decreases depending upon whether pre-synaptic spiking precedes or succeeds post-synaptic spiking. Note how the degree of strengthening or weakening depends upon the timing difference between the spikes (positive time differences imply that post-synaptic spikes followed pre-synaptic spikes). This plot is taken from [68].

in which networks with plastic synapses obeying an STDP model were simulated to explore the effects of a ubiquitous, yet poorly understood, animal behavior: sleep.

1.4 Sleep and synaptic renormalization

Sleep is one of the fundamental mysteries facing contemporary neuroscience. Virtually every known species of animal requires sleep, yet we still do not know *why*. The essential need for sleep was demonstrated in a series of experiments by Allan Rechtschaffen, who showed that totally depriving rats of sleep resulted in their death within two to three weeks [72]. Disappointingly, however, no "unambiguous cause of death" could be identified [73]. Various theories for the purpose of sleep have been proposed, including wound healing [74], strengthening of the immune system [75], and memory consolidation [76], and while some of these theories enjoy extensive experimental support, none explain why sleep deprivation should lead to death in such a short time.

1.4.1 Sleep stages

In the early twentieth century, most scientists assumed that sleep results from decreased neuronal activity–that the brain essentially "shuts down" every night due to fatigue [2]. This simple view of sleep was dramatically overturned in the 1930's when Alfred Loomis applied nascent EEG technology to record the brain activity of sleeping subjects. Loomis discovered that the sleeping brain is not quiet, but in fact pulses with a vast repertoire of exotic waveforms [77]. Loomis classified these waveforms into five distinct sleep stages, a concept which remains foundational to the modern study of sleep [78].

We currently understand sleep to consist of two distinct phases: rapid eye movement (REM) and non-rapid eye movement (NREM) sleep. REM sleep is characterized by loss of both muscle tone and body temperature regulation [79], and it is also referred to as paradoxical sleep because its EEG recordings resemble those observed during wakefulness. The eponymous eye movements observed during REM sleep are associated with cholinergically-modulated bursts of neuronal activity in the pons, lateral geniculate nucleus, and occipital cortex known as PGO spikes [80]. Most memorable dreams are thought to occur during REM sleep [81], and EEG recordings typically show low-voltage patterns with mixed frequency content.

In NREM sleep, both muscle tone and regulation of body temperature remain intact, and unlike REM sleep, NREM sleep is further divided into three stages (the old Rechtschaffen and Kales classification system featured four stages, but the more recent American Association of Sleep Medicine system condenses the number to three [78]). Stage N1 features EEG activity similar to that observed during REM sleep, but Stage N1 is not associated with rapid eye movement and serves primarily as a brief transition between wakefulness and Stage N2 (see Fig. 1.12). Stage N2 consti-

tutes a deeper state of sleep, and its EEG is marked by K-complexes (large, biphasic waveforms that are thought to suppress external stimuli from reaching conscious awareness [82]) and sleep spindles. Sleep spindles last ~ 1 s, feature 10-16 Hz oscillations, and are associated with both procedural and episodic memory consolidation [83].

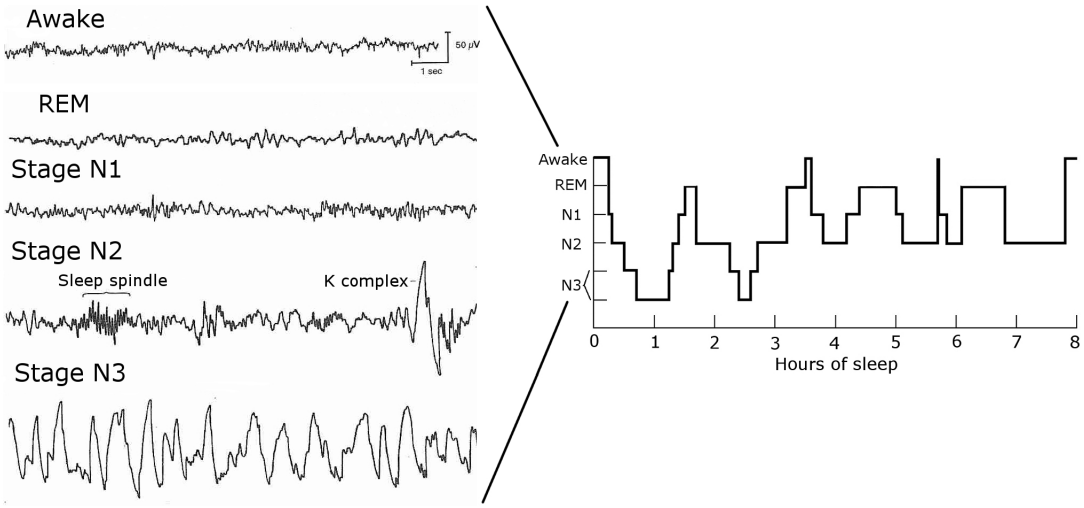

Figure 1.12: Typical EEG traces of the different stages of sleep. On the right is a typical *hypnogram*, which plots the stage of sleep over time. Note how slow wave sleep (Stage N3) progressively decreases in duration throughout the night, while REM sleep increases in duration.

N3 is the deepest stage of sleep and is easily identified by its high-amplitude, low-frequency EEG, for which reason it is also called *slow wave sleep*. Slow waves are produced by the alternating bursting and quiescence of thalamocortical neurons, a pattern which in turn results from their interaction with cells in the reticular nucleus. Thalamocortical neurons have specialized membrane channels that admit calcium only when they are hyperpolarized, so that inhibitory input from the reticular nucleus primes thalamocortical neurons to fire bursts of action potentials. During slow wave sleep the cells of the reticular nucleus fire rhythmically (due to calcium channels similar to those found in thalamocortical cells), and this rhythmic firing induces rhythmic thalamocortical activity, which generates the rhythmic post-synaptic

potentials in cortical dendrites that are recorded as slow waves [2].

Interestingly, slow wave activity is associated with memory consolidation. In one study, for example, participants whose slow wave activity was suppressed during sleep using acoustic stimulation showed decreased improvement in a texture discrimination task relative to the control group [84]. In another study, participants whose slow wave activity was boosted using transcranial stimulation showed increased improvement in a paired-associate learning task compared to the control group [85]. Experiments indicate that slow wave activity and sleep spindles in the neocortex gate high-frequency ripples in the hippocampus, which strongly suggests that memory traces stored in the hippocampus are transferred to the neocortex during slow wave sleep [86, 87]. This theory is made even more compelling by the fact that in rats, spike sequences observed during preceding maze navigation are often replayed within hippocampal ripples during slow wave sleep [88].

1.4.2 Synaptic renormalization

The evidence clearly supports an essential role for slow wave sleep in memory consolidation, but that may not even be its most important function. Giulio Tononi theorizes that slow wave activity is also the primary force which maintains synaptic homeostasis within the brain [89]. This is enormously important because stronger synapses consume more energy and physical space, two precious resources which the brain holds in short supply. Tononi's synaptic renormalization hypothesis posits that synaptic strength is globally upscaled during wakefulness, and that slow wave activity during sleep serves to globally downscale, or "renormalize," connection strength (see Fig. 1.13). This process is thought to simultaneously facilitate memory consolidation by enhancing the relative strength of synapses which comprise memory traces [90].

Evidence in favor of the synaptic renormalization hypothesis continues to mount.

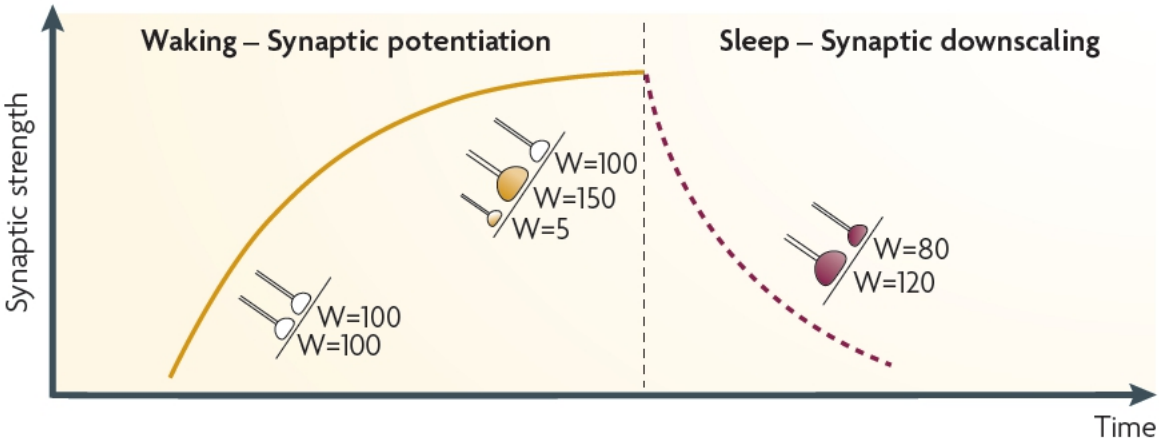

Figure 1.13: Overview of the synaptic renormalization hypothesis. During waking, synapses experience an overall increase in strength, while during sleep they are downscaled. Note that the two synapses in this cartoon start with the same strength, but end with one being relatively stronger, perhaps because it was integrated into a memory trace. This plot is taken from [76].

Electrophysiological studies show that evoked LFP/EEG responses increase in slope during wakefulness and decrease following sleep in rats [91] and humans [92], exactly as the theory predicts. At the level of individual cortical neurons, it has been shown that firing rates increase with wakefulness and decrease following sleep, and that the magnitude of the decrease in firing rate correlates with the intensity of slow wave activity [93]. Furthermore, slow wave activity increases locally during sleep in brain regions known to have experienced significant potentiation during waking, providing compelling support for the idea that slow wave activity has a homeostatic effect [94].

While the synaptic renormalization hypothesis enjoys fairly strong empirical support for its basic premises, it suffers from the fact that it provides no specific biophysical mechanism for either wake-dependent synaptic upscaling or sleep-dependent downscaling [76]. Tononi and others have suggested that differences in the cortical neuromodulatory milieu may favor potentiation during wakefulness and depression during sleep [95], but exactly how the various neuromodulators induce these effects is unclear. Chapter IV of this dissertation describes work done in collaboration

with Victoria Booth, Geoffrey Murphy, and Michal Zochowski which investigates the effects of one particular neuromodulator–acetylcholine–on overall network potentiation. We show that cholinergic modulation provides a possible biophysical explanation for synaptic renormalization.

1.5 Outline

This explanation for synaptic renormalization employs phase response curves, which motivate work throughout this thesis and which we argue are useful for understanding large-scale network dynamics. Chapter II demonstrates their utility by presenting an investigation of how the variation of PRCs with firing frequency affects the synchronization of large-scale neuronal networks. Using the Morris-Lecar neuronal model, we first show that the phase-delay region of Type II PRCs diminishes as frequency increases. We then demonstrate that this leads to decreased synchronization with increased frequency in networks composed of Type II neurons, and we compare these results to those obtained for Type I neurons.

Chapter III continues this line of inquiry using a more realistic neuron model. This model was developed to simulate experimental results which showed that cholinergic modulation switches cortical pyrmidal neurons' PRCs from Type II to Type I [34, 96]. We show that this model also results in significant frequency-dependent attenuation of the phase-delay region of Type II PRCs, and we explain how this effect depends upon the relative speeds of an adaptation-inducing potassium current and a fast-acting sodium current. We also show that in this model, as in the Morris-Lecar model, increased frequency leads to diminished synchronization of networks composed of Type II neurons.

Finally, the work presented in Chapter IV uses the cortical pyramidal model

introduced in Chapter III to investigate how network potentiation is affected by acetylcholine, which is present in cortex during waking but virtually absent during slow wave sleep. We show that the presence/absence of acetylcholine induces low/high network synchronization due to neurons exhibiting Type I/Type II PRCs. This in turn leads to high/low overall network potentiation as a result of STDP, thus indicating that acetcylcholine may be a key to understanding synaptic renormalization, and providing another example in which PRC theory correctly predicts the synchronization properties of large-scale networks.

CHAPTER II

Effects of the frequency dependence of phase response curves on network synchronization

2.1 Introduction

It is well known that individual neurons respond differently to external stimulation. Different response properties are primarily due to different excitation properties of the neuronal membrane, but differences in the anatomical structure of the neurites can also contribute [97]. Two basic measures characterizing general response properties of individual neurons are the frequency-current (f-I) curve and the phase response curve (PRC). The f-I curve measures neuronal firing frequency in response to continuous stimulation by external current. Typically, neurons can be divided into two groups based on their f-I curves, Type I and Type II (see Fig. 2.1(a)). The frequency of Type I neurons is strongly modulated by the magnitude of the external current and can take on very low values at firing threshold. The frequency of Type II neurons is much less responsive to changes in the current magnitude. These neurons start firing at threshold with a critical frequency and as current amplitude increases, firing frequency does not change as significantly.

As mentioned in Section 1.2.1, the PRC is a measure used to describe the response of an individual neuron to perturbations to its oscillation. PRCs are very useful for understanding how well several individual neurons will synchronize when coupled

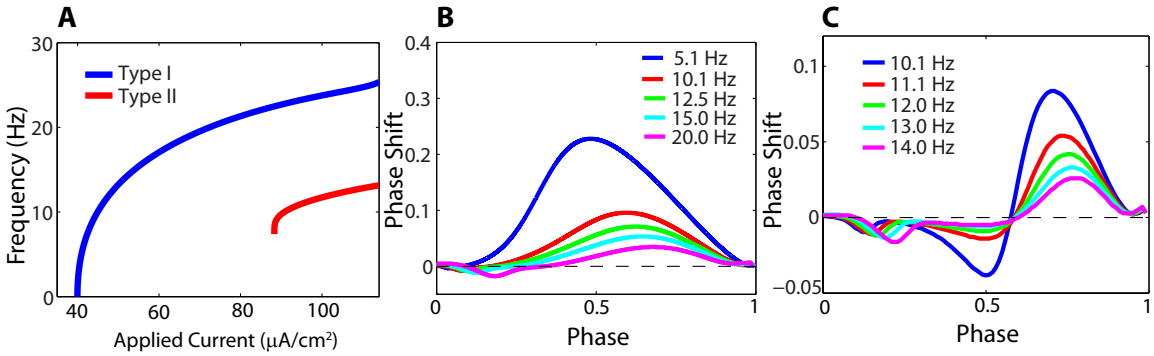

Figure 2.1: (a) Frequency-current (f-I) curves for Type I and Type II Morris-Lecar neurons. The firing frequency of the Type I neuron goes to zero at firing threshold, while the Type II neuron exhibits a threshold frequency of about 8 Hz. (b) PRCs for various firing frequencies of the Type I Morris-Lecar neuron. PRCs were calculated using 0.5 msec excitatory current pulses of amplitude 200 μA/cm^2. (c) PRCs for various firing frequencies of the Type II Morris-Lecar neuron. PRCs were calculated using 0.5 msec excitatory current pulses of amplitude 200 μA/cm^2.

with excitation. Like f-I curves, neuronal PRCs are generally grouped into two categories, and, conveniently, neurons with Type I f-I curves typically have Type I PRCs and neurons with Type II f-I curves typically have Type II PRCs [36].

In this chapter, we first investigate links between these two measures, then investigate their influence on network spatio-temporal activity patterns. Specifically, we measure changes in the PRC as a function of firing frequency of the neuron. We find that while the PRC of a given neuron depends on a number of factors, including the amplitude of the stimulating pulse and the firing frequency of the neuron at which the PRC is measured, for neurons with Type I PRCs these factors mainly influence the amplitude of the induced phase shifts but do not qualitatively change the profile of the PRC. However, for neurons with Type II PRCs, the amplitude of the phase delays evoked at early phases can decrease significantly as the intrinsic firing frequency increases, leading to a more Type I-like response. Thus, by modulating firing frequency, we can continuously monitor the transition from Type II to Type I-like PRCs and observe the effect of this transition upon spatio-temporal patterning in a large network. Specifically, we consider the propensity for synchronization as a

function of network firing frequency in large-scale excitatory networks composed of either Type I or Type II Morris-Lecar model neurons. The work presented in this chapter was published as the textbook chapter "Effects of the frequency dependence of phase response curves on network synchronization" in *Phase Response Curves in Neuroscience*. The work was performed in collaboration with Victoria Booth and Michal Zochowski [98].

2.2 Type I and Type II dynamics of Morris-Lecar model neurons

In our model networks, individual neurons are modeled by the Morris-Lecar equations [99],

$$
\begin{aligned}
(2.1)\quad C\frac{dV}{dt} &= -\overline{g}_{Ca} m_\infty(V)(V - V_{Ca}) - \overline{g}_K w(V - V_K) - \overline{g}_L(V - V_L) + I_{\text{app}} \\
(2.2)\quad \frac{dw}{dt} &= \phi \frac{w_\infty(V) - w}{\tau_w(V)} \\
(2.3)\ m_\infty(V) &= \frac{1}{2}\left[1 + \tanh\left(\frac{\mathrm{V} - \overline{\mathrm{V}}_1}{\overline{\mathrm{V}}_2}\right)\right] \\
(2.4)\ w_\infty(V) &= \frac{1}{2}\left[1 + \tanh\left(\frac{\mathrm{V} - \overline{\mathrm{V}}_3}{\overline{\mathrm{V}}_4}\right)\right] \\
(2.5)\quad \tau_w(V) &= \frac{1}{\cosh\left(\frac{\mathrm{V} - \overline{\mathrm{V}}_3}{2\overline{\mathrm{V}}_4}\right)},
\end{aligned}
$$

where V represents membrane voltage (in mV) and time is measured in msec. Action potentials are generated by an inward Ca^{2+}-mediated current and an outward K^+-mediated current whose dynamics are governed by the gating variable w. The functions $m_\infty(V)$ and $w_\infty(V)$ are the steady state activation functions of the Ca^{2+} and K^+ currents, and $\tau_w(V)$ is the time constant governing dynamics of the gating variable w. The term I_{app} represents an externally applied stimulus to the neuron.

Following [100], we use the parameters listed in Table 2.1 to simulate Type I and Type II Morris-Lecar model neurons. Fig. 2.1(a) depicts the f-I curves of both

Parameter	Type I	Type II
C	20 μF/cm^2	20 μF/cm^2
g_{Ca}	4.0 mS/cm^2	4.4 mS/cm^2
g_K	8.0 mS/cm^2	8.0 mS/cm^2
g_L	2.0 mS/cm^2	2.0 mS/cm^2
V_{Ca}	120.0 mV	120.0 mV
V_K	-84.0 mV	-84.0 mV
V_L	-60.0 mV	-60.0 mV
$\overline{V}_1$	-1.2 mV	-1.2 mV
$\overline{V}_2$	18.0 mV	18.0 mV
$\overline{V}_3$	12.0 mV	2.0 mV
$\overline{V}_4$	17.4 mV	30.0 mV
ϕ	1/15	0.04
I_{app}	35.0 μA/cm^2	80.0 μA/cm^2

Table 2.1: Parameters for the Morris-Lecar Type I and Type II model neurons used in our simulations, taken from [100].

neuron types. Note that the frequency of the Type I neuron is capable of assuming arbitrarily low values at firing threshold, while the Type II neuron exhibits a critical frequency at threshold of about 8 Hz.

Figs. 2.1(b,c) depict the PRCs of Type I and Type II Morris-Lecar neurons in response to excitatory stimulation. Note that at low frequency, both types exhibit a phase delay when a current pulse is applied at values of θ slightly greater than 0. This is due to the fact that $\theta = 0$ is defined to occur at maximum membrane voltage, so that the voltage naturally decreases at the beginning of the cycle, when the neuron is repolarizing after an action potential. The excitatory applied current pulse therefore opposes this process and delays the natural oscillatory behavior. In the Type I neuron, this initial phase delay gives way to phase advance for stimulation at later phases in the firing cycle. The Type II neuron exhibits qualitatively different behavior. The initial phase delay region is followed by a further delay region, forming a second, larger "trough" before finally giving way to a phase advance region at late phases of stimulation.

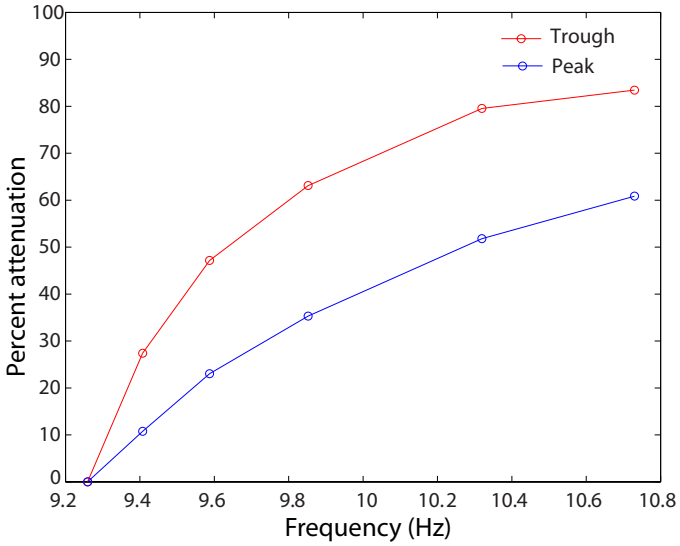

Figure 2.2: Attenuation of both the peak and trough of the Type II PRC as a function of frequency, relative to the amplitudes of the peak and trough when the neuron is firing at approximately 9.3 Hz. PRCs were computed using 0.5 msec current pulses of amplitude 40 μA/cm^2.

In the Morris-Lecar model, PRC properties are strongly affected not only by the properties of membrane excitability but also by the induced firing frequency of the unperturbed neuron. Figs. 2.1(b,c) depict changes in the phase shifts for both types of neurons as the firing frequency of the neuron is increased by increasing the external current I_{app}. In both cases, there is an overall attenuation of the PRC as frequency increases. Additionally, the Type II PRC exhibits an extreme attenuation of the phase delay region relative to the phase advance region with increased frequency, rendering the neuron more Type I-like. This phenomenon is quantified in Fig. 2.2.

2.3 Network Model

To better understand the effects on network dynamics of frequency-dependent changes in the characteristics of the PRC, we simulated large-scale excitatory networks consisting of either Type I or Type II Morris-Lecar neurons for different average network firing frequencies. We varied synaptic weight and network connectivity and then quantified synchronization of the network spatio-temporal activity patterns.

2.3.1 Network structure

In our networks of Morris-Lecar neurons, individual neurons are in an excitable state (I_{app} levels are set below firing threshold) and underlying network activity is driven by random, excitatory noise to each neuron. Thus, we modify equation (3.1) for the membrane voltage of the ith neuron V_i as follows:

(2.6)
$$C\frac{dV_i}{dt} = -\overline{g}_{Ca}m_\infty(V_i)(V_i - V_{Ca}) - \overline{g}_K w_i(V_i - V_K) - \overline{g}_L(V_i - V_L) + I_{\text{app}} + \sum_{j\in\Gamma_i} I_{ij}^{\text{syn}} + I_i^{\text{noise}}.$$

Here we have added two terms, one for the synaptic current exchanged between neurons, $\sum_{j\in\Gamma_i} I_{ij}^{\text{syn}}$, and another for random, excitatory inputs used to modulate average network firing frequency, I_i^{noise}. The synaptic current flowing from neuron j to i is defined to be non-zero if neuron j is directionally coupled to neuron i (i.e., $j \in \Gamma_i$) and the voltage of neuron j is greater than 0 mV. The magnitude of the synaptic current is given by

(2.7)
$$I_{ij}^{\text{syn}} = s\max(0, \mathrm{V}_j).$$

The synaptic weight s is the same for all synapses, and its specific value is one of the parameters varied from simulation to simulation.

The term I^{noise} is used to control the average firing frequency of the network. Each neuron randomly receives square current pulses of amplitude 300 μA/cm^2 and duration 0.5 msec at a specified frequency. The noise frequency determines the average firing frequency of the network. Additionally, Type I and Type II neurons are both given sub-threshold baseline currents, with $I_{\text{app}} = 35\,\mu$A/cm^2 for Type I and $I_{\text{app}} = 80\,\mu$A/cm^2 for Type II, to compensate for their differences in threshold

current.

The neurons are connected in a one-dimensional network with periodic boundary conditions. The connectivity pattern is constructed using the Watts-Strogatz architecture for Small World Networks [50] . A radius of connectivity r is specified, and each neuron is directionally coupled to its $2r$ nearest neighbors. Then, every connection in the network is rewired with probability p to another neuron chosen at random. In this way, $p = 0$ results in a locally-connected network and $p = 1$ in a randomly connected network. The radius of connectivity r therefore determines the density of connections in the network, while the re-wiring probability p determines the network connectivity structure. r is set to 5 for all simulations except those used to generate Fig. 2.5. All simulated networks have 250 neurons.

2.3.2 Measuring network synchronization

We monitor phase-synchronization of firing in the network using the mean phase coherence, σ [101]. The mean phase coherence between a pair of neurons, $\sigma_{1,2}$, is defined by:

$$\sigma_{1,2} = \left| \frac{1}{N} \sum_{k=1}^{N} e^{i\phi_k} \right| \tag{2.8}$$

$$\phi_k = 2\pi \left(\frac{t_{2,k} - t_{1,k}}{t_{1,k+1} - t_{1,k}} \right), \tag{2.9}$$

where $t_{2,k}$ is the time of the k^{th} spike of neuron 2, $t_{1,k}$ is the time of the spike of neuron 1 that is largest while being less than $t_{2,k}$, $t_{1,k+1}$ is the time of the spike of neuron 1 that is smallest while being greater than or equal to $t_{2,k}$, N is the number of spikes of neuron 2, and $e^{i\phi_k} = \cos(\phi_\mathrm{k}) + i\sin(\phi_\mathrm{k})$. The mean phase coherence of the entire network, σ, is calculated by averaging $\sigma_{i,j}$ over all pairs of neurons, excluding $\imath = \jmath$.

2.4 Effects of the PRC Frequency Dependence on Network Synchronization

We investigated the changes in network mean phase coherence as a function of network structure for different values of average frequency of network activity. Figs. 2.3(a-c) summarize the dual effects of synaptic coupling and architecture on synchronization of Type I networks. For low coupling strengths s (vertical axis), the networks essentially fail to synchronize regardless of the value of the rewiring probability p (horizontal axis), indicated by the low values of mean phase coherence. Above $s \approx 0.3$ mS/cm^2, however, the networks synchronize for network architectures with a large fraction of random connectivity. Fig. 2.3(c) shows that the differences in mean phase coherence between networks driven at high frequencies and low frequencies, $\sigma_{\text{high}} - \sigma_{\text{low}}$, are positive, revealing that Type I networks synchronize better at higher frequency. This is hardly a surprising result, because higher network frequency implies more exchange of synaptic current, which leads to greater effective coupling among neurons. For $s \gtrsim 0.45$mS/cm^2, the differences in mean phase coherence, $\sigma_{\text{high}} - \sigma_{\text{low}}$, return to approximately 0, since σ saturates for both the high- and low-frequency networks at such high coupling.

Type II networks, on the other hand, exhibit quite different behavior. Results depicted in Figs. 2.3(d-f) demonstrate that appreciable network synchronization occurs at coupling strengths of $s \approx 0.2$mS/cm^2 and greater. At the same time, the differences in mean phase coherence between networks driven at high frequency and at low frequency, $\sigma_{\text{high}} - \sigma_{\text{low}}$, remain negative, implying that Type II networks synchronize better at *lower frequency* (see Fig. 2.3(f), and note the difference in scale from Fig. 2.3(c)). These results differ from those obtained for Type I networks, in which synchrony increases with increasing mean network firing frequency. This

contrast in synchronization behavior is even more clearly illustrated in Fig. 2.4, where the differences in mean phase coherence between high- and low-frequency networks are plotted as a function of synaptic weight for a number of different pairings of noise frequency. In all cases, the difference in synchronization between high- and low-frequency Type I networks starts at essentially zero, steeply rises to a large peak as synaptic weight increases, then returns to zero as both networks saturate. The presence of this pronounced region of positively-valued $\sigma_{\text{high}} - \sigma_{\text{low}}$ for all frequency pairings demonstrates the tendency of Type I networks to synchronize better at higher frequency. Type II networks, on the other hand, exhibit large regions of negative $\sigma_{\text{high}} - \sigma_{\text{low}}$ for all frequency pairings, indicating that Type II networks tend to synchronize better at lower frequency. Interestingly, Figs. 2.4(c,d) show a small region where $\sigma_{\text{high}} - \sigma_{\text{low}}$ is significantly positive for Type II networks. This feature is lacking in Figs. 2.4(a,b). These contrasting results may be a result of the competing influences of effective coupling and PRC phase delay. As frequency increases, more current is exchanged between neurons, leading to higher effective coupling and increased synchronization. At the same time, increasing frequency also leads to a diminishing phase delay region in the neuronal PRCs, which depresses synchronization. The interplay between these two influences is nontrivial, and we see that in Figs. 2.4(a,b) the depressive pressure of the neuronal PRC dominates for virtually all values of s, while in Figs. 2.4(c,d) the positive pressure of effective coupling dominates for small synaptic weight values, before giving way to the effects of the neuronal PRC at greater values of s.

We obtain similar results when considering cross sections of the color plots from Figs. 2.3(a-f). In Figs. 2.3(g,h) the synaptic coupling is fixed and the mean phase coherence is plotted as a function of re-wiring probability p for four different noise fre-

quencies. The strength of synaptic coupling was chosen to lie in a transitional region, where Type I network synchrony takes on an intermediate value ($s = 0.36$ mS/cm^2). In both Type I and Type II networks, mean phase coherence increases with increasing re-wiring probability, but increasing frequency affects the two types of networks in different ways. In the Type I network (Fig. 2.3(g)), higher frequency implies greater σ values for all values of p, while in the Type II network (Fig. 2.3(h)) higher frequency yields slightly smaller σ values for virtually all values of p. This effect in the Type II network is not due to changes in network firing frequency with changes in p, since average network firing frequency remains virtually constant for all values of p (Fig. 2.3(i)). These results further indicate that for networks of Type II neurons, the increase in network propensity for synchronization due to higher mean firing frequency, and thus higher effective coupling, is offset by reduced cellular propensity for synchronization.

We also investigated how network connection density affects the emergence of network synchrony for the two network types. Figs. 2.5(a) and 2.5(b) depict the differences in mean phase coherence for high- and low-frequency network firing, $\sigma_{\text{high}} - \sigma_{\text{low}}$, as a function of p and the radius of connectivity r, for Type I and Type II networks, respectively. Similar to our previous results in which Type I networks exhibited positive values of $\sigma_{\text{high}} - \sigma_{\text{low}}$ for a bounded range of coupling strength values (Fig. 2.3(c)), Type I networks also show greater synchrony at high frequency than at low frequency between $r \approx 5$ and $r \approx 7$. Type II networks synchronize slightly better at low frequency than at high frequency for $r \gtrsim 2$, which is analogous to the transition that occurs at $s \approx 0.2$ mS/cm^2 in Fig. 2.3(f). These results show that the networks behave in qualitatively the same manner for both increasing r and increasing s, which is not surprising, since the effect of both is a greater exchange of synaptic current

within the network.

2.5 Discussion and summary

The aim of this chapter has been to show the link between frequency modulation of the neuronal PRC and propensity for network synchronization. We investigated these links in the Morris-Lecar neuronal model under two standard excitability regimes, Type I and Type II excitability. For each cell type, as the intrinsic firing frequency of our model neurons increased, phase shifts in spike timing (as measured by the PRC) decreased. This attenuation was uniform across all phases for the Type I cell but not for the Type II cell, which exhibited a greater attenuation of the phase delay region than of the phase advance region. We investigated the effect of this frequency-dependent, gradual abolition of the phase delay region of Type II PRCs upon network synchronization. In large, noisy, excitatory networks, we varied synaptic weight and connectivity architecture across parameter regimes that both prevented and promoted network synchronization. As average network firing frequency was increased by changing the frequency of random excitatory inputs, we observed diminished synchronization (as measured by mean phase coherence) in networks composed of Type II neurons. This phenomenon was robust and can be attributed to the non-uniform, pronounced attenuation of phase delays observed in Type II neurons as frequency increases. In contrast, networks composed of Type I neurons, whose PRCs have no delay region and are uniformly attenuated as frequency increases, showed an increase in propensity for synchronization as frequency increased.

These results paint a complex picture of interactions between network and cellular properties that may lead to nontrivial effects in terms of network dynamical patterns. For example, neurons having various intrinsic cellular properties may be

differentially mixed to form networks having different capacities in terms of their pattern formation. As we have shown, Type I networks have a stronger propensity to synchronize at high compared to low frequencies, whereas Type II networks show the opposite tendency. It is therefore possible that Type I networks function as integrators, while Type II networks may act as low-pass filters in the temporal coding regime.

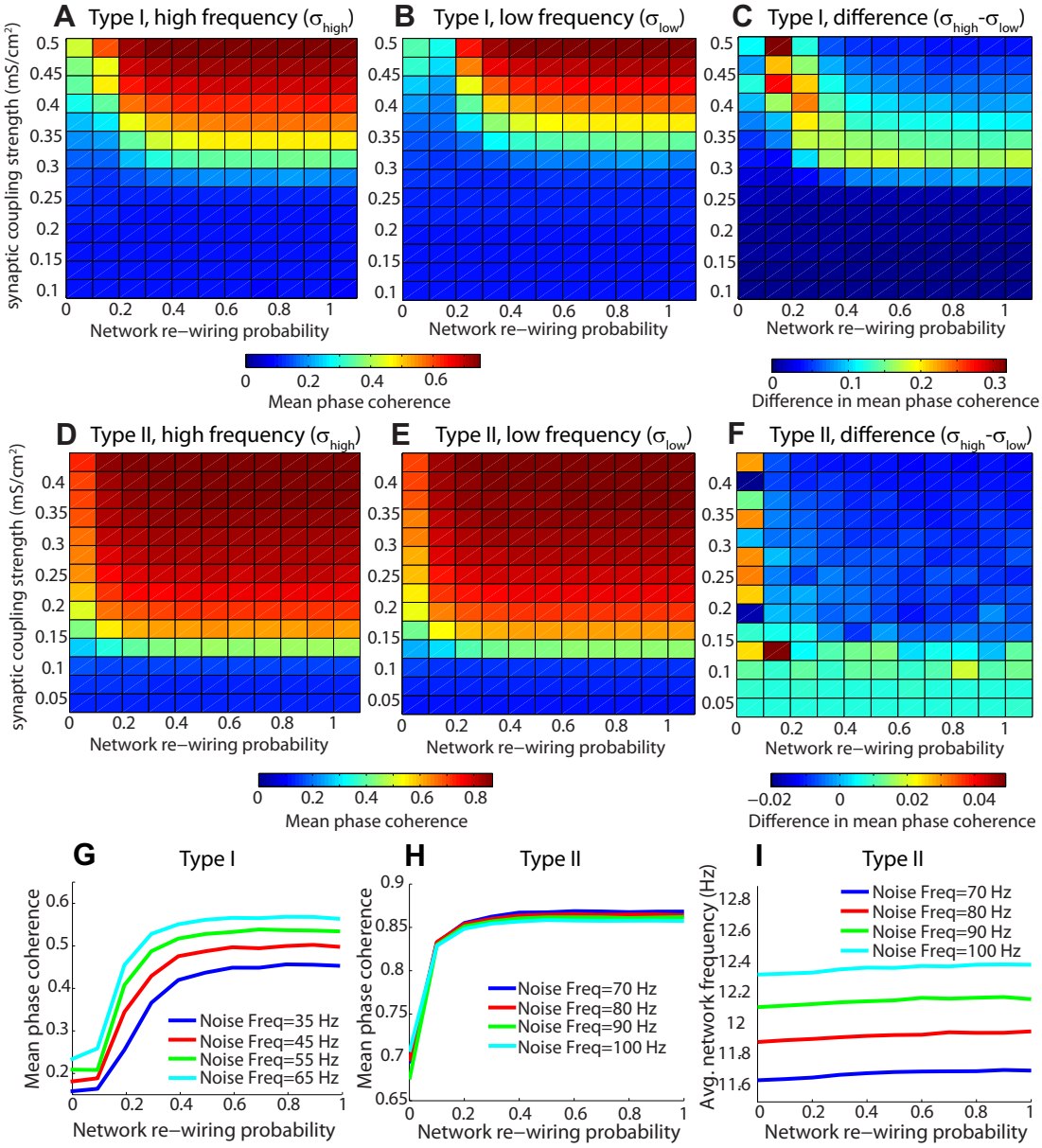

Figure 2.3: (a,b) Mean phase coherence σ as a function of synaptic coupling strength s and re-wiring probability p for networks of Type I neurons driven with a noise frequency of 65 Hz (σ_{high}, a) and of 35 Hz (σ_{low}, b). (c) Difference between the σ values for the high-frequency and low-frequency Type I networks, $\sigma_{\text{high}} - \sigma_{\text{low}}$, as a function of synaptic coupling strength s and re-wiring probability p. (d,e) Mean phase coherence σ as a function of synaptic coupling s and re-wiring probability p for networks of Type II neurons driven with a noise frequency of 100 Hz (σ_{high}, d) and of 70 Hz (σ_{low}, e). (f) Difference between the σ values for the high-frequency and low-frequency Type II networks, $\sigma_{\text{high}} - \sigma_{\text{low}}$, as a function of synaptic coupling strength s and re-wiring probability p. Note the difference in scale between (c) and (f). (g) Cross sections of (a) and (b) with additional, intermediate frequency stimulation values and s fixed at 0.36mS/cm^2. (h) Cross sections of (d) and (e) with additional, intermediate frequency stimulation values and s fixed at 0.36mS/cm^2. (i) Average network firing frequency as a function of p for various values of the noise frequency in a Type II network, with $s = 0.36$mS/cm^2.

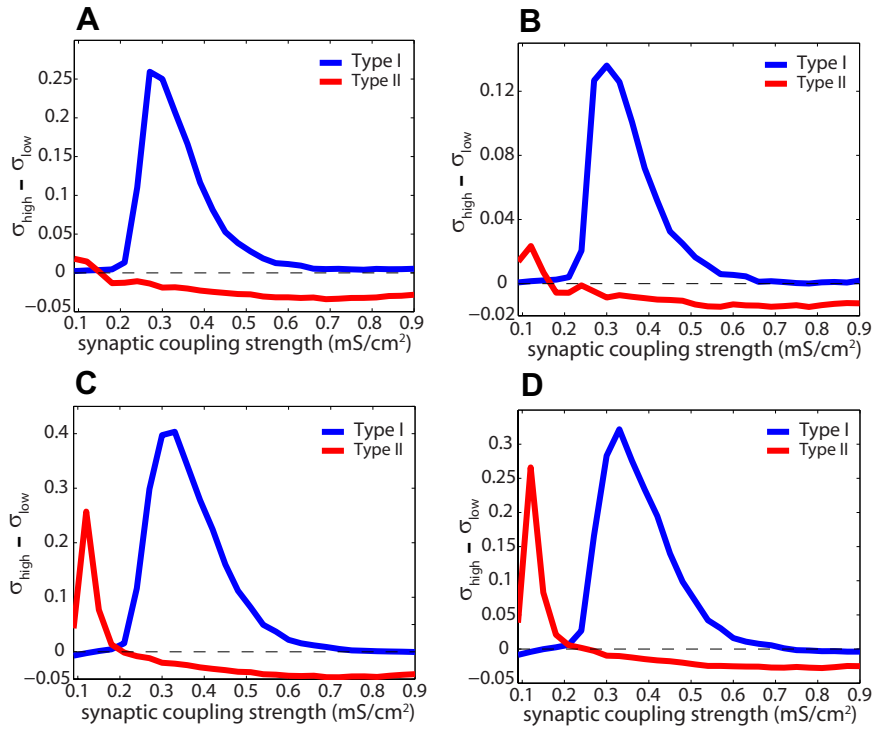

Figure 2.4: Difference in mean phase coherence, $\sigma_{\text{high}} - \sigma_{\text{low}}$, as a function of synaptic coupling s for Type I (blue) and Type II (red) networks driven at high and low noise frequencies of (a) 130 Hz and 60 Hz, (b) 90 Hz and 60 Hz, (c) 130 Hz and 30 Hz, and (d) 90 Hz and 30 Hz, respectively. The network re-wiring probability p is fixed at 0.3.

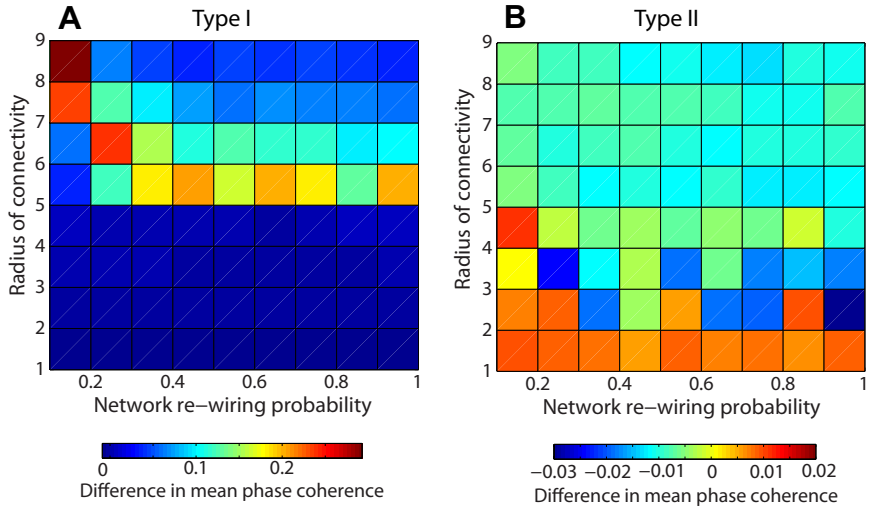

Figure 2.5: (a) Difference in mean phase coherences, $\sigma_{\text{high}} - \sigma_{\text{low}}$, as a function of the radius of connectivity r and the re-wiring probability p in a Type I network. s is fixed at 0.30 mS/cm^2, and the noise frequency is 65 Hz in the high frequency network and 35 Hz in the low frequency network. (b) $\sigma_{\text{high}} - \sigma_{\text{low}}$ as a function of r and p in a Type II network. s is fixed at 0.30 mS/cm^2, and the noise frequency is 100 Hz in the high frequency network and 70 Hz in the low frequency network.

CHAPTER III

Cellularly-driven differences in network synchronization propensity are differentially modulated by firing frequency

3.1 Introduction

In the previous chapter, we showed how the frequency dependence of phase response curves (PRCs) can be used to understand why synchronization responds differently to frequency modulation in Type I networks versus Type II networks. In this chapter, we show why frequency modulation alters neuronal PRCs, and we specifically explain why the phase delay region of Type II PRCs is attenuated more than the phase advance region. In addition to the Morris-Lecar model used previously, we also explore these effects in a more biophysically realistic model of a cortical pyramidal cell. The work presented in this chapter was published as the paper "Cellularly-driven differences in network synchronization propensity are differentially modulated by firing frequency" in the May 2011 issue of *PLoS Computational Biology*. The work was performed in collaboration with Victoria Booth and Michal Zochowski [102].

Neuronal synchronization is thought to underlie spatiotemporal pattern formation in the healthy [103, 104, 105, 106] and pathological brain [32, 107, 108, 109, 110]. The propensity for synchronization in a neuronal network is determined by both cellular and network properties. An important experimentally obtainable measure of cellular properties is the neuronal phase response curve [35]. The PRC characterizes

the change in spike timing of a periodically firing neuron in response to brief, weak external stimulation. PRCs have been classified into two general categories: Type I, which display only phase advances in response to excitatory stimuli, and Type II, which respond with both phase advances and delays. Type I cells exhibit relatively poor propensity for synchronization under excitatory coupling, while Type II cells synchronize better [35, 36, 111, 37, 38, 39, 40, 46]. Furthermore, the PRC characteristics thought to be responsible for synchronization propensity change differentially as a function of frequency for Type I and Type II cells [112]. In this study, we explain the differential effects of frequency modulation on neuronal response properties and exploit these effects to investigate differential changes in the capacity for synchronization of excitatory networks consisting of Type I or Type II neurons.

To demonstrate the universality of the frequency-dependent effects on the neuronal PRC, we consider a reduced model neuron described by the Morris-Lecar equations [99] which can display either a Type I or Type II PRC in different parameter regimes [100]. Then, to present the effects within a physiological context, we turn to the results of a recent experimental study which showed that cholinergic modulation of cortical pyramidal neurons switches the neuronal PRC from Type II to Type I [96]. In a Hodgkin-Huxley-based cortical pyramidal neuron model, the switch in PRC type was shown to depend on a slow, low-threshold potassium current which is targeted by cholinergic modulation [34]. Using these two neuronal models, we explain the underlying cellular basis of the differential frequency effects on the PRC. We show that the relative timing of hyperpolarizing, potassium currents in relation to the model's depolarizing currents (a calcium current in the Morris-Lecar model and a sodium current in the cortical pyramidal cell model) plays a crucial role in shaping the phase response of a neuron. We then investigate the influence of the

frequency-dependent cellular effects on network activity by analyzing network synchronization as a function of underlying neuronal spike frequency near firing threshold in large-scale, excitatory networks composed of either Morris-Lecar neurons or cortical pyramidal model neurons. As expected, the neuronal PRC type profoundly affects network propensity for synchronization [46]. We show that, in general, increasing firing frequency near firing threshold has little effect upon synchrony in Type I networks, while it severely suppresses synchrony in Type II networks. We show these results to be robust to neuronal heterogeneity, network connectivity parameters and whether neuronal activity is driven by constant or stochastic inputs. Our results provide important insight into differential changes in the propensity for network synchronization induced by the external modulation of neuronal frequency. As neuronal firing frequency changes, the changes in network spatiotemporal patterns depend upon the response characteristics of the individual cells in the network.

3.2 Methods

3.2.1 Morris-Lecar neuron model

We used the Morris-Lecar model [99] as a generic neuronal model to initially explore frequency-dependent PRC effects. The model contains two active ionic currents: an inward Ca^{2+} current whose dynamics are instantaneous and an outward K^+ current gated by the dynamic variable w. The current balance equation for the i^{th} cell is

$$C\frac{dV_i}{dt} = -\overline{g}_{Ca} m_\infty(V_i)(V_i - \overline{V}_{Ca}) - \overline{g}_K w(V_i - \overline{V}_K) - \overline{g}_L(V_i - \overline{V}_L) + I_i^{\text{drive}} - I_i^{\text{syn}}, \tag{3.1}$$

where $C = 20.0\ \mu\text{F/cm}^2$, V_i is in millivolts, t is in milliseconds, I_i^{drive} is an externally applied current measured in $\mu\text{A/cm}^2$, and I_i^{syn} is the synaptic current

received by neuron $\imath$. The Ca^{2+} current is governed by the steady-state activation function $m_\infty(V) = 1/2\{1 + \tanh[(V - V_1)/V_2]\}$, while dynamics of the K^+ current gating variable w are given by $dw/dt = \phi(w_\infty(V) - w)/\tau_w(V)$, with $w_\infty(V) = 1/2\{1 + \tanh[(V - V_3)/V_4]\}$ and $\tau_w(V) = \{\cosh[(V - V_3)/(2V_4)]\}^{-1}$.

The Type I and Type II neuronal models share the parameter values $\overline{g}_K = 8.0$ mS/cm^2, $\overline{g}_L = 2.0$ mS/cm^2, $\overline{V}_{Ca} = 120.0$ mV, $\overline{V}_K = -84.0$ mV, $\overline{V}_L = -60.0$ mV, $V_1 = -1.2$ mV, and $V_2 = 18.0$ mV. Type I cells are modeled with $\overline{g}_{Ca} = 4.0$ mS/cm^2, $V_3 = 12.0$ mV, $V_4 = 17.4$ mV, and $\phi = 1/15$, while Type II cells are modeled with $\overline{g}_{Ca} = 4.4$ mS/cm^2, $V_3 = 2.0$ mV, $V_4 = 30.0$ mV, and $\phi = 0.04$. These values were taken from [100].

3.2.2 Cortical pyramidal neuron model with simulated acetylcholine modulation

The cortical pyramidal model neuron we employed was motivated by recent computational and experimental findings, as reported in [34]. Varying the maximum conductance of a K^+-mediated adaptation current, g_{Ks}, from 1.5 mS/cm^2 to 0 mS/cm^2 effectively switches the response characteristics of the cortical pyramidal model neuron from Type II to Type I, a phenomenon which has been observed *in situ* and simulates the effects of cholinergic neuromodulation [96]. The model also features a fast, inward Na^+ current, a delayed rectifier K^+ current, and a leakage current, in addition to the aforementioned slow, low-threshold K^+ current responsible for spike-frequency adaptation [34, 113]. The current balance equation for the $\imath^{\text{th}}$ cell is

(3.2)
$$C\frac{dV_\imath}{dt} = -g_{Na}m_\infty^3(V_\imath)h(V_\imath - V_{Na}) - g_{Kdr}n^4(V_\imath - V_K) - g_{Ks}z(V_\imath - V_K) - g_L(V_\imath - V_L) + I_\imath^{\text{drive}} - I_\imath^{\text{syn}},$$

with $C = 1.0$ μF/cm^2, $V_\imath$ in millivolts, and t in milliseconds. $I_\imath^{\text{drive}}$ is an externally

applied current measured in μA/cm^2, and $I_\imath^{\text{syn}}$ is the synaptic current received by neuron $\imath$. Activation of the Na^+ current is instantaneous and governed by the steady-state activation function $m_\infty(V) = \{1 + \exp[(-V - 30.0)/9.5]\}^{-1}$. Dynamics of the Na^+ current inactivation gating variable h are given by

$$dh/dt = \alpha_h(h_\infty(V) - h)/\tau_h(V), \tag{3.3}$$

with $h_\infty(V) = \{1 + \exp[(V + 53.0)/7.0]\}^{-1}$ and $\tau_h(V) = 0.37 + 2.78\{1 + \exp[(V + 40.5)/6.0]\}^{-1}$. The delayed rectifier K^+ current is gated by n, whose dynamics are governed by

$$dn/dt = (n_\infty(V) - h)/\tau_n(V), \tag{3.4}$$

with $n_\infty(V) = \{1 + \exp[(-V - 30.0)/10.0]\}^{-1}$ and $\tau_n(V) = 0.37 + 1.85\{1 + \exp[(V + 27.0)/15.0]\}^{-1}$. The slow, low-threshold K^+ current targeted by cholinergic modulation is gated by z, which varies in time according to

$$dz/dt = \alpha_z(z_\infty(V) - z)/75.0, \tag{3.5}$$

where $z_\infty(V) = \{1 + \exp[(-V - 39.0)/5.0]\}^{-1}$. The parameters α_h and α_z in the current gating equations are varied in the investigation of the underlying cellular basis of the differential frequency effects on the PRC, but they are set to $\alpha_h = \alpha_z = 1$ in the network simulations. The slow, low-threshold K^+ current loosely models the muscarine-sensitive M-current observed in cortical neurons. It has been shown *in silico* that eliminating this current is sufficient to switch the model neuron's PRC from Type II to Type I [34]. This is intended to model cholinergic neuromodulation, which

has been shown experimentally to switch cortical pyramidal neurons between Type I and Type II phase responses [96]. This switching of PRC profile is demonstrated in Fig. 1, and is obtained by setting $g_{Ks} = 0.0$ mS/cm^2 to obtain a Type I response (simulated cholinergic modulation) and $g_{Ks} = 1.5$ mS/cm^2 to obtain a Type II response (simulated absence of cholinergic modulation). All other parameter values are the same for both types of neurons: $g_{Na} = 24.0$ mS/cm^2, $g_{Kdr} = 3.0$ mS/cm^2, $g_L = 0.02$ mS/cm^2, $V_{Na} = 55.0$ mV, $V_K = -90.0$ mV, and $V_L = -60.0$ mV.

3.2.3 PRC Calculation

For both neuronal models, I^{drive} is set to a fixed value to elicit repetitive firing in a single, synaptically isolated neuron, and the model equations are time evolved using a fourth-order Runge-Kutta numerical scheme until the oscillatory period stabilizes. Then, using initial conditions associated with spike peak, brief current pulses are administered at different phases of the oscillation, and the perturbed periods are used to calculate the corresponding phase shifts. The current pulses are administered at 100 equally-spaced time points throughout the period of the neuronal oscillation. The current pulses have a duration of 0.06 ms and an amplitude of 3.0 μA/cm^2 for the Type I cortical pyramidal neuron, a duration of 0.06 ms and an amplitude of 10.0 μA/cm^2 for the Type II cortical pyramidal neuron, and a duration of 0.50 ms and an amplitude of 100.0 μA/cm^2 for both the Type I and Type II Morris-Lecar neurons.

3.2.4 Network simulations

In all network simulations, the number of neurons is 200, and the synapses are exclusively excitatory. The network connectivity pattern is constructed using the Watts-Strogatz architecture for Small World Networks [50]. Starting with a 1-D ring

network with periodic boundary conditions, each neuron is at first directionally coupled to its $2r$ nearest neighbors, and then every connection in the network is rewired with probability p to another neuron selected at random. In this way, $p = 0$ results in a locally-connected network and $p = 1$ in a randomly connected network. The radius of connectivity r therefore determines the density of connections in the network, while the re-wiring parameter p determines the network connectivity structure. Network connectivity r is set to 4 in all simulations. Synaptic current is transmitted from neuron $\jmath$ at times $t_\jmath$ when its membrane voltage breaches -20 mV. The synaptic current delivered from neuron $\jmath$ to a synaptically connected neuron $\imath$ at times $t >= t_\jmath$ is given by $I_{\imath\jmath}^{\text{syn}} = s \exp\left(-\frac{t-t_\jmath}{\tau}\right)(V_\imath - E_{\text{syn}})$. The total synaptic current to a neuron $\imath$ is simply given by $I_\imath^{\text{syn}} = \sum_{\jmath\in\Gamma_\imath} I_{\imath\jmath}^{\text{syn}}$, where $\Gamma_\imath$ is the set of all neurons which synapse onto neuron $\imath$. The synaptic weight s is the same for all synapses within a given simulation, and we set $\tau = 0.5$ ms and $E_{\text{syn}} = 0$ mV. All simulations are run for 10,000 ms, with the first 3000 ms disregarded in order to eliminate initial transient effects. The dynamics are numerically integrated in Matlab using a fourth-order Runge-Kutta method with a time step of 0.05 ms for the cortical pyramidal neuron networks and 0.10 ms for Morris-Lecar neuron networks. We employ two different methods to modulate network firing frequency in our simulations. The first is to simply modulate the supra-threshold value of I^{drive} for all neurons in the network. In order to prevent the networks from trivially synchronizing, we do not supply each neuron with exactly the same level of current, but instead sample from a Gaussian distribution of current values. The mean value of the distribution determines the average firing frequency of the network, and the standard deviation of the Gaussian is chosen such that the standard deviation in natural neuronal frequencies is 1 Hz. In order to model more biologically relevant environmental inputs, we also

run simulations of cortical pyramidal neuronal networks in which frequency is modulated by stochastic input. All neurons are given the same constant sub-threshold baseline current, plus square current pulses randomly delivered to each neuron at a specified frequency f_{noise}, so that $I_i^{\text{drive}} = I_{\text{base}} + I_i^{\text{noise}}(f_{noise})$. The delivery of the square current pulses is a Poisson process. Modulation of this noise frequency thereby modulates the average frequency of the network. In our simulations of stochastically-driven cortical pyramidal neuronal networks, I_i^{noise} consists of square current pulses with amplitude 30 μA/cm^2 and duration 0.2 msec. With these values, at least two successive pulses are required to elicit neuronal firing. The baseline currents are $I_{\text{base}} = -0.16$ μA/cm^2 for Type I networks and $I_{\text{base}} = 0.0$ μA/cm^2 for Type II networks. We monitor phase-synchronization of neuronal firing in our simulations using the mean phase coherence (MPC) measure, σ [101]. This measure quantifies the degree of phase locking between neurons, assuming a value of 0 for completely random spiking and 1 for complete phase locking. Note that MPC may be attained for locking of phases at *any value*, not just zero. The MPC between a pair of neurons, $\sigma_{1,2}$, is defined by:

$$\sigma_{1,2} = \left| \frac{1}{N} \sum_{k=1}^{N} e^{i\phi_k} \right| \tag{3.6}$$

$$\phi_k = 2\pi \left(\frac{t_{2,k} - t_{1,k}}{t_{1,k+1} - t_{1,k}} \right), \tag{3.7}$$

where $t_{2,k}$ is the time of the k^{th} spike of neuron 2, $t_{1,k}$ is the time of the spike of neuron 1 that is largest while being less than $t_{2,k}$, $t_{1,k+1}$ is the time of the spike of neuron 1 that is smallest while being greater than or equal to $t_{2,k}$, and N is the number of spikes of neuron 2. The MPC of the entire network, σ, is calculated by averaging $\sigma_{i,j}$ over all pairs of neurons, excluding $\imath = \jmath$. Note that this measure is

not symmetric. We quantify phase-zero synchronization of a network by calculating the bursting measure B, which is 0 for random spiking and approaches 1 for perfect locking at phase zero between all neurons, for a large number of total spikes and neurons. Calculation of B requires a time-ordered list of the spike times of all neurons over the duration of the entire simulation [114]. Denoting as τ_i the time difference between spikes i and $i+1$, which do not necessarily (and probably do not) correspond to spikes of the same neuron, B is then defined as

$$B = \left(\frac{\sqrt{\langle \tau^2 \rangle - \langle \tau \rangle^2}}{\langle \tau \rangle} - 1 \right) \frac{1}{\sqrt{N}}, \tag{3.8}$$

where $\langle\rangle$ represents averaging over all spikes. This measure makes use of the fact that an ensemble of spike time intervals will have a larger standard deviation in a synchronous signal than in an asynchronous signal. In our simulations, both the mean phase coherence and the bursting parameter are calculated for neuronal activity from 3000 ms to 10,000 ms, unless otherwise noted.

3.3 Results

We first investigate the underlying cellular basis of the differential frequency effects on Type I and Type II PRCs. We show that the relative activation levels and timing of hyperpolarizing, potassium currents in relation to depolarizing currents play a crucial role in shaping the phase response of a neuron. We then show that individual neuronal spiking frequency modulates network synchrony in significantly different ways for networks consisting of Type I or Type II cells. Specifically, synchrony in Type I networks is affected very little by frequency modulation near threshold, whereas in Type II networks, synchrony falls dramatically as frequency increases above firing threshold. This effect is due to the disparity in the frequency-modulated attenuation of the PRCs of the two cell types. We first show this effect in

excitatory networks composed of Morris-Lecar model neurons, and then investigate it in depth for excitatory networks consisting of model cortical pyramidal cells under acetylcholine modulation.

3.3.1 Frequency modulation of neuronal phase responses

Fig. 3.1 displays the response properties of the model neurons in our simulations, with Fig. 3.1(a,d) showing the frequency-current curves of the model neurons and Fig. 3.1(b,c,e,f) showing the PRCs of the model neurons. Type I PRCs in both the Morris-Lecar and the cortical pyramidal neuron models exclusively display phase advances (positive PRC values) in response to excitatory perturbations (Fig. 3.1(b,e)) while Type II PRCs show phase delays (negative PRC values) at earlier phases and advances at later phases (Fig. 3.1(c,f)). (Note that the presence of small negative regions early in Morris-Lecar PRCs and the absence of such regions in cortical pyramidal cell PRCs is a consequence of the fact that spikes consume a much larger portion of the interspike interval in the Morris-Lecar model than in the cortical pyramidal cell model [100]. We therefore ignore these early regions in Morris-Lecar PRCs.) The switch from Type I to II is induced by changes in the steady state activation function of the K^+ current in the Morris-Lecar model and by the presence of the slow, low-threshold K^+ current in the cortical pyramidal cell model. A categorization of Type I and Type II can also be applied to a neuron's frequency-current (f-I) relation, with Type I f-I curves exhibiting arbitrarily low frequencies at firing thresholds and Type II f-I curves showing a finite, non-zero firing frequency at threshold. While the categorization of a neuron's PRC and f-I curve are not necessarily the same, and the relationship between the curves has not been completely determined [115], for both models considered here, PRC and f-I curve types coincide (Fig. 3.1(a,d)).

In both models, increasing frequency by increasing the constant applied current results in an attenuation of phase responses (Fig. 3.1). This attenuation occurred in qualitatively different ways for Type I and Type II neurons. In the Type I model neurons, increased firing frequency led to diminished phase advances but did not change the relative shape of the curves–they all remained distinctly Type I (Fig. 3.1(b,e)). In the Type II model neurons, however, there was much greater attenuation of the phase-delay region compared to the phase-advance region (Fig. 3.1(c,f)). This asymmetric attenuation can affect synchronization properties because the phase-delay region contributes to the increased propensity for synchronization in Type II excitatory networks [111]. Previously, the emergence of phase delay regions at low firing frequencies was attributed to decreased activation of K^+-mediated adaptation currents at low frequencies [111, 112], but this explanation cannot apply to the Morris-Lecar model, since it contains no adaptation currents. Below we discuss the properties of a cell's hyperpolarizing and depolarizing currents that are responsible for its phase response, and which explain the observed frequency-dependent attenuation.

In both models, phase delays exist in the Type II parameter regimes because there is a voltage interval in which activation of an outward, hyperpolarizing current is greater than activation of the inward, depolarizing current. In the Type II Morris-Lecar model, the steady state activation curve of the K^+ current, $w_\infty(V)$, is shifted to the left and steeper compared to that of the Ca^{2+} current, $m_\infty(V)$, thus providing for this voltage interval. In the Type II cortical pyramidal neuron model, the steady state activation curve, $z_\infty(V)$, of the slow, low-threshold K^+ current (which is absent in the Type I neuron), is similarly shifted to the left relative to the steady-state activation curve of the Na^+ current, $m^3_\infty(V)$. In either model, as the voltage trajectory passes through the early part of the interspike interval, a brief, excitatory stimulus will

induce a larger response from the lower-threshold K^+ current than from the inward current, resulting in negative values of the PRC at early phases. At higher voltage levels later in the interspike interval, the inward current dominates the response to the brief stimulus due to its faster (instantaneous) activation dynamics, thus leading to advances in the cycle, and positive values of the PRC at later phases. As firing frequency increases, the cycle trajectory passes through this K^+-dominant voltage interval at a faster rate, thus preventing the full K^+ response from developing before reaching voltage levels where the instantaneous inward current can respond. The delaying K^+ response to the brief stimulus is thus diluted by the advance-promoting inward current response, and phase delays are attenuated. This attenuation of phase delays is therefore the result of a disparity between the *fixed* dynamics of the delay-inducing K^+ current and the time afforded that current to act by the *shrinking* interspike interval. Phase advances are less sensitive to frequency modulation since the instantaneous dynamics of the inward currents in both models can directly track the faster cycle trajectory.

We further illustrate this point by modulating the speed of the gating variable controlling the delay-inducing potassium current in each model. Fig. 3.2(a) demonstrates that in the Morris-Lecar model, increasing ϕ, which increases the rate of the K^+ gating variable w, results in an increase in the amplitude of PRC phase delays, while decreasing ϕ has the opposite effect. Faster K^+ dynamics allow for faster development of the delaying K^+ response to the excitatory stimulus. In this model, modulating ϕ also changes the voltage levels during the interspike interval, which can shift the K^+ dominant voltage interval to different phases. We systematically quantify the contribution of K^+ dynamics to the generation of the phase delay by measuring the changes in the PRC delay depth as a function of ϕ for neurons re-

ceiving different driving currents and thus exhibiting different intrinsic frequencies (Fig. 3.2(b)). The depth of the PRC delay region increased with increasing ϕ for all levels of external current, and faster-firing neurons could display similar delay depths as slower-firing neurons with appropriate increases in ϕ. While increasing ϕ also acted to increase firing frequency (Fig. 3.2(c)), phase delay amplitudes nonetheless increased, indicating that speeding up the rate of K^+ dynamics exerts a stronger effect on the phase delay than does the accompanying frequency increase. A similar dependence of phase delay amplitude on the rate of the gating variable z for the slow, low-threshold K^+ current in the cortical pyramidal cell model is shown in Fig. 3.2(d,e). As the rate of z dynamics increased (i.e., as α_z increased in Eq. 4.4), depths of the PRC delay increased due to the ability of the K^+ current to develop a delaying response before voltage levels were reached where the Na^+ current activated. Again, increasing the rate of z dynamics caused an increase in frequency (Fig. 3.2(f)), but the faster development of the K^+ response to the perturbation could overcome a frequency-induced attenuation of phase delays. In this model, voltage levels during the interspike interval also changed with the changes in α_z, but they did not greatly influence the phase of maximal delays. In the cortical pyramidal neuron model, the amplitude of phase delays also depended on the rate of the Na^+ current inactivation (Fig. 3.2(g-i)), gated by the variable h in Eq. 4.1. Slower Na^+ inactivation, induced by lower values of α_h in Eq. 4.2, allowed larger Na^+ responses to the perturbing stimulus, which diluted the delaying effect of the K^+ response and therefore attenuated phase delays. The rate of Na^+ inactivation had little effect on voltage levels as a function of phase during the interspike interval, and only slightly affected the frequency. Increasing the rate of Na^+ inactivation did induce a decrease in firing frequency, which would promote the observed increase in delay depth, but these

changes to firing frequency were too slight to be the primary cause of the enlarged delay amplitude.

These results imply that appropriate selection of the rate of variables gating the intracellular currents mentioned above permits the recovery of specified PRC delay depths for different levels of external current. Fig. 3.3 illustrates this effect for both models. From the curves in Fig. 3.2(b,e,h), appropriate rates of the gating variables were separately selected for each level of external current to induce delay depths of 0.04 in the Morris-Lecar neuron and 0.025 in the cortical pyramidal neuron. In the Morris-Lecar model, the maximal phase delay region was shifted to the left as the external current increased because the voltage trace was similarly shifted (Fig. 3.3(a,d)). However, in the cortical pyramidal cell model, the PRC profiles were virtually identical for different levels of external current, both when the slow potassium current was modified and when the sodium inactivation was modified (Fig. 3.3(b,c)). This was due to the fact that the voltage traces (plotted as a function of oscillatory phase) were not shifted when either of these intracellular currents were altered (Fig. 3.3(e,f)). The invariance of the voltage traces in the cortical pyramidal cell model is an interesting phenomenon, but it is beyond the scope of this chapter.

3.3.2 Network correlates of PRC modulation

Morris-Lecar neuron network driven by constant applied currents

We analyzed network activity patterns in large-scale (N=200) excitatory networks composed of Morris-Lecar model neurons with Type I and Type II PRCs under different network connectivity regimes. As described in the Methods section, randomness of network connectivity was determined by the small-world "re-wiring parameter." Network activity was modulated by altering the mean applied current given to each neuron, and neuronal heterogeneity was enforced by selecting applied current values

from a Gaussian distribution centered on the specified mean. Fig. 3.4(a,b) show that increased mean applied current generally led to increased network frequency. Effects of the frequency-dependence of PRCs upon network synchrony are evident in Fig. 3.4(c,d), which plot phase-zero synchronization, as measured by the bursting measure B, versus the re-wiring parameter for different network frequencies. In Type I networks, increased neuronal firing frequency had little effect upon synchronization, while synchronization of Type II networks substantially *decreased* with increased neuronal firing rates. Fig. 3.4(e,f) show that phase locking of the networks, as measured by mean phase coherence (MPC), painted a similar picture. For a given value of the re-wiring parameter, increased frequency had very different effects upon Type II networks in comparison to Type I networks. In fact, for $0.2 \lesssim p \lesssim 0.4$, Type I network MPC discernably increased with increased frequency, showing exactly the opposite trend as Type II networks.

Cortical pyramidal neuron network driven by constant applied currents

We first investigated synchronization properties of networks driven with constant applied currents, as in the Morris-Lecar network simulations. Every cell was driven with a constant current, I^{drive}, whose value was chosen from a Gaussian distribution with specified mean. This mode of driving neuronal activity reflected the conditions under which the PRC is generally computed. Fig. 3.5(a,d) show that increasing the mean value of I^{drive} typically led to an increase in the average network firing frequency, as expected.

We observed sharp differences between responses of the Type I and Type II networks to frequency modulation. As shown in Fig. 3.5(b), the bursting parameter tended to increase only slightly with increased applied current in Type I networks, while Fig. 3.5(e) shows that in Type II networks the phase-zero synchronization

substantially decreased as applied current increased. This same trend was seen in the phase locking of the networks, albeit to a lesser degree, as shown in Fig. 3.5(c,f). The large drop in MPC shown in Fig. 3.5(c) was due to the disruption of propagating waves as long-range connections were introduced into the network. This drop in synchrony in turn explains the large increase in frequency over the same range of the re-wiring parameter (Fig. 3.5(a)), since each neuron then receives a steady barrage of input, rather than punctuated bursts of input.

To show that these results were robust to network structure and coupling strength, Fig. 3.6 displays how the bursting measure B varied with the re-wiring parameter and synaptic weight in both types of networks. Note that synaptic weights were much higher in Type I than in Type II networks because Type I networks required greater coupling in order to reach appreciable levels of synchronization. The left panels in Fig. 3.6(a,b) show the values of the bursting parameter corresponding to high-frequency networks ($I^{\text{drive}} = 0.20$ μA/cm^2 for Type I and $I^{\text{drive}} = 1.40$ μA/cm^2 for Type II), while the center panels show the data corresponding to low-frequency networks ($I^{\text{drive}} = -0.10$ μA/cm^2 for Type I and $I^{\text{drive}} = 1.20$ μA/cm^2 for Type II). The right panels show the difference in B between the high- and low-frequency networks for each network type, revealing the fundamental difference in synchronization response of the two types of networks. The right panel in Fig. 3.6(a) shows values very near zero for most of the parameter landscape, with a few slightly positive values sprinkled throughout, indicating that Type I network synchrony was largely unaffected by increased frequency, and that when increasing frequency did have an effect, it generally increased synchrony. In Type II networks, on the other hand, differences in bursting values were negative for values of s greater than approximately 0.020 mS/cm^2 and values of the re-wiring parameter greater than approximately 0.10.

These values correspond to the parameter space in which appreciable synchronization occurred and in which propagating waves were precluded, indicating that Type II networks synchronized much better at lower frequencies for non-trivial network parameters. For many Type II network parameters, the difference in synchronization between high- and low-frequency networks was evident from the activity patterns alone (see Fig. 3.6(e,f)), while differences in Type I network synchrony were not so obvious (as in Fig. 3.6(c,d)).

Time to synchronization In the high-coupling regime, where differences in steady-state synchronization between high- and low-frequency Type II networks were diminished, we investigated whether frequency might still affect the *time* to synchronization. In the right panel of Fig. 3.6(b), it is clear that the magnitude of the difference between high- and low-frequency values of B in Type II networks decreased above approximately $s = 0.06\text{mS/cm}^2$. This was a saturation effect; regardless of the level of applied current, there was a ceiling of $B \approx 0.8$ which was not breached, and as the differentially-driven networks approached this limit, the differences in their steady-state values of B diminished. This effect is displayed in the tightly-packed values of B shown in Fig. 3.7(a). Despite this fact, our simulations showed that in this regime there was still a major difference between the differentially-driven networks: the time to synchronization. As Fig. 3.7(b) shows, when started with random initial conditions, Type II networks synchronized more quickly when driven with lower levels of applied current, even when there was very little difference between the levels of steady-state synchrony. This further underscores the enhanced synchronization properties that Type II networks exhibited at lower frequency.

Finally, Fig. 3.8 also supports the previously-presented trends. The differences in

MPC between high- and low-frequency Type I networks were almost all very close to zero, while in the Type II networks there was a very significant region in which the MPC differences were negative. This negative region did not occupy as large an area in parameter space as it did for the bursting parameter, but that was due to the fact that the MPC saturated much more quickly than did the bursting parameter.

Cortical pyramidal neuron network driven by stochastic input currents

After we demonstrated the distinct synchronization response properties of Type I and Type II networks stimulated by varing levels of constant current, we next investigated the more biologically relevant context of stochastic stimulation. Here random current pulses were used to simulate neuronal drive coming from other brain modalities. Fig. 3.9 shows, as we would expect, that average network firing frequency consistently increased with f_{noise}, the average frequency at which sub-threshold current pulses were stochastically applied (see Methods for a more detailed description of this process), but remained largely independent of the network re-wiring parameter.

The synchronization responses of the networks to frequency modulation were very similar to those described previously. The differences in bursting measure B between high- and low-frequency Type I networks were again very small for virtually all values of the network re-wiring parameter and coupling strength (Fig. 3.10(a)). The Type II networks, on the other hand, transitioned to synchrony at approximately $s = 0.14$ mS/cm^2 for almost all values of the re-wiring parameter (data not shown), at which point the differences in B became very negative (Fig. 3.10(b)), indicating once again that Type II networks were very sensitive to frequency modulation and that they had greater propensity for synchronization at low frequencies. Fig. 3.10(c,d) further illustrate the effect of increased frequency upon network synchrony for a particular value of the synaptic coupling.

Phase locking again largely followed the same trend as bursting, with the difference in MPC assuming values near zero for most of parameter space in Type I networks (Fig. 3.10(e)). The few very negative values seen, for high coupling and low re-wiring values, were most likely due to wave-propagation effects. Fig. 3.10(f) shows that Type II networks underwent a transition in MPC at $s = 0.14$ mS/cm^2, the same value at which the bursting values transitioned. Line plots for the MPC at this synaptic coupling value clearly demonstrate the increased propensity for synchronization at low frequency for Type II networks (Fig. 3.10(h)), while Fig. 3.10(g) shows the insignificant effect of frequency modulation upon Type I MPC.

3.4 Discussion and summary

We have shown that excitatory networks composed of neurons with either Type I or Type II PRC properties respond very differently to frequency modulation near firing threshold, with Type I network synchrony remaining largely unaffected by frequency modulation and Type II networks synchronizing much better at lower frequencies. This result is robust in virtually all network parameter regimes in which the network is capable of attaining any appreciable level of synchronization. While both Type I and Type II PRCs are modified by changes in frequency, only Type II PRCs change in qualitative profile. Specifically, the phase delay region, which is known to be critical in promoting synchrony, is severely attenuated. Increased frequency therefore tends to have little effect upon Type I networks, since there is no change in the PRC's contribution to synchrony, while in Type II networks it leads to depressed synchrony via the diminished phase delay region of the PRC. It should be noted that our simulations agreed with a large body of previous work showing that neurons with Type II membrane dynamics (as defined by the frequency-current

curve) tend to synchronize better than neurons with Type I membrane dynamics, when coupled with excitation. Previous theoretical work indicates that when excitatory networks are driven with constant current, those composed of Type I neurons will not synchronize as well as those composed of Type II neurons [35, 36, 116], a phenomenon which we observed in our simulations, since much larger synaptic coupling values were required in Type I networks to evoke levels of synchrony equivalent to those in Type II networks (Fig. 3.6). Previous theoretical [117] and experimental [118] work has also shown that neurons with Type I membrane dynamics respond to excitatory noisy input with much higher spike-time variability than do neurons with Type II membrane dynamics. This accords with the results of our simulations of networks stimulated by noisy current pulses, where again we saw that greater synaptic coupling was needed for Type I networks to synchronize as well as Type II networks (Fig. 3.10). In this chapter, we focused on the implications for network synchronization of the observed frequency-dependence of PRCs. Our results suggest that the severe attenuation of the phase-delay region of Type II PRCs at increased firing frequencies contributes to the observed decline in network synchronization at such frequencies. Frequency-dependent modification of PRCs has been investigated before in complex, multi-compartment neuronal models [119, 97], but such results rely on dendritic effects and hence do not apply to our results using single-compartment neurons. It has been shown in a simple θ-neuron model that low-threshold adaptation currents can produce negative regions in the PRC at low frequency [112], an effect which is probably due to the change in bifurcation structure induced by such currents [111]. From this perspective, the delay region of the PRC develops only at low frequency because the adaptation current is saturated at high frequency, resulting in its responding to excitatory stimulation with relatively smaller

transient increases. Our work extends this insight by explaining the emergence and attenuation of delay regions in the PRCs of Morris-Lecar neurons, which have no adapting current. Our explanation applies to the cortical pyramidal model neuron, which does feature an adapting current, as well: it is the speed of low-threshold, hyperpolarizing currents relative to the interspike interval which determines the depth of the PRC delay region in Type II cells. For a fixed level of external current, the faster we made the K^+ current in the Morris-Lecar neuron and the adapting K^+ current in the cortical pyramidal neuron, the larger their PRC delay depths grew. It is therefore not only the saturation level of low-threshold, hyperpolarizing currents that is important, but also the speed with which they can respond to brief stimulation. In addition, our simulations showed that the PRC delay depth is not exclusively controlled by the effects of hyperpolarizing currents, but can be greatly affected by depolarizing currents as well. The faster we made the deactivation of the sodium current, the larger the delay depth grew, underscoring once again the importance of the speed of intracellular currents relative to the interspike interval. The frequency-dependent synchronization which we have described in this chapter could potentially be involved in any cognitive process, functional or pathological, which involves spatiotemporal pattern formation of neuronal populations. For example, cholinergically-induced switching between sensitivity and insensitivity to frequency modulation could be important in proper memory consolidation during slow wave and REM sleep, two states that are characterized by differing levels of acetylcholine in cortical and hippocampal regions. Frequency-mediated synchrony could also play a part in the binding of signals from multiple sensory modalities. Gamma oscillations (20-80 Hz) in cortical networks are believed to be generated by synchronous activity of fast-spiking interneurons [120], which generally exhibit Type II frequency-current

relations and PRC profiles [118, 115]. While excitatory and inhibitory synaptic connections and gap junctions may participate in the synchronous firing of interneuron networks [121, 122, 123, 124], our results suggest the importance of the cellular properties of the fast-spiking interneurons in generating synchrony. Additionally, the frequency-dependence of synchronization may provide a means to restrict synchronization to specific frequency bands. Finally, frequency modulation could contribute to the onset of epileptiform activity, and our results might help to explain recent evidence that synchrony decreases during seizures [30, 125]. At the same time, the importance of our results is not confined to these examples alone. Our findings point to the possibility that Type I and Type II excitatory networks function in two separate coding regimes, with Type I networks functioning in the rate coding regime and Type II networks functioning in the temporal coding regime, effectively acting as low-pass filters. Further experimental investigation into the interplay between cellular properties, frequency, and network synchronization is clearly required.

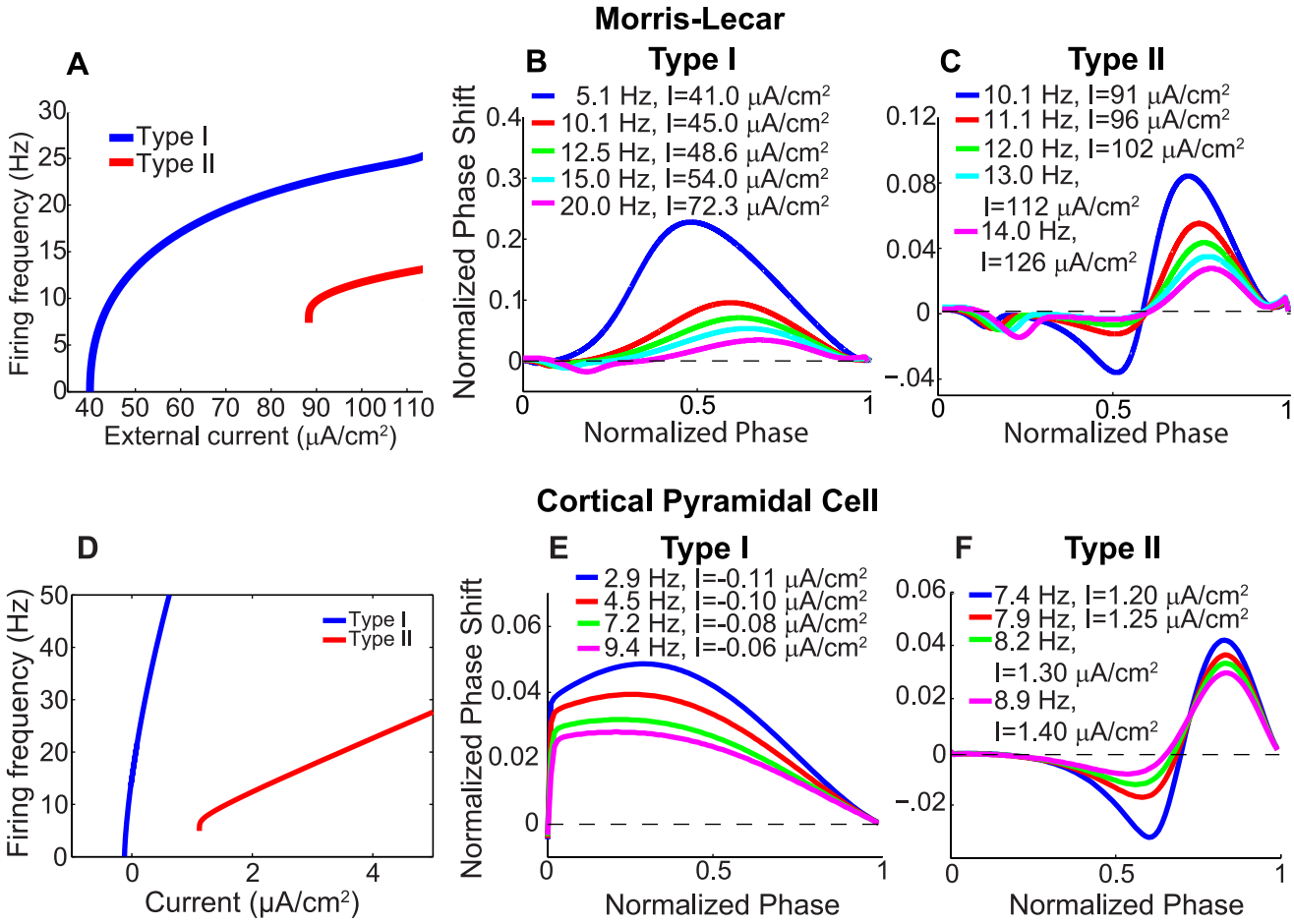

Figure 3.1: (a) Frequency-current curve for Type I and Type II Morris-Lecar model neurons. Note that the Type I cell can fire at arbitrarily low frequencies, while the Type II cell exhibits a non-zero frequency threshold. (b,c) Frequency dependence of PRCs for Morris-Lecar model neurons with Type I and Type II response characteristics. When the PRC was computed at different neuronal firing frequencies (different curves), amplitudes of phase shifts were attenuated, and the Type II neuron showed asymmetric attenuation of the phase advance and phase delay regions. (d) Frequency-current curves for Type I ($g_{Ks} = 0$ mS/cm^2, cholinergic modulation) and Type II ($g_{Ks} = 1.5$ mS/cm^2, no cholinergic modulation) cortical pyramidal model neurons. The Type I neuron could fire at arbitrarily low frequencies, while the Type II neuron exhibited a threshold frequency of approximately 8 Hz. (e) PRCs for different firing frequencies of the Type I cortical pyramidal neuron. (f) PRCs for different firing frequencies of the Type II cortical pyramidal neuron. In both models, the Type I cells exhibited global attenuation of the phase responses, while increased firing frequency evoked asymmetric attenuation in the phase delay region as compared to the phase advance region in Type II cells.

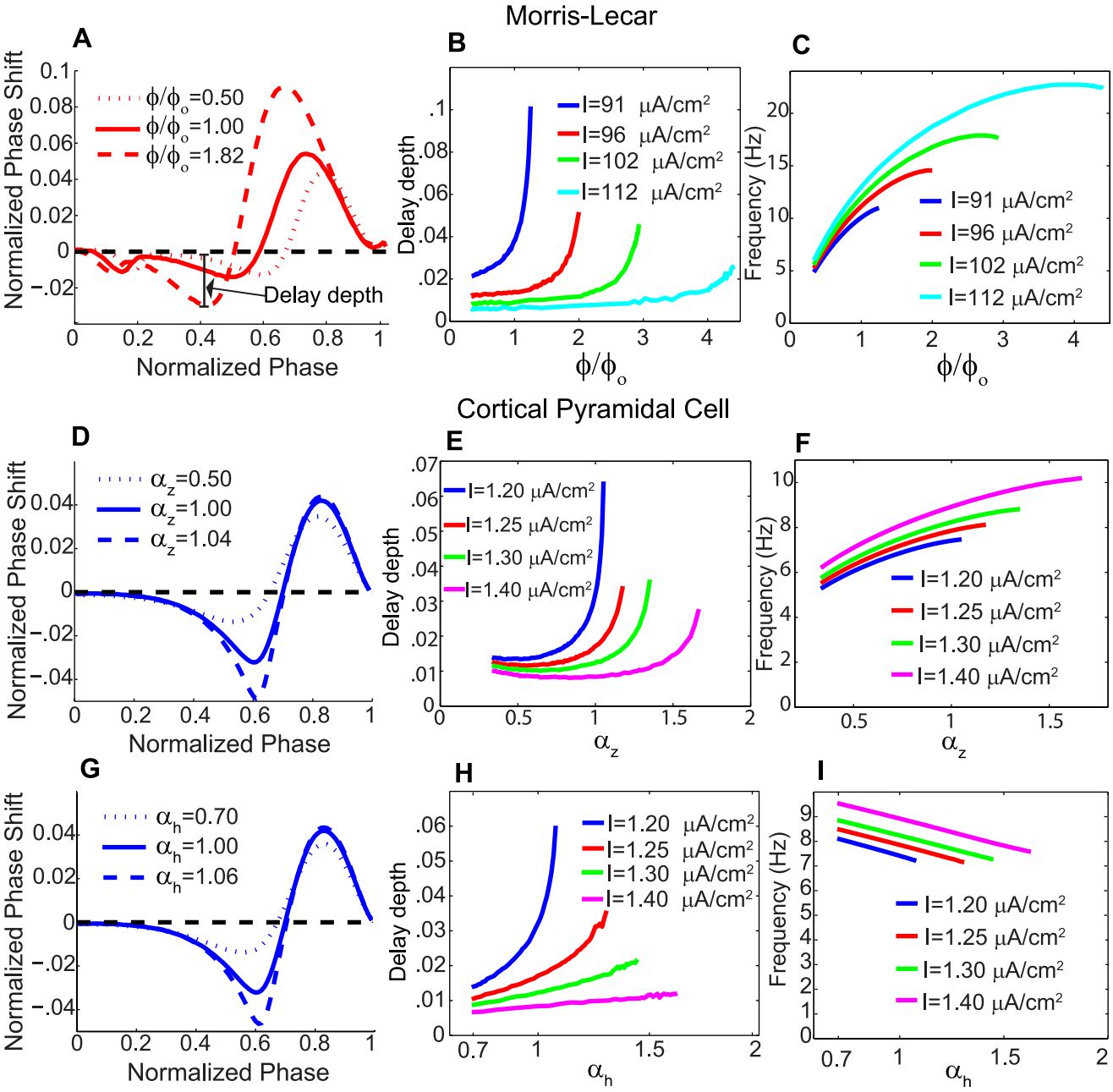

Figure 3.2: (a-c) Effects of modifying the speed of the potassium current in the Type II Morris-Lecar neuron, with increasing values of ϕ/ϕ_0 implying faster dynamics ($\phi_0 = 0.04$). (a) PRCs of the neuron for three sample values of ϕ/ϕ_0, with $I^{drive} = 96.0\ \mu A/cm^2$. As the speed of the potassium dynamics increases, the PRC delay depths grow progressively larger. (b) Absolute value of the delay depth of the PRCs as a function of ϕ/ϕ_0, for four different values of I^{drive}, which correspond to those in Fig. 3.1(c). (c) Neuronal firing frequency as a function of ϕ/ϕ_0, for the same values of I^{drive} as in panel B. Note how linear growth of ϕ/ϕ_0 results in sub-linear growth of the frequency, indicating that the delay depth is largely determined by the speed of the potassium current relative to the spiking frequency of the neuron. (d-f) Effects of modifying the speed of the slow potassium gating variable z in the Type II cortical pyramidal cell model. (d) PRCs of the neuron for three sample values of α_z, with $I^{drive} = 1.20\ \mu A/cm^2$. (e) Absolute value of the delay depth of the PRCs as a function of α_z, for four different values of I^{drive}, which correspond to those in Fig. 3.1(f). (f) Neuronal firing frequency as a function of α_z, for the same values of I^{drive} as in panel E. (g-i) Effects of modifying the speed of the sodium inactivation gating variable h in the cortical pyramidal cell model. (g) PRCs of the neuron for three sample values of α_h, with $I^{drive} = 1.20\ \mu A/cm^2$. (h) Absolute value of the delay depth of the PRCs as a function of α_h, for four different values of I^{drive}, which correspond to those in Fig. 3.1(f). (i) Neuronal firing frequency as a function of α_h, for the same values of I^{drive} as in panel (h).

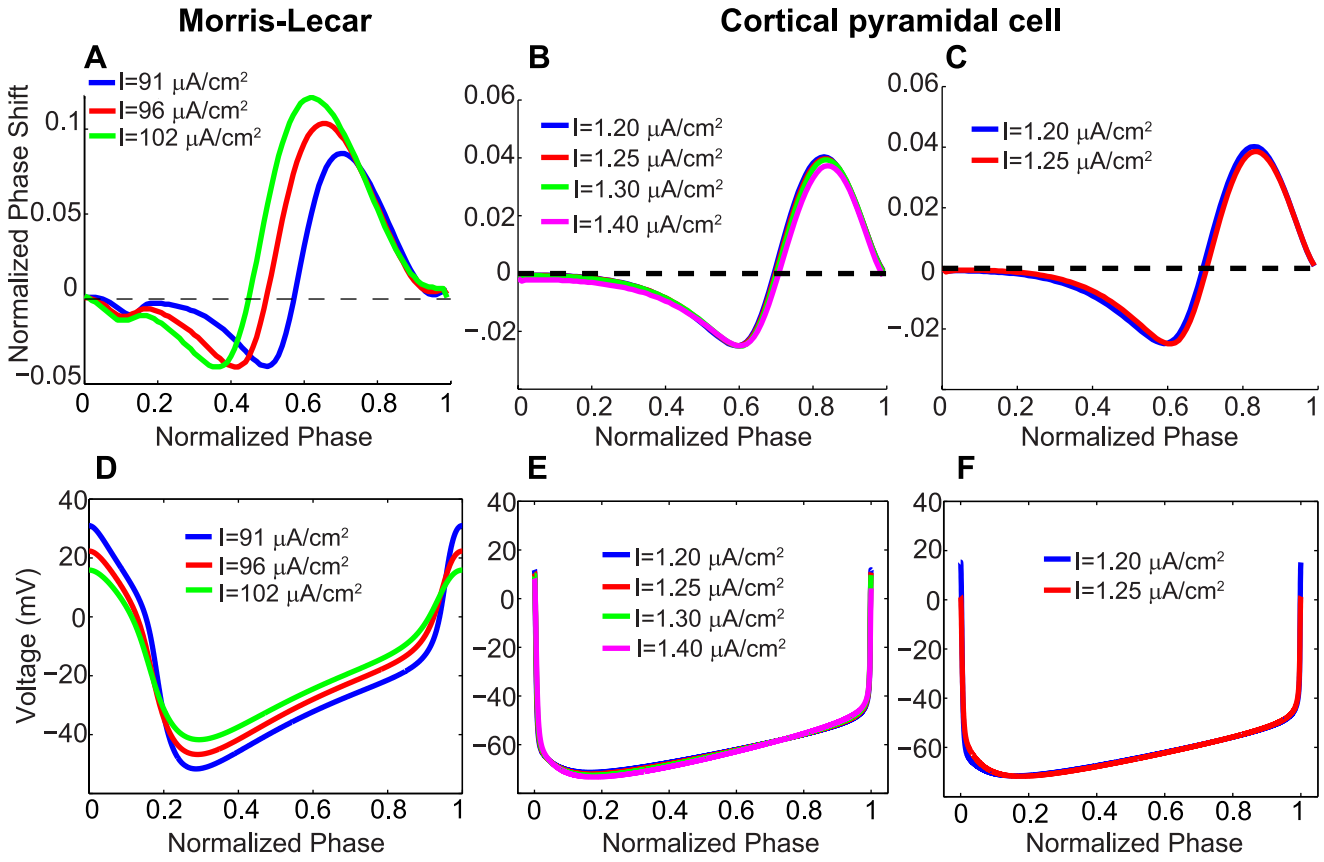

Figure 3.3: (a) PRC profiles of the Type II Morris-Lecar neuron for three different values of I^{drive}, with ϕ separately adjusted to induce a maximum phase delay of 0.04. (b) PRC profiles of the Type II cortical pyramidal neuron for four different values of I^{drive}, with α_z separately adjusted to induce a maximum phase delay of 0.025. (c) PRC profiles of the Type II cortical pyramidal neuron for two different values of I^{drive}, with α_h separately adjusted to induce a maximum phase delay of 0.025. (d) Unperturbed voltage traces as a function of oscillatory phase corresponding to the Type II Morris-Lecar PRCs in panel A. (e) Unperturbed voltage traces as a function of oscillatory phase corresponding to the Type II cortical pyramidal PRCs in panel B. (f) Unperturbed voltage traces as a function of oscillatory phase corresponding to the Type II cortical pyramidal PRCs in panel C. Note how the voltage traces are virtually identical in for the cortical pyramidal model, but not for the Morris-Lecar model. This explains why the PRCs are virtually identical for the cortical pyramidal model, but not the Morris-Lecar model.

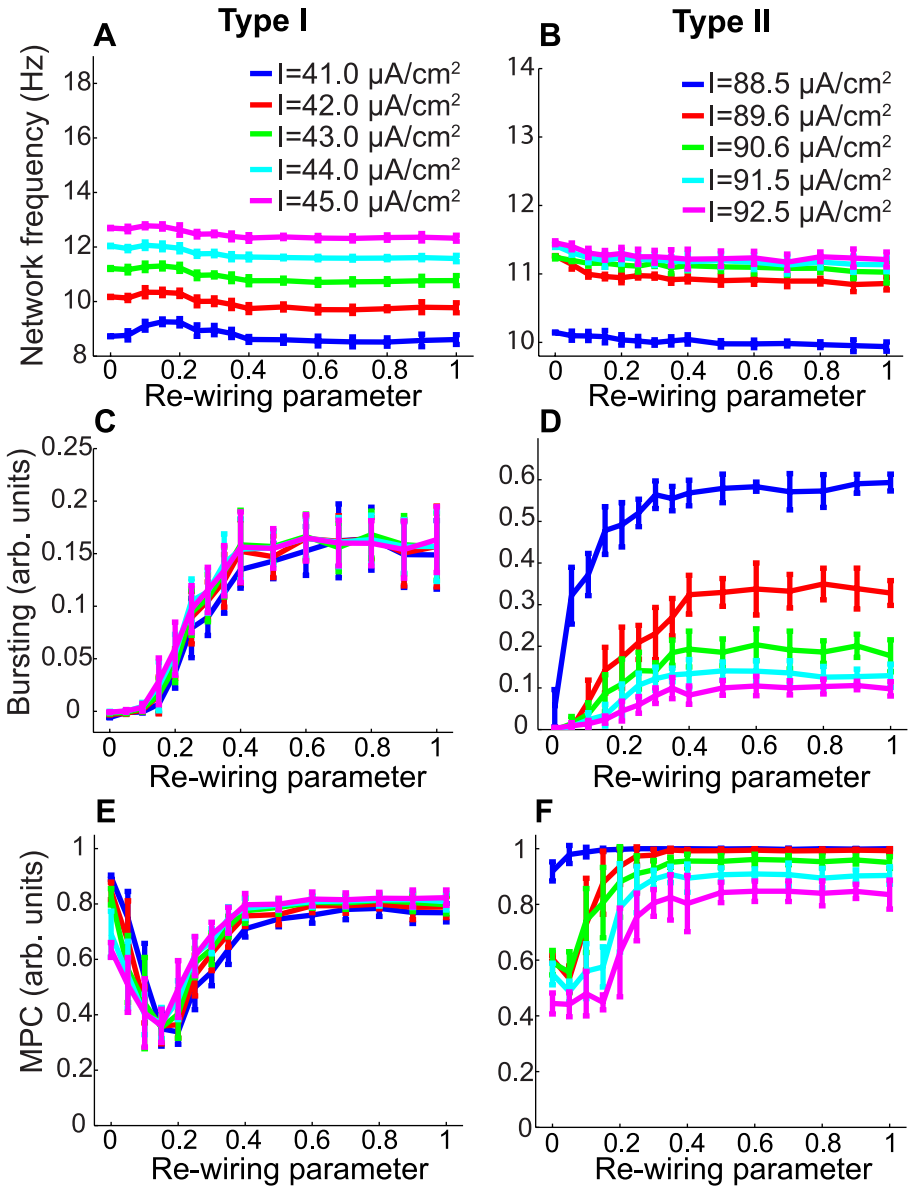

Figure 3.4: Measures of network activity for simulations of large-scale (N=200) excitatory networks of Morris-Lecar model neurons driven with various constant applied currents (different curves) for Type I (a,c,e) and Type II (b,d,f) cells. The synaptic coupling was set to $s = 0.3$ mS/cm^2 for Types I and II. (a,b) Average network firing frequency as a function of the network re-wiring parameter. (c,d) Phase-zero synchronization (as quantified by the bursting measure) versus the re-wiring parameter. (e,f) Phase locking (as measured by mean phase coherence) as a function of the re-wiring parameter.

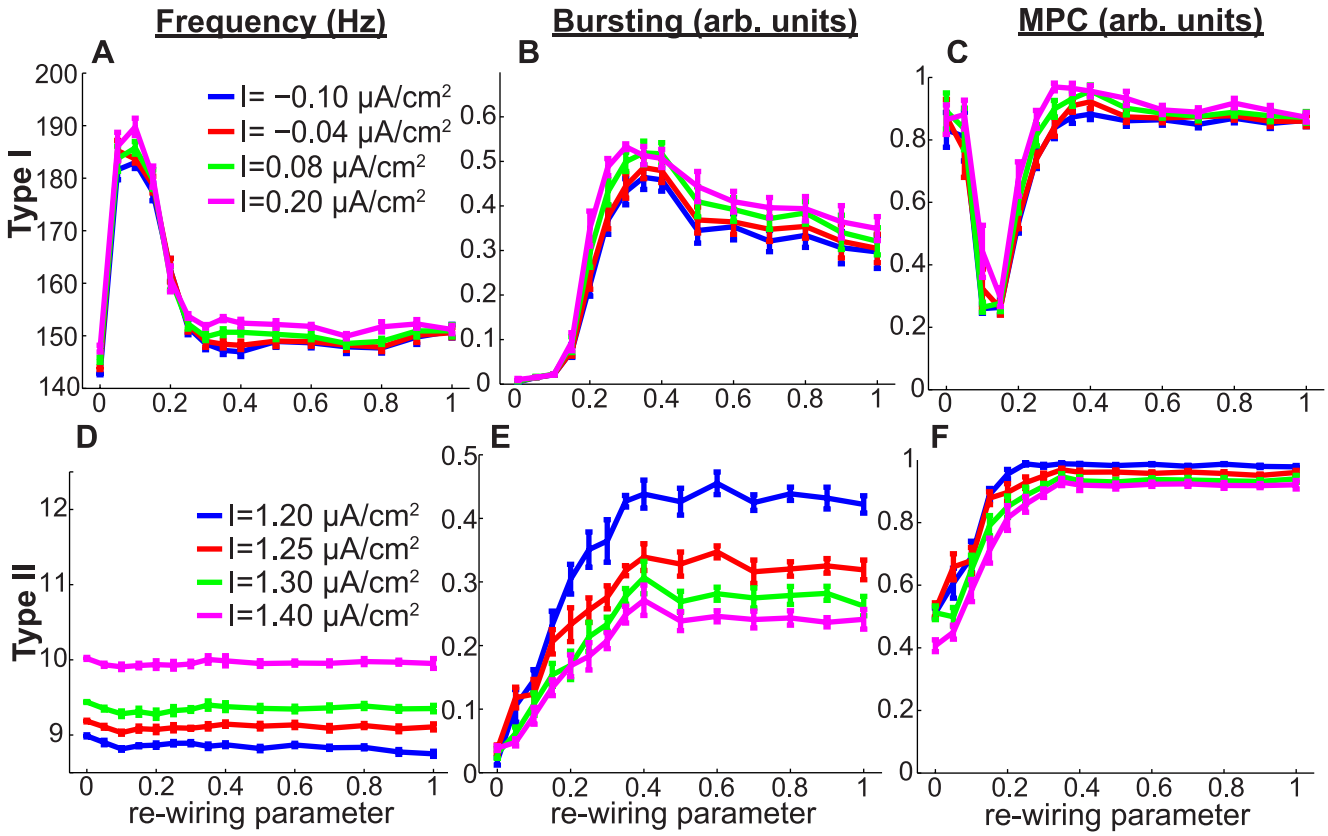

Figure 3.5: (a-f) Measures of network activity for simulations of large-scale (N=200) excitatory networks of cortical pyramidal model neurons driven with varying constant applied currents for Type I (a,b,c) and Type II (d,e,f) cells. Synaptic weight was fixed at $s = 0.35$ mS/cm^2 for Type I plots and $s = 0.035$ mS/cm^2 for Type II plots. (a,d) Average network frequency as a function of the re-wiring parameter for Types I and II networks. (b,e) Phase-zero synchronization, as measured by the bursting parameter, as a function of the re-wiring parameter for Types I and II networks. (c,f) Phase locking, as measured by mean phase coherence, as a function of the re-wiring parameter for Types I and II networks. Note how Type II network synchrony tended to decrease with increasing stimulation intensity, while Type I network synchrony tended to remain the same or slightly increase with increased stimulation intensity.

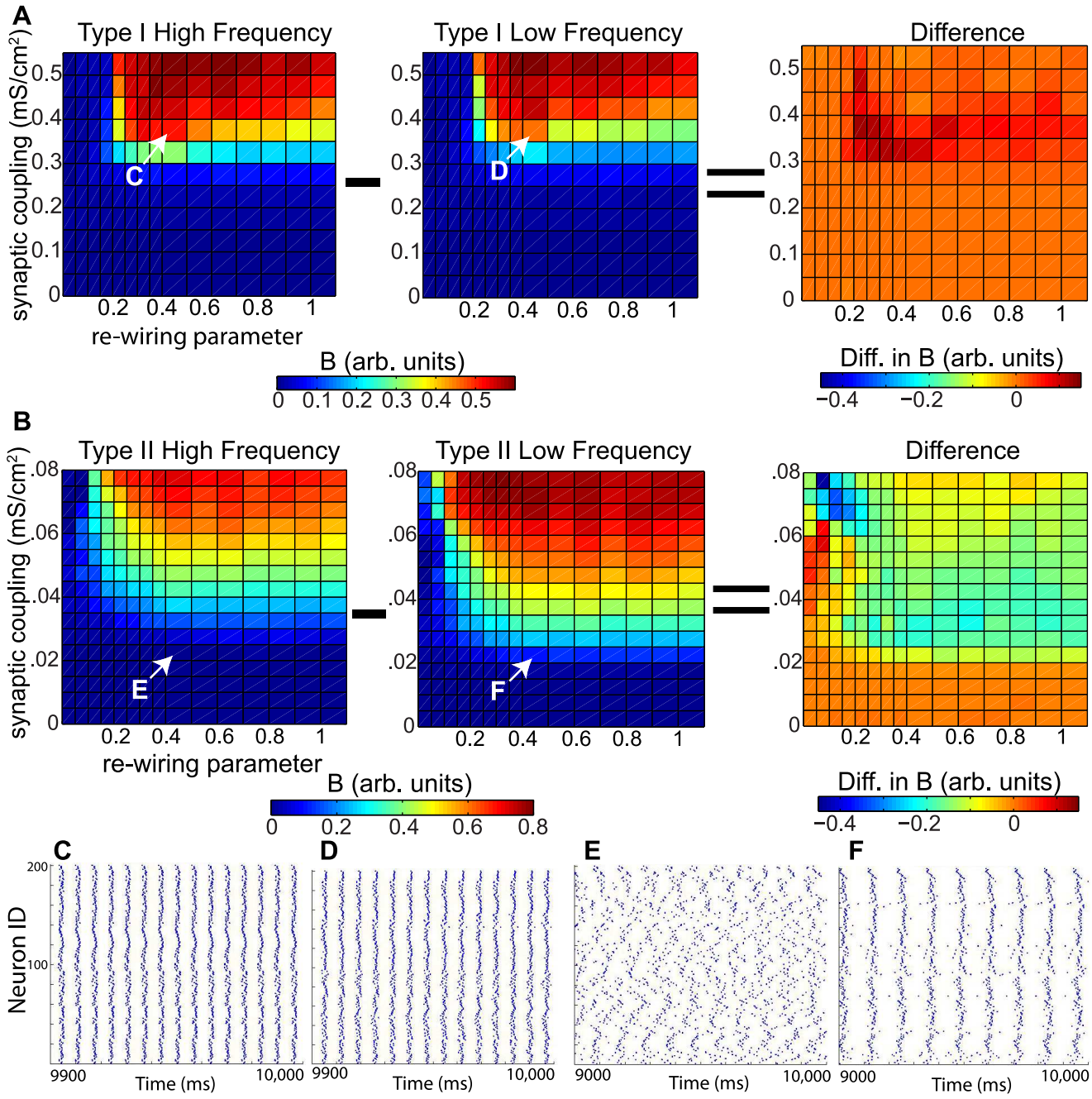

Figure 3.6: (a,b) Phase-zero synchrony (as measured by the bursting parameter, B) of Type I and Type II cortical pyramidal neuronal networks as a function of synaptic coupling strength s and the re-wiring parameter, p. The left panels show values of B for networks stimulated with a high applied current (0.20 μA/cm^2 for Type I and 1.40 μA/cm^2 for Type II), and the middle panels show values of B for networks with a low applied current (-0.10 μA/cm^2 for Type I and 1.20 μA/cm^2 for Type II). The right panel subtracts the low-frequency values of B from the high-frequency values of B. Note the pronounced negative-difference region in the Type II plot, while the Type I plot shows almost exclusively zero or positive values of the difference. (c,d) Raster plots of the last 100 ms of simulations of high-frequency (c) and low-frequency (d) Type I networks with network parameters $s = 0.35$ mS/cm^2 and $p = 0.40$. (e,f) Raster plots of the last 1000 ms of simulation of (e) high-frequency and (f) low-frequency Type II networks with network parameters $s = 0.020$ mS/cm^2 and $p = 0.40$. The difference in synaptic coupling values between Type I and Type II networks was due to the fact that the Type II networks synchronized better than the Type I networks and therefore required much smaller synaptic coupling values to appreciably synchronize.

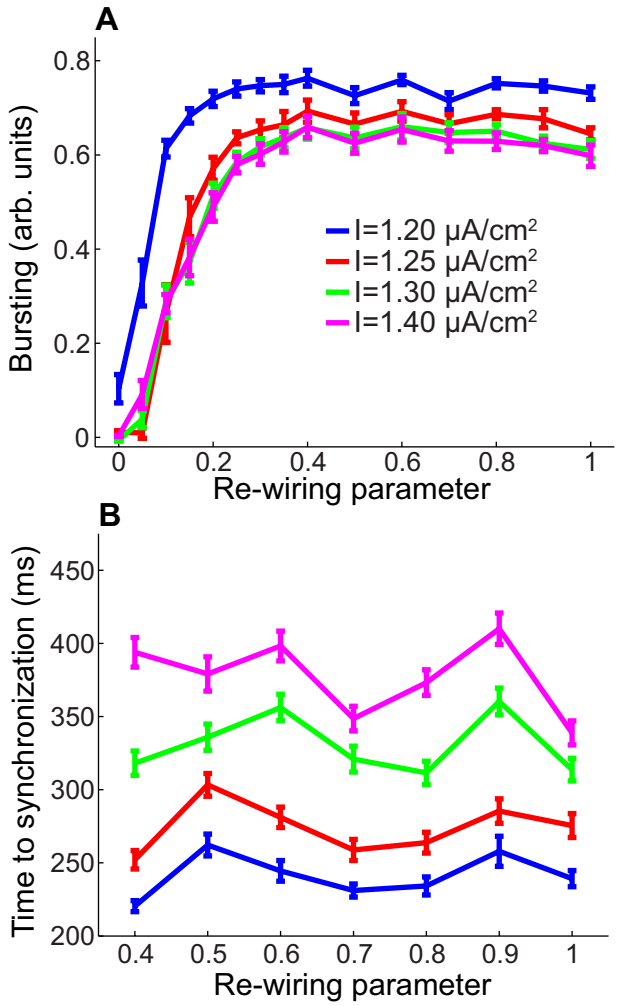

Figure 3.7: (a) Bursting parameter B as a function of the re-wiring parameter for four Type II networks driven with different values of applied current ($s = 0.065$ mS/cm^2). Note how for values of the re-wiring parameter greater than approximately 0.40, there was little difference among the values of B for different values of I^{drive}, especially for the three largest values of I^{drive}. (b) Average time taken for the bursting parameter of Type II networks with randomly-distributed initial conditions to breach 0.6. Initial conditions were randomized such that initial membrane voltage values were uniformly distributed on the interval [-70 mV, -50mV], with gating variables set to corresponding equilibrium values. Each data point is an average of 100 simulations. Note that panel B plots the subset of values of the re-wiring parameter from panel A for which the bursting parameter assumes approximately constant values.

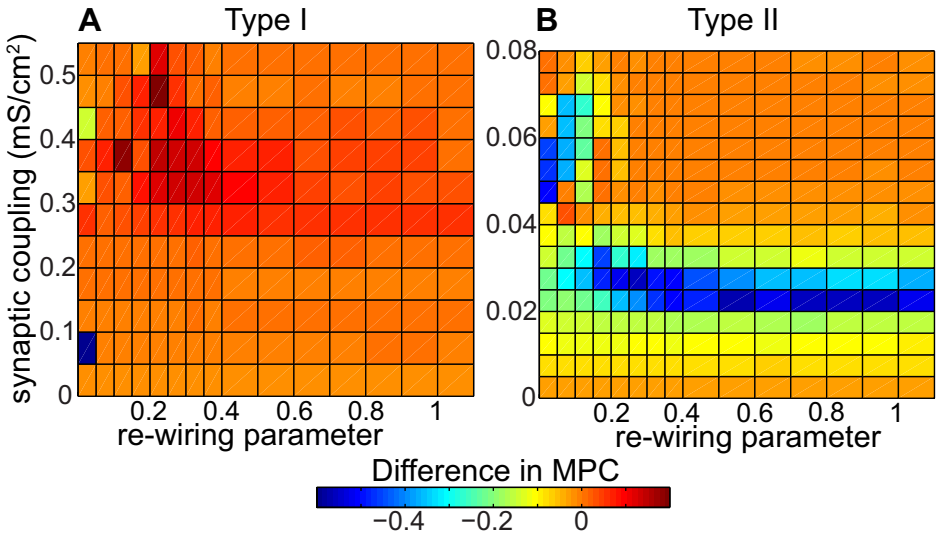

Figure 3.8: (a,b) Differences in MPC between high- and low-frequency networks as a function of network re-wiring and synaptic weight for (a) Type I and (b) Type II networks composed of cortical pyramidal cells. Values of I^{drive} were the same as in Fig. 3.6.

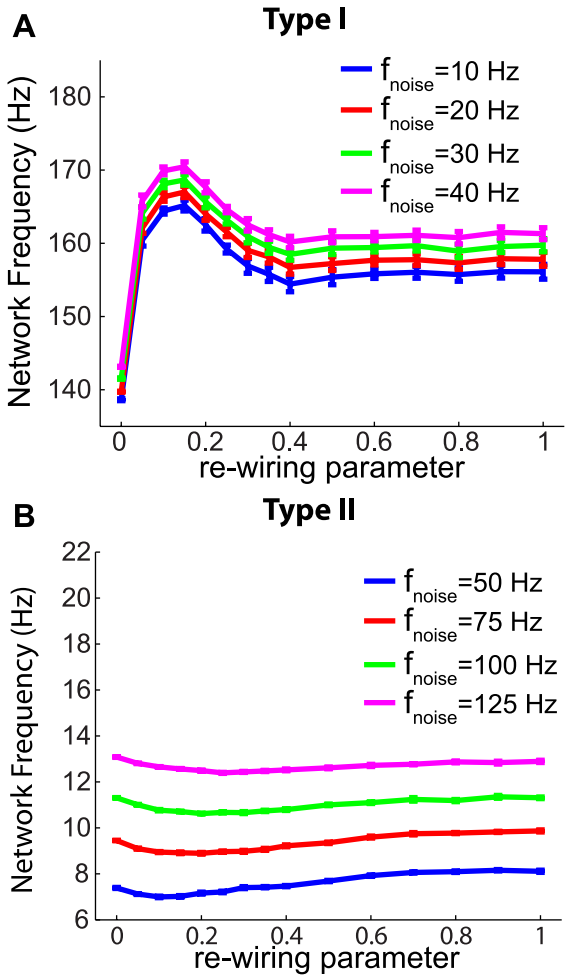

Figure 3.9: (a,b) Average network frequency as a function of the re-wiring parameter for various values of f_{noise} in (a) Type I and (b) Type II stochastic-input networks. Synaptic weight was set to 0.30 mS/cm^2 in (A) and 0.14 mS/cm^2 in (b).

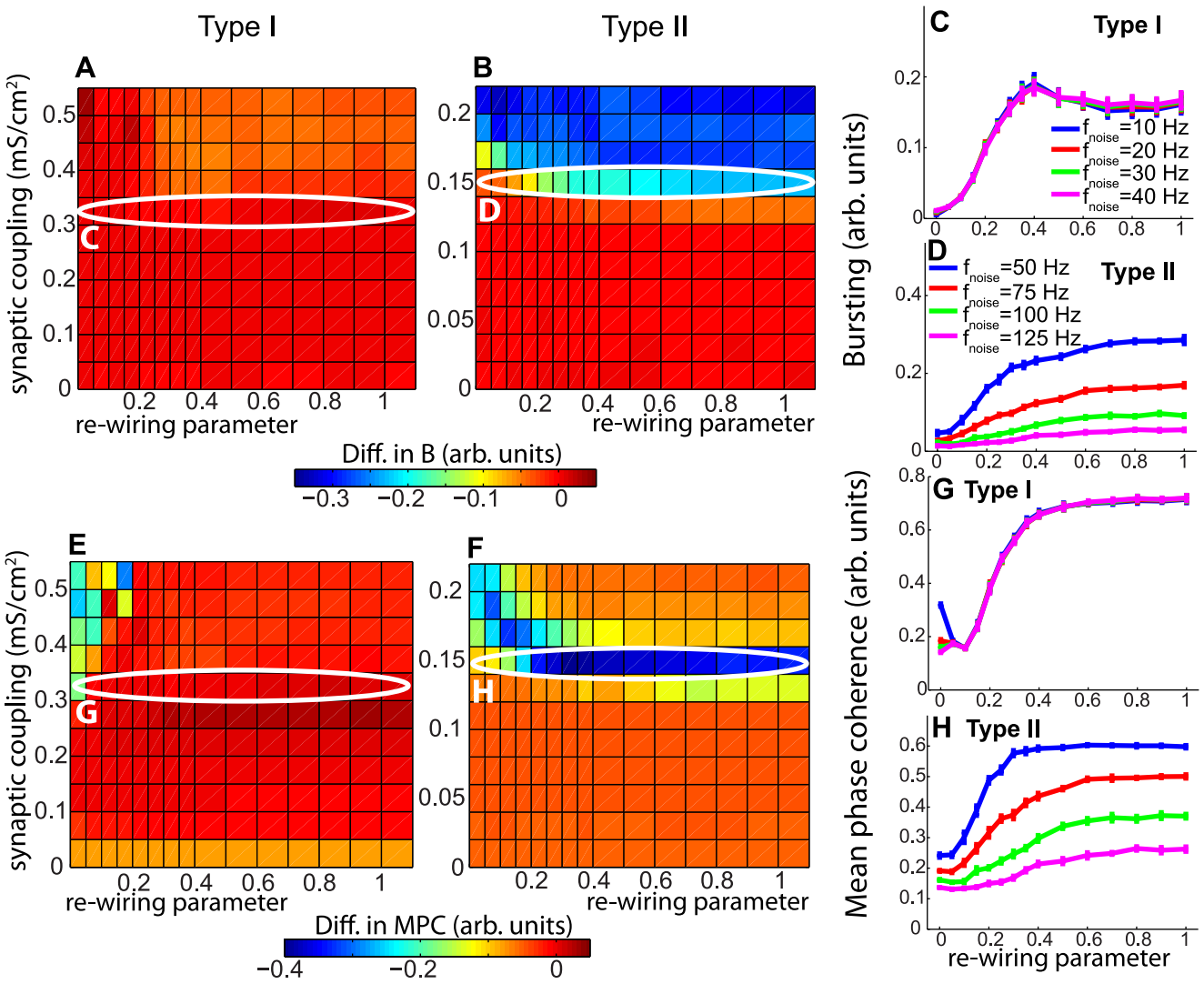

Figure 3.10: (a,b) Differences in bursting parameter B between high- and low-frequency networks as a function of synaptic weight s and the re-wiring parameter for (a) Type I and (b) Type II networks. For Type I networks, $f_{\text{noise}} = 40$ Hz and $f_{\text{noise}} = 10$ Hz corresponded to high- and low-frequency networks, respectively, while for Type II networks, $f_{\text{noise}} = 125$ Hz and $f_{\text{noise}} = 50$ Hz corresponded to high- and low-frequency networks, respectively. (c,d) Values of the bursting parameter as a function of the re-wiring parameter for four different values of f_{noise}, with synaptic coupling fixed at $s = 0.30\text{mS/cm}^2$ in (C) and $s = 0.14\text{mS/cm}^2$ in (D). The circled regions in plots (a) and (b) were constructed by taking the difference between the highest- and lowest-frequency data points in (c) and (d). (e,f) Differences in MPC between high- and low-frequency networks as a function of synaptic weight and the re-wiring parameter for Type I and Type II networks. (g,h) Values of the MPC for four different values of f_{noise}, with synaptic coupling fixed at $s = 0.30$ mS/cm^2 in (g) and $s = 0.14$ mS/cm^2 in (h). The circled regions in plots (e) and (f) were constructed by taking the difference between the highest- and lowest-frequency data points in (g) and (h). Line colors in plots (g) and (h) correspond to the same legend as in plots (c) and (d), respectively.

CHAPTER IV

Acetylcholine, network dynamics, and synaptic renormalization

4.1 Introduction

In the previous chapter we analyzed the dynamics of a cortical pyramidal cell whose phase response curve (PRC) switched from Type II to Type I when modulated with acetylcholine. In this chapter, we explore how such cholinergically-induced PRC switching may be important to understanding sleep. The work presented in this chapter has been submitted for publication in *PLoS Computational Biology*, and it was performed in collaboration with Victoria Booth, Geoffrey Murphy, and Michal Zochowski.

Sleep is crucial for normal cognitive function, as evidenced by the many cognitive impairments associated with chronic sleep loss [126, 127]. A leading proposal for the function of sleep, called the synaptic renormalization hypothesis, posits that sleep is required to maintain synaptic balance in the brain [90]. According to this hypothesis, waking experiences result in the net potentiation of many brain circuits, leading to both increased energy consumption and heightened demand for space by the potentiated synapses. In order to conserve energy and space, sleep induces a period of large-scale synaptic downscaling. Sleep is therefore "the price we pay for plasticity" [95].

Multiple lines of empirical evidence supporting the synaptic renormalization hypothesis have recently emerged[128, 129, 130, 131, 132], including *in vivo* studies finding increased slope of evoked LFP/EEG responses after wakefulness and decreased slope following sleep in rats[91] and humans[92]. Furthermore, increasing evidence supports a link between synaptic depotentiation during sleep and slow wave activity (SWA)[133], which is the pattern of electroencephalograph (EEG) activity observed during NREM sleep in mammals and birds which features increased power in the delta band (0.5 to 4 Hz). Various studies have shown that SWA in NREM sleep locally increases in brain areas that exhibit potentiation during prior wakefulness[94, 134, 135], suggesting that SWA may function to maintain synaptic homeostasis.

Exactly how synaptic downscaling is induced during sleep is an open question. One suggestion is that the repeated alternation of depolarized "up" states, reflecting the simultaneous activity of many neurons, and hyperpolarized "down" states, reflecting fewer active neurons, observed to occur at approximately 1 Hz during SWA may induce long-term depression (LTD) of synapses [136, 137]. Another possibility is that the reduction of brain-derived neurotrophic factor (BDNF) during sleep[95, 128] might enable synaptic depression. Similarly, it is not clear exactly why synapses might exhibit net potentiation during wakefulness, though it has been suggested that the processing of sensory signals or the formation of new memories may inevitably lead to synaptic upscaling[90].

A further hypothesis is that differences in the neuromodulators available during waking and NREM sleep states may contribute to the opposing effects of wakefulness and NREM sleep on neuronal potentiation levels[95]. Waking is characterized by high levels of noradrenaline, serotonin, histamine and acetylcholine in cortex, while

all these neurotransmitters are at low levels during NREM sleep[138, 139]. The low levels of these neuromodulators during sleep has led to the idea that this alters molecular mechanisms underlying spike-timing dependent plasticity (STDP) so that sleep favors synaptic depotentiation[140]. Although some investigation has been done into the effects of various neuromodulators on STDP[141], these mechanisms remain poorly understood.

In the present study, we build upon previous work to develop a new theory for synaptic downregulation during NREM sleep that highlights a role for differing cortical network dynamics during wake and NREM sleep states. This theory relies upon previous findings showing that acetylcholine (ACh) modulates the phase-dependence of neural responses in cortex[142, 143]. When ACh is more available, as in the awake state, most cortical neurons display phase-independent firing in response to synaptic input: they fire soon after receiving excitatory input regardless of their activity when the input arrives (Type I). In contrast, when ACh is less available, as during NREM sleep, cortical neurons display phase-dependent firing in response to synaptic input: whether they fire sooner or later after receiving an excitatory input depends on how long it has been since they last fired (Type II). As we and others have shown previously, the increased flexibility of exact firing times in response to input that occurs in the absence of ACh better enables pre- and post-synaptic cells to synchronize their activity, thereby increasing synchronized activity in cortical networks [102, 35, 36]. While ACh has many diverse effects in the brain[144, 145], here we focus on these dynamical effects of cholinergic modulation.

Our new theory concerns the effect of increased synchronized network activity during NREM sleep on the strength of synaptic connections. In particular, we posit that although this increase in synchronized network activity strengthens some individual

synaptic connections, it weakens others. Further, and critically, this weakening is more pronounced when an animal is experiencing NREM sleep (more synchronized activity) than when an animal is awake (less synchronized activity). Supporting this novel hypothesis, we show that a computational model employing these dynamic, physiologically-plausible mechanisms is fully able to account for synaptic renormalization during NREM sleep.

4.2 Materials and Methods

4.2.1 Cortical neuron model

The cortical pyramidal model neuron we employed was motivated by a recent experimental study which showed that in slices of mouse visual cortex, the presence of acetylcholine (ACh) modulated the response properties of cortical neurons as measured by the phase response curve [142]. The neuronal PRC tracks the changes in spike timing in response to perturbations of the membrane potential as a function of the phase of the spike cycle at which the perturbation occurs. The presence of ACh and its effects upon neuronal PRCs were shown to be well modeled by varying the maximum conductance g_{Ks} of a slow, low-threshold K^+-mediated adaptation current from 1.5 mS/cm^2 to 0 mS/cm^2 in a Hodgkin-Huxley based neuronal model [143, 113]. We used this model in the current study, and modulated only g_{Ks} to model the presence or absence of ACh. The model also featured a fast, inward Na^+ current. The model also includes an inward Na^+ current, a delayed rectifier K^+ current, and a leakage current. The current balance equation for the i^{th} cell was

(4.1)
$$C\frac{dV_i}{dt} = -g_{Na}m_\infty^3(V_i)h(V_i-V_{Na})-g_{Kdr}n^4(V_i-V_K)-g_{Ks}z(V_i-V_K)-g_L(V_i-V_L)+I_i^{\text{drive}}+I_i^{\text{noise}}-I_i^{\text{syn}},$$

with $C = 1.0\ \mu\mathrm{F/cm^2}$, V_i in millivolts, and t in milliseconds. I_i^{drive} was an externally applied current that was constant for each neuron but Gaussian-distributed across neurons in the network, with a variance set to induce a spread of 1 Hz in the instrinsic neuronal frequencies in the neurons comprising both cholinergically-modulated networks and non-cholinergic networks. The mean of the distribution of I_i^{drive} values was $0.08\mu\mathrm{A/cm^2}$ for the ACh networks and $1.30\mu\mathrm{A/cm^2}$ for the non-ACh networks (different values were necessary to account for different firing thresholds and frequency-current curves). I_i^{noise} was a Gaussian noise term supplied to each neuron in our study of noise robustness (Fig. 4.4). This noise was independent from neuron to neuron, but for each individual neuron the noise was correlated over a time scale of 100 ms (the typical inter-spike interval of the slowest-firing neurons). I_i^{syn} was the synaptic current received by neuron i.

Activation of the Na^+ current was instantaneous and governed by the steady-state activation function $m_\infty(V) = \{1 + \exp[(-V - 30.0)/9.5]\}^{-1}$. Dynamics of the Na^+ current inactivation gating variable h were given by

$$dh/dt = (h_\infty(V) - h)/\tau_h(V), \tag{4.2}$$

with $h_\infty(V) = \{1 + \exp[(V + 53.0)/7.0]\}^{-1}$ and $\tau_h(V) = 0.37 + 2.78\{1 + \exp[(V + 40.5)/6.0]\}^{-1}$. The delayed rectifier K^+ current was gated by n, whose dynamics were governed by

$$dn/dt = (n_\infty(V) - n)/\tau_n(V), \tag{4.3}$$

with $n_\infty(V) = \{1 + \exp[(-V - 30.0)/10.0]\}^{-1}$ and $\tau_n(V) = 0.37 + 1.85\{1 + \exp[(V + 27.0)/15.0]\}^{-1}$. The slow, low-threshold K^+ current targeted by cholinergic

modulation was gated by z, which varied in time according to

$$dz/dt = (z_\infty(V) - z)/75.0, \tag{4.4}$$

where $z_\infty(V) = \{1 + \exp[(-V - 39.0)/5.0]\}^{-1}$.

The slow, low-threshold K^+ current loosely modeled the muscarine-sensitive M-current observed in cortical neurons. Setting $g_{Ks} = 0$ modeled the presence of ACh in cortical networks, and setting $g_{Ks} = 1.5$ modeled the absence of ACh from cortical networks. All other parameter values were the same for both cholinergic and non-cholinergic networks: $g_{Na} = 24.0$ mS/cm^2, $g_{Kdr} = 3.0$ mS/cm^2, $g_L = 0.02$ mS/cm^2, $V_{Na} = 55.0$ mV, $V_K = -90.0$ mV, and $V_L = -60.0$ mV.

4.2.2 PRC Calculation

To obtain the phase response curves displayed in Fig. 4.1, I^{drive} was set to a fixed value to elicit repetitive firing in a single, synaptically isolated neuron, and the model equations were time evolved using a fourth-order Runge-Kutta numerical scheme until the oscillatory period stabilized. Then, using initial conditions associated with the spike peak, brief current pulses were administered at different phases of the oscillation, and the perturbed periods were used to calculate the corresponding phase shifts. The current pulses were administered at 100 equally-spaced time points throughout the period of the neuronal oscillation. The current pulses had a duration of 0.06 ms and an amplitude of 3.0 μA/cm^2 for the cholinergically-modulated cortical pyramidal neuron, a duration of 0.06 ms and an amplitude of 10.0 μA/cm^2 for the non-cholingically-modulated cortical pyramidal neuron.

4.2.3 Network simulations

We simulated networks with 800 excitatory neurons and 200 inhibitory neurons. The network connectivity pattern was constructed using the Watts-Strogatz architecture for "small world networks" [146]. Starting with a 1-D ring network with periodic boundary conditions, each neuron was at first directionally coupled to its $2r$ nearest neighbors, and then every connection in the network was rewired with probability p to another neuron selected at random. In this way, $p = 0$ resulted in a locally-connected network and $p = 1$ in a randomly connected network. The radius of connectivity r therefore determined the density of connections in the network, while the re-wiring parameter p determined the network connectivity structure. Network connectivity r was set to 4 in all simulations except those in Fig. 4.9 and Fig. 4.5.

Synaptic current was transmitted from neuron $\jmath$ following times $t_{\jmath_k}$ when its membrane voltage breached -20 mV. The synaptic current delivered from neuron $\jmath$ to a synaptically connected neuron $\imath$ at times $t >= t_{\jmath_k}$ was given by $I_{\imath\jmath}^{\text{syn}} = w_{\imath\jmath} \exp\left(-\frac{t-t_{\jmath_k}}{\tau}\right)(V_\imath - E_{\text{syn}})$, where we used $\tau = 0.5$ ms and $E_{\text{syn}} = 0$ mV for excitatory synapses and $E_{\text{syn}} = -75$ mV for inhibitory synapses. The total synaptic current to a neuron $\imath$ was given by $I_\imath^{\text{syn}} = \sum_{\jmath\in\Gamma_\imath} I_{\imath\jmath}^{\text{syn}}$, where $\Gamma_\imath$ was the set of all neurons presynaptic to neuron $\imath$. Excitatory synaptic strengths $w_{\imath\jmath}$ evolved according to an additive STDP rule in which the change in synaptic strength between postsynaptic neuron $\imath$ and presynaptic neuron $\jmath$ was given by

$$\Delta w_{\imath\jmath} = \begin{cases} e^{-|\Delta t|/\tau_{\text{stdp}}}, & \text{if } \Delta t > 0 \\ -e^{-|\Delta t|/\tau_{\text{stdp}}} & \text{if } \Delta t < 0 \end{cases}, \tag{4.5}$$

where Δt represents the spike time of postsynaptic neuron $\imath$ minus the spike time

of presynaptic neuron $\jmath$. We set $\tau_{\text{stdp}} = 10.0$ ms in all our simulations, except in Fig. 4.6, where we show that our results are robust to large variations in the size of this window. We also confined synaptic strength values to the interval $[0, w_{max}]$, where w_{max} was a parameter that we varied in our simulations. The maximum amount the strength of a synapse could change due to one spike pairing was $w_{max}/10$. We intentionally chose this value to be rather large so that synaptic strength distributions would equilibrate in a reasonable amount of time.

Simulations were initialized with all synaptic strengths set to $w_{max}/2$, after which the strengths of excitatory synapses evolved freely according to the dynamics of the network (strengths of inhibitory synapses were fixed). After the distribution of synaptic weights had equilibrated (which required longer for non-cholinergic networks because they fired at lower rates than cholinergic networks; cholinergic network simulations were run for 5,000 ms and non-cholinergic network simulations were run for 20,000 ms), the overall network potentiation was quantified using using the equation

$$\text{Network potentiation} = 2\frac{< w >}{w_{max}} - 1, \tag{4.6}$$

where $< w >$ designates the mean of all final excitatory synaptic strengths. This measure attributed a network potentiation value of +1 to maximally potentiated final synaptic distributions, and a network potentiation value of -1 to maximally *de*potentiated final synaptic distributions. All simulations were numerically integrated in Matlab using a fourth-order Runge-Kutta method with a time step of 0.05 ms.

We quantified phase-synchronization of neuronal firing in our simulations using the mean phase coherence (MPC) measure [101]. This measure quantified the degree of phase locking between neurons, assuming a value of 0 for completely asynchronous

spiking and 1 for complete phase locking. Note that high MPC could be attained for locking of phases at *any value*, not just zero. The MPC between a pair of neurons, $\sigma_{1,2}$, was defined by:

$$\sigma_{1,2} = \left| \frac{1}{N} \sum_{k=1}^{N} e^{i\phi_k} \right| \tag{4.7}$$

$$\phi_k = 2\pi \left(\frac{t_{2,k} - t_{1,k}}{t_{1,k+1} - t_{1,k}} \right), \tag{4.8}$$

where $t_{2,k}$ was the time of the k^{th} spike of neuron 2, $t_{1,k}$ was the time of the spike of neuron 1 that was largest while being less than $t_{2,k}$, $t_{1,k+1}$ was the time of the spike of neuron 1 that was smallest while being greater than or equal to $t_{2,k}$, and N was the number of spikes of neuron 2. The MPC of the entire network was calculated by averaging the mean phase coherence of all neuron pairs, discounting the first half of network activity, in order to capture steady-state network synchronization.

In our simulations exploring network heterogeneity, the network was composed of 1000 neurons (800 excitatory, 200 inhibitory), of which 50 comprised a cluster in which w_{max} was two times greater than in the rest of the network (w_{max} = 0.08 mS/cm^2 for connections originating from neurons within the cluster, and w_{max} = 0.04 mS/cm^2 for connections originating from neurons outside the cluster). Connectivity was constructed by initially segragating the cluster from the rest of the network, so that the cluster and the rest of the network formed two disjoint Watts-Strogatz networks, each with a radius of connectivity of 4 and a re-wiring probability of 0.60. The two networks were then coupled by sending three outgoing connections from each cluster neuron to randomly-selected neurons in the rest of the network. Similarly, three outgoing connections were also sent from each neuron in the rest of the network to randomly-selected neurons within the cluster. Simulations were then run in

which the network was repeatedly switched between cholinergic and non-cholinergic states, and the effects on network potentiation were explored. We quantified the network potentiation for all excitatory connections, as before, but also for just the connections which linked the cluster and the rest of the network.

4.3 Results

We simulated the effects of ACh on synaptic potentiation in cortical networks consisting of 1000 neurons (20% of which were inhibitory). Each neuron was described by a recently-developed cortical pyramidal cell model [143] that was motivated by experimentally measured effects of ACh [142]. In this model, simulated cholinergic modulation blocks a slow, low-threshold M-type potassium current that induces spike frequency adaptation. Blockade of this current modulates the response properties of modeled neurons as measured by the phase response curve (PRC). In the absence of ACh, the neuronal PRC displays phase regions where spike timing is delayed and where it is advanced, categorized as Type II PRC [35, 36]. In the presence of ACh, only advances in spike timing are obtained regardless of the phase of perturbation, resulting in Type I PRC (see Fig. 4.1).

Switching PRCs of synaptically coupled neurons from Type II to Type I has been shown to dramatically affect the synchronization of neuronal networks. Specifically, simulated large-scale neuronal networks whose cells have Type II PRCs have been shown to synchronize much better than neuronal networks composed of cells with Type I PRCs [46]. This effect can be explained heuristically by the fact that neurons with Type II PRC are in some sense "more flexible" than those with Type I PRC, since neurons with Type II PRC can advance *and* delay their spike firing in response to synaptic input [35, 36]. Accordingly, it has been shown that cholinergic modula-

tion has a dramatic effect upon the synchronization of simulated cortical networks, with the absence of ACh (inducing Type II PRC) leading to much higher network synchrony than the presence of ACh (inducing Type I PRC) [102].

We investigated how the differential effects of ACh on network synchrony influenced overall network synaptic potentiation when synaptic strengths evolved according to a spike-timing dependent plasticity (STDP) rule. In our network simulations, synaptic strength values were initialized to an intermediate value and then allowed to evolve, according to the STDP rule, over the interval $[0, w_{max}]$ (see Materials and Methods for simulation details). We quantified the steady state distribution of synaptic strength values with a measure of "network potentiation," calculated as a linear transformation of the mean of the equilibrium distribution. The values of this network potentiation measure range from -1 for maximally weakened networks (all synaptic strength values go to 0) to +1 for maximally strengthened networks (all synaptic strength values go to w_{max}). We investigated the effects of network connectivity by varying synaptic connection architecture using the Watts-Strogatz small-world paradigm [146]. With this method, each neuron was initially connected to a fixed number of its nearest neighbors, and then a certain proportion of these connections were re-wired to synapse onto randomly-selected cells in the network. The proportion of connections which were re-wired was specified by the *re-wiring probability*. Since both maximum synaptic strength and network connectivity structure are known to dramatically influence neuronal network dynamics, we explored a wide range of values for w_{max} and the re-wiring probability to ensure the robustness of our results.

Dynamical effects of acetylcholine on network synchronization and potentiation

Simulated cholinergic modulation switched neuronal PRCs from Type II to Type I (Fig. 4.1 a,b), inducing a decrease in network synchronization (Fig. 4.1 c,d) that affected the steady state distributions of synaptic strengths (Fig. 4.1 e,f). The synaptic strength distribution of the cholinergically-modulated network was heavily skewed toward maximal synaptic weight, reflecting higher network potentiation. On the other hand, the distribution of the non-cholinergic network was more symmetric, with about half the synapses at the maximal value and the majority of remaining synapses at zero strength. These results were robust to variations in maximal synaptic strength and network connectivity architecture (Fig. 4.2 a,b). Network potentiation values for cholinergic networks exceeded those for non-cholinergic networks for almost all combinations of re-wiring probability and w_{max}.

Differences in network potentiation were especially pronounced for $w_{max} \gtrsim 0.05$ mS/cm^2, at which values the network potentiation dropped to approximately zero in non-cholinergic networks for all values of the re-wiring probability (Fig. 4.2b). Interestingly, this drop in network potentiation coincided with the transition from asynchronous to synchronous activity in non-cholinergic networks (Fig. 4.2d). On the other hand, the robustly high levels of potentiation observed in cholinergic networks (Fig. 4.2a) corresponded to completely asynchronous activity for all network parameters (Fig. 4.2c). Our simulations therefore counterintuitively showed that synchronous network dynamics led to relatively lower network potentiation than asynchronous network dynamics.

Since STDP requires correlated firing to potentiate the connection between two neu-

rons, one might expect that asynchronous network activity should induce no net change in network potentiation, rather than the overall increased potentiation we observed. Further analysis of pre- and post-synaptic cell pairs uncovered an important statistical structure of the neuronal firing patterns in the cholinergically-modulated networks: post-synaptic neurons throughout the network were more likely to fire shortly after their pre-synaptic neurons rather than shortly before (Fig. 4.3a). Thus, pre-post spike time differences landed in the positive portion of the STDP curve more frequently than in the negative portion of the STDP curve, resulting in increased potentiation of the network as a whole.

On the other hand, the relatively lower network potentiation observed in networks without cholinergic modulation was due to post-synaptic neurons firing right before their pre-synaptic partners much more frequently (Fig. 4.3b). This effect occurred because the bursts of activity in non-cholinergic networks constrained all neurons to fire within very short time windows, forcing pre-synaptic neurons to directly compete with one another to induce common post-synaptic partners to fire. As a result, roughly half the pre-post spike time differences fell in the positive portion of the STDP curve, and the other half fell in the negative portion, leading to nearly symmetric and highly polarized final distributions of synaptic strengths (as in Fig. 4.1f).

It should be noted that we tested this result for robustness against noise by adding Gaussian-distributed noise with a temporal correlation of 100 ms (the approximate inter-spike interval of the slowest-firing neurons) to the external constant current driving individual neurons. We found that even for a noise amplitude as high as 0.10 μA/cm^2, we still observed much greater potentiation in networks with cholinergic modulation than in non-cholinergic networks for a large range of network param-

eters (Fig. 4.4a,b). This noise amplitude was large relative to the driving currents for both ACh networks (0.08 μA/cm^2) and non-ACh networks (1.30 μA/cm^2). Furthermore, we found that if we chose one set of network parameters and progressively increased the noise amplitude, the difference between network potentiation in the presence and absence of ACh did not disappear until the noise amplitude reached 0.20 μA/cm^2 (Fig. 4.4c).

We also tested our results for robustness to connectivity density by increasing the radius of connectivity in our network simulations (see the description of the Watts-Strogatz small world network paradigm detailed in Materials and Methods). Networks with cholinergic modulation showed greater overall potentiation than non-cholinergic networks for a wide range of connectivity densities (0.8 % to 4.0 % connectivity), though sparser connectivity led to greater differences in network potentiation (Fig. 4.5).

We tested the results for robustness to frequency modulation by varying the duration of the STDP window, τ_{stdp}. We used this approach rather than directly modulating neuronal frequency because network effects made it difficult to elicit a wide range of average firing frequencies. In Fig. 4.6, τ_{stdp} was varied from 1 ms to 100 ms (the default value throughout this study was 10 ms). Cholinergically-modulated networks exhibited much higher network potentiation than non-cholinergically-modulated networks for all values of τ_{stdp}.

Finally, several studies have shown that the equilibrium distribution of synaptic weights in a network subject to STDP strongly depends upon the mathematical form of the STDP rule. Some have suggested that the integral of the LTD portion

of the STDP curve should be greater than the LTP portion of the curve in order to maintain network potentiation at reasonable levels [**?**, **?**], while others have pointed out that "multiplicative" (weight-dependent) STDP rules tend to produce qualitatively different synaptic weight distributions than "additive" STDP rules [**?**]. We explored the first suggestion by using an asymmetric STDP rule in which the integral of the LTD curve was ten percent greater than the integral of the LTP curve. The results of these simulations, shown in Fig. 4.7, are qualitatively similar to our main results in Fig. 4.2. We also implemented a weight-dependent STDP rule, which resulted in more unimodal synaptic weight distributions but still resulted in cholinergic networks showing higher network potentiation than non-cholinergic networks (Fig. 4.8).

Switching acetylcholine levels in a heterogeneous network

The above results pertained to networks with homogeneous connectivity distributions in the sense that all synapses could achieve the same maximal strength, and long-range network connections did not preferentially target any particular neurons. Such homogeneity certainly does not exist in the brain [147, 148]. Therefore, we explored effects of cholinergic modulation on synaptic potentiation in the presence of network connectivity heterogeneities. A question of particular interest was whether ACh-induced changes in synaptic plasticity affect all connections in the network to the same extent. To address this question, we considered a network of 1000 neurons with an embedded cluster of 50 neurons. The maximal synaptic strength values (w_{max}) of connections originating from cells within the cluster were two times greater than for the surrounding network. Additionally, while the number of outgoing connections per neuron was the same for both the cluster and the rest of the network, a fixed fraction of out-going synaptic connections from surrounding cells preferentially

targeted the cluster and vice versa. Thus, in the network, a small number of connections originated within the cluster and projected outside the cluster, while a larger number of connections originated outside the cluster and projected to the cluster (see Materials and Methods for more details).

In this heterogeneous network, we alternately switched between the presence and absence of cholinergic modulation (simulating waking and NREM sleep, respectively), and found that such switching induced immediate and dramatic changes in network synchrony and potentiation (Fig. 4.9a). As in the homogeneous networks, we found that the asynchronous dynamics induced by cholinergic modulation resulted in relatively high network potentiation (Fig. 4.9b,c), but we found that the depotentiating effects of removing acetylcholine were even more pronounced than in homogeneous networks. Fig. 4.9a shows that the network potentiation measure actually dipped below zero for two non-cholinergic intervals, implying that the number of connections whose synaptic strength went to 0 exceeded the number that reached w_{max} (Fig. 4.9d).

This enhanced depotentiating effect resulted from the dynamical interplay between the cluster and the rest of the network. As shown in Fig. 4.9e, in the absence of cholinergic modulation the cluster tended to fire in synchronized bursts, which drove the rest of the network to respond by firing noisy bursts. The relative firing times of the surrounding network relative to the cluster resulted in potentiation of connections originating in the cluster and projecting outside the cluster, and depotentiation of connections originating outside the cluster and projecting to the cluster (see the "no ACh" intervals in Fig. 4.9f). Since there were more connections originating outside the cluster and projecting into the cluster than vice versa, strong overall network

de-potentiation occurred.

Fig. 4.9f demonstrates another striking feature of this network: the small subset of connections projecting from the cluster to the surrounding network remains at very high potentiation levels throughout cholinergic switching. Furthermore, this set of connections collectively *increases* in strength during epochs when ACh is absent, in contrast to the collective weakening exhibited by connections in the rest of the network.

4.4 Discussion and summary

We have proposed a novel physiologically-plausible mechanism, based on cholinergic modulation of neural membrane excitability, that can account for synaptic renormalization during NREM sleep. We have shown that the dramatic changes in membrane excitability induced by cholinergic modulation, and the resulting changes in network firing patterns, lead to upscaling and downscaling of mean synaptic efficacy. Thus, our results propose a dynamical mechanism for synaptic renormalization that provides a bottom-up framework linking changes in the neuromodulator environment during waking and NREM sleep to changes in neuronal excitability, network activity patterns, and overall renormalization of network connectivity. Simulations of networks with heterogeneous synaptic connection distributions also provided evidence for selective rescaling of particular network connections.

Our simulations showed that the presence of ACh in cortical networks led to asynchronous dynamics, which in turn led to relatively high network potentiation. On the other hand, the absence of ACh resulted in more synchronous network activity and relatively lower overall potentiation. These results are consistent with the prediction

of the synaptic renormalization hypothesis that wakefulness (during which ACh is present in cortex) is associated with global synaptic upscaling, while NREM sleep (during which ACh is largely absent from cortex) is associated with global synaptic downscaling. These results were also robust to noise, changes in network frequency, different network topologies, and varoius STDP parameters, and they were strengthened by network heterogeneities.

The general effects of ACh upon the dynamics of our simulated networks also match several empirical observations. The presence of ACh during wakefulness is associated with an asynchronous EEG [149] and greater power in high frequency bands [142, 150]. These effects are replicated in our simulations through the asynchronous network activity (see Fig. 4.1c) and the elevated frequency of neuronal firing observed when cortical networks were cholinergically modulated (compare Fig. 4.1c to Fig. 4.1d). On the other hand, ACh is known to be largely absent during NREM sleep, when slow wave activity dominates EEG recordings. Such activity is associated with the slow oscillation of thalamocortical neuron membrane potential that results from thalamocortical bistability [151, 152, 153]. In addition, multiple lines of evidence suggest that slow waves involve the persistent synchronous bursting of cortical neuron populations [95, 154, 155, 156]. Similar activity patterns were produced in our simulations when ACh was absent from the cortical networks (see Fig. 4.1d), suggesting that the absence of ACh may work in tandem with underlying slow oscillations to facilitate bursting activity. Such bursting activity may have been further promoted by the presence of inhibition within the network, since inhibitory feedback has been shown to promote synchronous neuronal activity [41]. As shown in Fig. 4.9, the highly synchronous activity associated with down-regulated ACh

resulted in synaptic downscaling relative to the asynchronous activity induced by the up-regulation of ACh.

Fig. 4.9f also shows how a subset of connections that were highly potentiated following waking (ACh present) remained strong–and were actually even further strengthened–during simulated NREM sleep (ACh absent). This effect was obtained through the introduction of a small subset of connections which had larger maximum synaptic strength values than in the rest of the network, providing a possible mechanism for sleep-dependent memory consolidation within the framework of spike-timing dependent plasticity. It is known that acetylcholine is essential to proper memory function, as evidenced by the decrease in acetylcholine observed in dementia and the effectiveness of acetylcholinesterase inhibitors such as donepezil in treating dementia [157]. Our results are consistent with a role for acetylcholine in which its presence is necessary for the formation of new memories, while its absence is required for memory consolidation.

While our theory focuses on possible dynamical underpinnings of the renormalization hypothesis, there are many other factors which may contribute to synaptic renormalization. Incoming sensory signals may promote upscaling during wakefulness [90], while downscaling during sleep might be facilitated by the endogenous low-frequency rhythms of slow-wave sleep, which share similar frequency content with the low-frequency stimulation known to induce long-term depression [136, 137]. One recent study suggested that elevated levels of neuromodulators such as noradrenaline and acetylcholine during waking may promote overall synaptic potentiation, while the absence of these same neuromodulators during sleep may modify spike-timing dependent plasticity to favor synaptic depression [140, 141].

Our theory hinges on the result that synchronous network activity leads to synaptic downscaling, while asynchronous network activity generates synaptic upscaling. Our analysis of the structure of spike times in pre- and post-synaptic cell pairs indicates that downscaling was due to timing competition between arriving excitatory post-synaptic potentials (EPSPs) within the brief period of synchronous spiking activity. This competition within such a short time window resulted in about half the pre-post pairings falling in the negative portion of the STDP curve and therefore leading to lower network potentiation relative to asynchronous network activity. It has previously been shown that asynchronous neuronal activity leads to increased network potentiation while synchronous activity leads to decreased network potentiation in simulated networks incorporating STDP with propagation delays [158]. Our results show that similar effects can be obtained in networks where synaptic delays are negligible. Additionally, these effects are obtained for completely different and counterintuitive reasons, namely through altered statistics of spike arrival times at post-synaptic cells.

In summary, we have shown that cholinergic modulation can lead to changes in overall network potentiation, and that these changes may be understood in terms of the altered cellular and network dynamics induced by ACh. Further experimental investigation into the possible role of cholinergic modulation in the dynamical underpinnings of synaptic renormalization is clearly required.

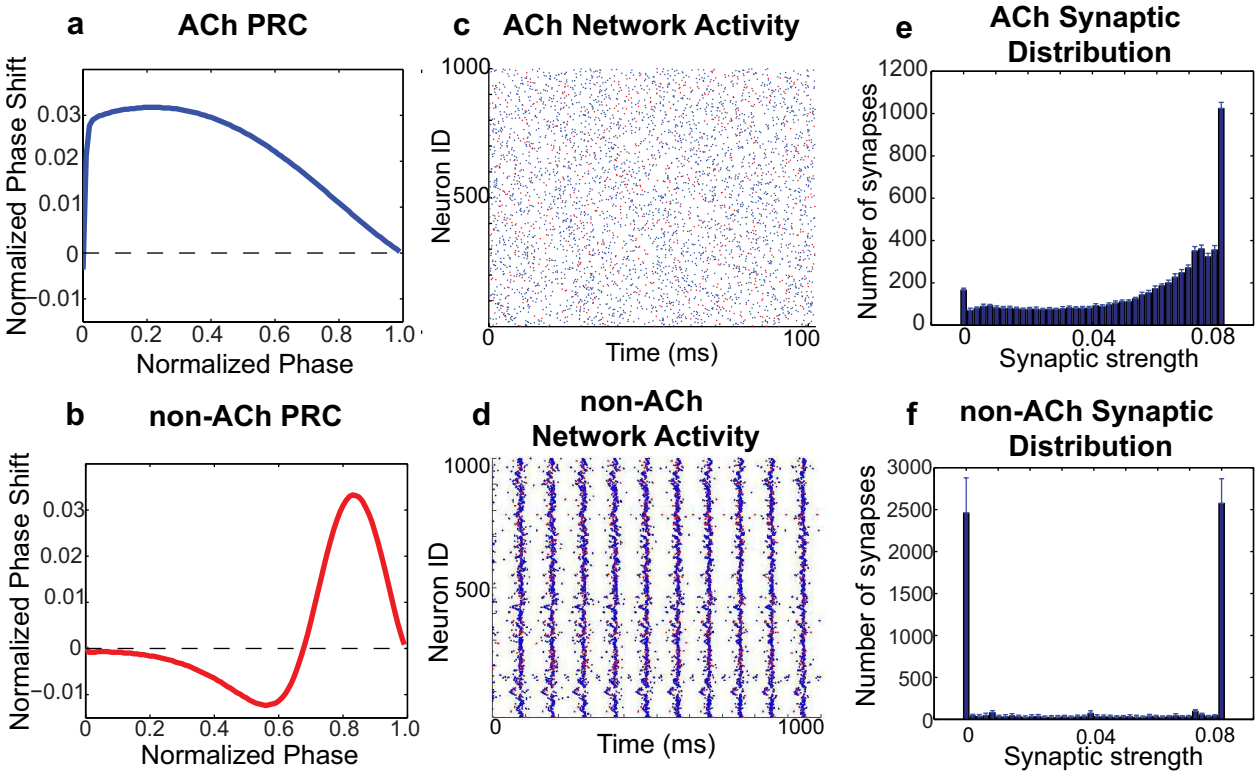

Figure 4.1: Effects of acetylcholine on phase response curves, network synchrony, and overall network synaptic potentiation in 1000-cell cortical neuronal network models. (a,b) Phase response curves of individual neurons with (a) and without (b) simulated cholinergic modulation. (c, d) Raster plots of the activity of a model cortical network with (c) and without (d) simulated ACh. Blue (Red) dots represent spikes of excitatory (inhibitory) neurons. Note the higher synchronization in the network without cholinergic modulation compared to the network with cholinergic modulation. (e) Average final distributions of synaptic strengths for a typical cholinergically-modulated network, with a network potentiation value of ≈ 0.35. (f) Average final distribution of synaptic strengths for a typical *non*-cholinergic network. This distribution constitutes a much lower network potentiation value (≈ 0) due to a greater proportion of synapses with zero synaptic strength values. In panels (c)-(f), the re-wiring probability was 0.60 and $w_{max} = 0.08$ mS/cm^2. Panels (e) and (f) represent histograms averaged over ten different network initializations.

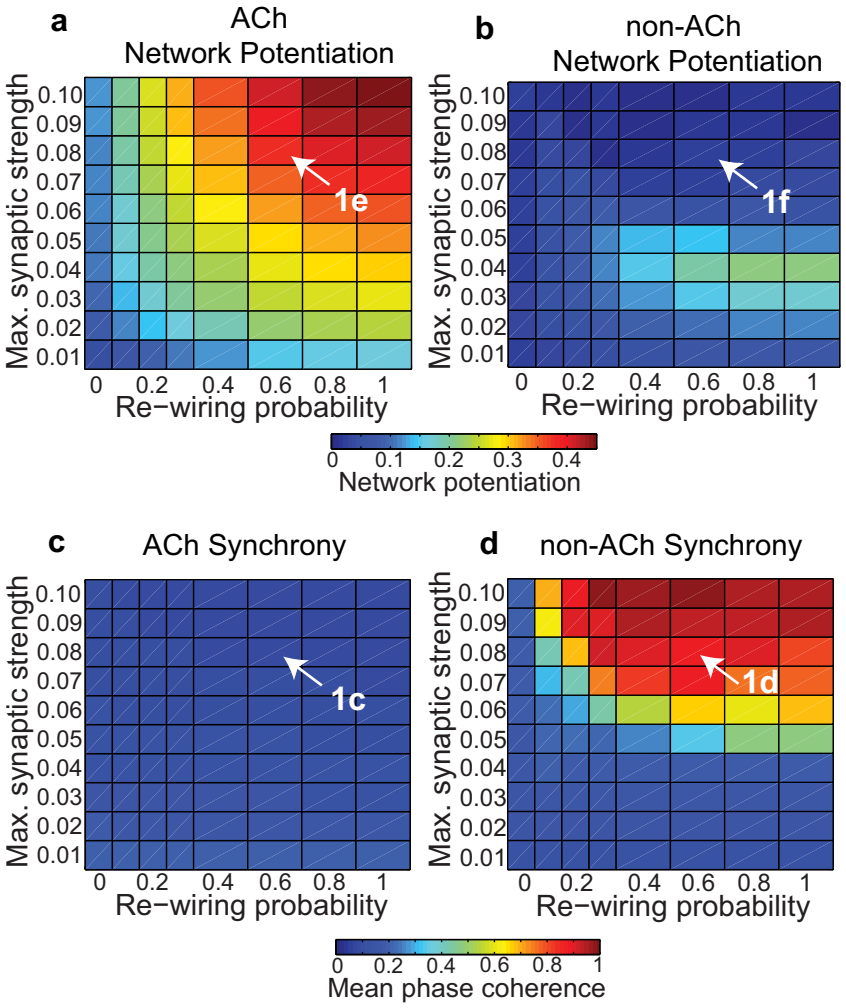

Figure 4.2: Effects of acetylcholine on network potentiation and synchronization for varied network parameters. (a,b) Network potentiation as a function of re-wiring probability (controlling randomness of network connections, x-axis) and maximum synaptic strength (w_{max}, y-axis) for model cortical networks both with (a) and without (b) simulated cholinergic modulation. Note the much greater potentiation of cholinergic networks for virtually all network parameters, and especially for $w_{max} \gtrsim 0.05$ mS/cm^2. (c,d) Network synchrony, as measured by mean phase coherence, as a function of re-wiring probability and w_{max} for networks with (c) and without (d) simulated cholinergic modulation. All results represent averages over ten randomly-initialized network simulations. Arrows indicate network parameters which gave rise to panels c, d, e, and f in Fig. 4.1.

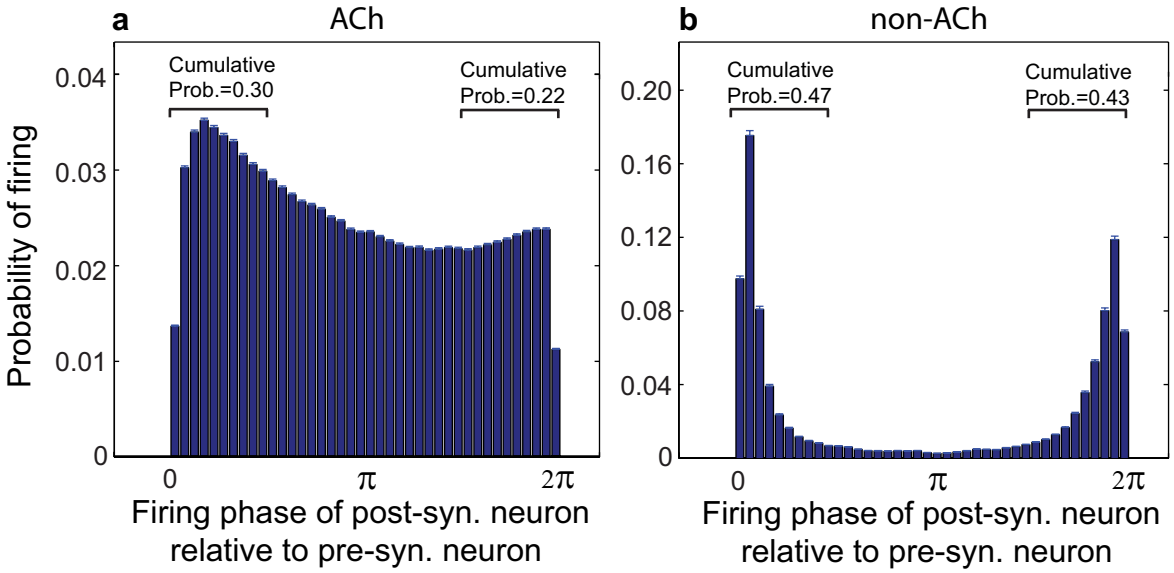

Figure 4.3: Structure of neuronal firing of pre- and post-synaptic cell pairs in cholinergic and non-cholinergic cortical networks. (a,b) Spike-timing histogram of phases of post-synaptic cell firing relative to pre-synaptic cell firing in the model cortical network both with (a) and without (b) simulated cholinergic modulation. These plots were constructed by averaging the spike-timing histograms of all pre-post pairs throughout the entire network. (a) In cholinergic networks, post-synaptic cells were much more likely to fire shortly *after* (as opposed to shortly before) pre-synaptic spikes, as evidenced by the fact that the cumulative probability of firing within the interval $[0, \pi/2]$ (0.30) was substantially larger than the cumulative probability of firing within the interval $[3\pi/2, 2\pi]$ (0.22). (b) In non-cholinergic networks, post-synaptic spike timings were more balanced between shortly preceding and shortly succeeding pre-synaptic spikes, leading to much lower network potentiation via the STDP rule. Both histograms were computed from simulations in which the re-wiring probability was 0.60 and $w_{max} = 0.08$ mS/cm^2. Note the different scales on the y-axes.

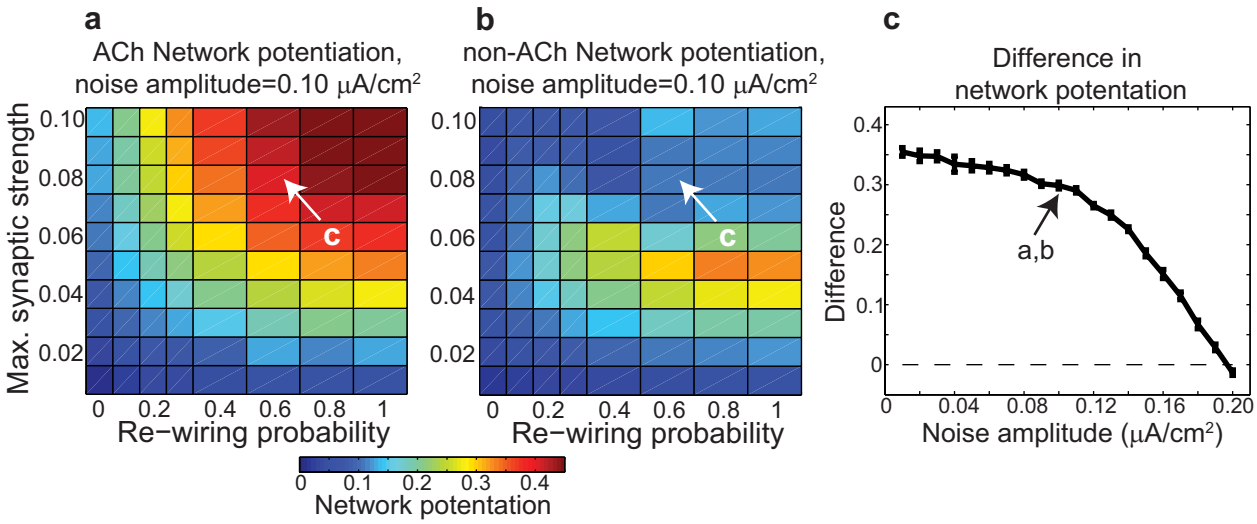

Figure 4.4: Effects of noise amplitude on the difference in network potentiation between networks with and without cholinergic modulation. (a,b) Network potentiation as a function of re-wiring probability (x-axis) and maximum synaptic strength w_{max} (y-axis) for networks with (a) and without (b) cholinergic modulation, with noise amplitude fixed at 0.10 μA/cm^2. Note that networks with cholinergic modulation exhibited much greater potentiation than those without cholinergic modulation for $w_{max} \gtrsim 0.05\mu$A/cm^2. (c) Difference in network potentiation between cholinergic and non-cholinergic networks as a function of noise amplitude for the network parameters indicated by arrows in panels (a) and (b).

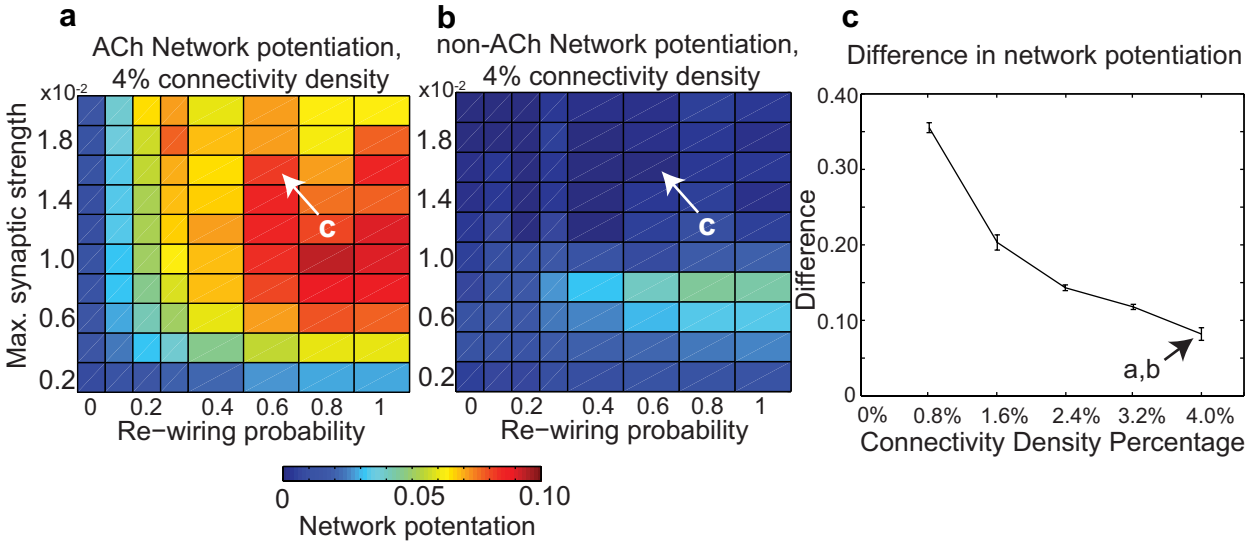

Figure 4.5: Effects of connectivity density upon network potentiation. (a,b) Network potentiation of ACh and non-ACh networks with 4.0 % connectivity density. Network potentiation is displayed as a function of w_{max} and re-wiring probability, as in Fig. 4.2. Note the difference in scale between these plots and Fig. 4.2. (c) Difference between ACh and non-ACh network potentiation values as a function of connectivity density for networks with parameters analogous to those indicated by arrows in panels (a) and (b). In order to investigate similar regimes of network excitability, we decreased w_{max} in proportion to the increase in connectivity density.

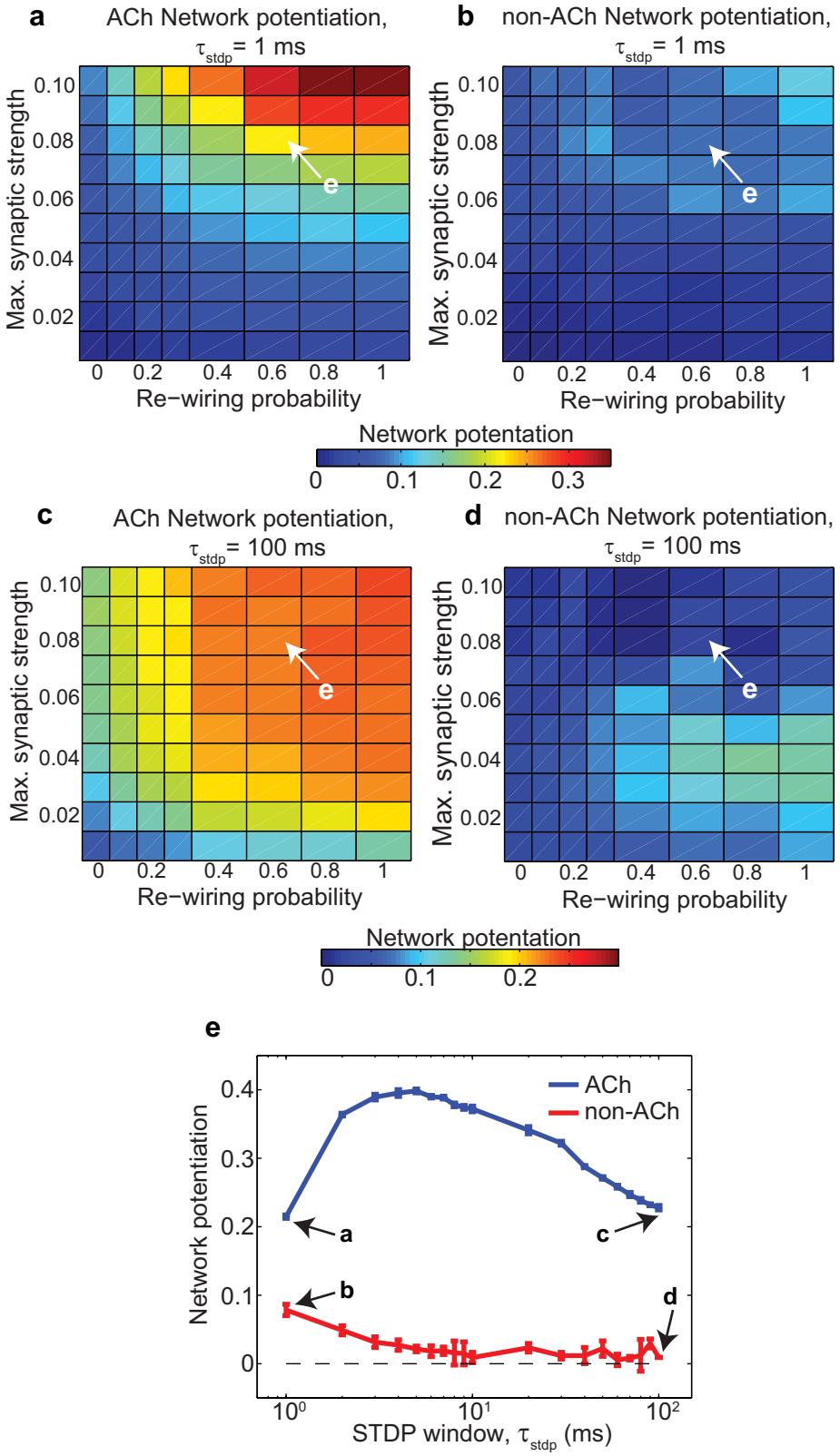

Figure 4.6: Effects of the modulation of the STDP window, τ_{stdp}, upon network potentiation. (a,b) Network potentiation of ACh and non-ACh networks as a function of w_{max} and re-wiring probability for $\tau_{\text{stdp}} = 1.0$ ms. (c,d) Network potentiation of ACh and non-ACh networks as a function of w_{max} and re-wiring probability for $\tau_{\text{stdp}} = 100.0$ ms. (e) Network potentiation of both ACh and non-ACh networks as a function of τ_{stdp}, with $w_{max} = 0.08\text{mS/cm}^2$ and a re-wiring probability of 0.60.

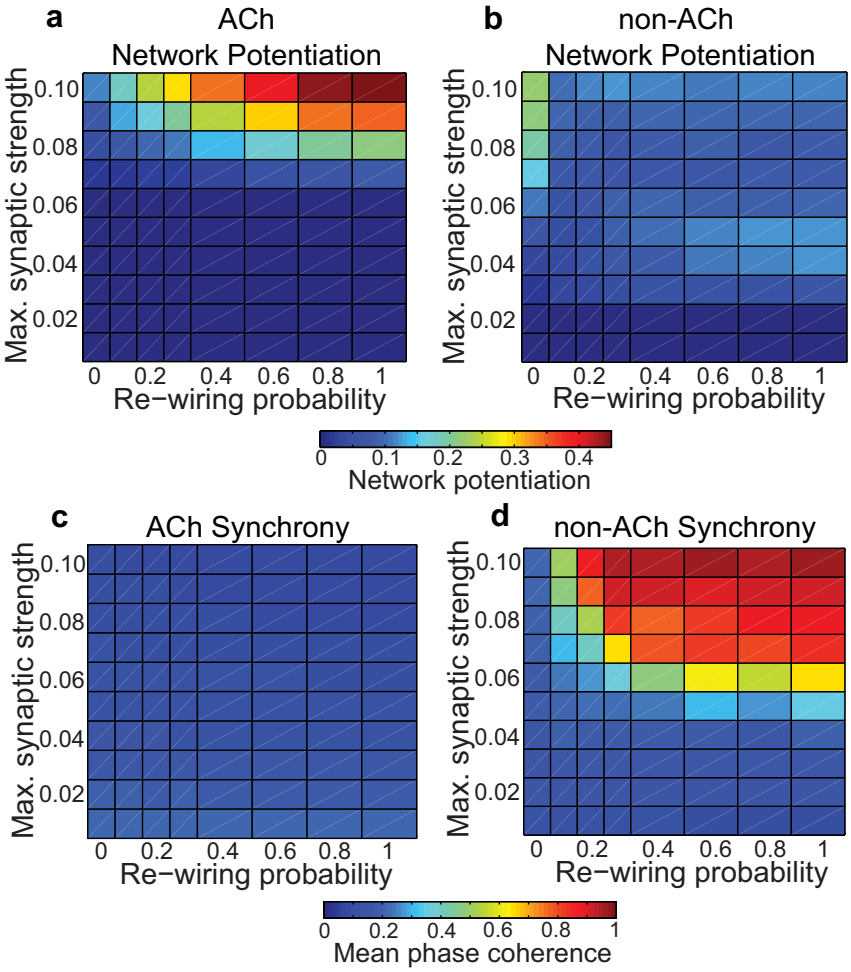

Figure 4.7: Effects of acetylcholine on network potentiation (a,b) and synchronization (c,d) for varied network parameters with an asymmetric STDP rule that favors LTD over LTP. STDP parameters were $\tau_- = 40$ ms, $\tau_+ = 20$ ms, $A_+ = w_{max}/10$, and $A_- = 1.1 \times (\tau_+/\tau_-) \times A_+$.

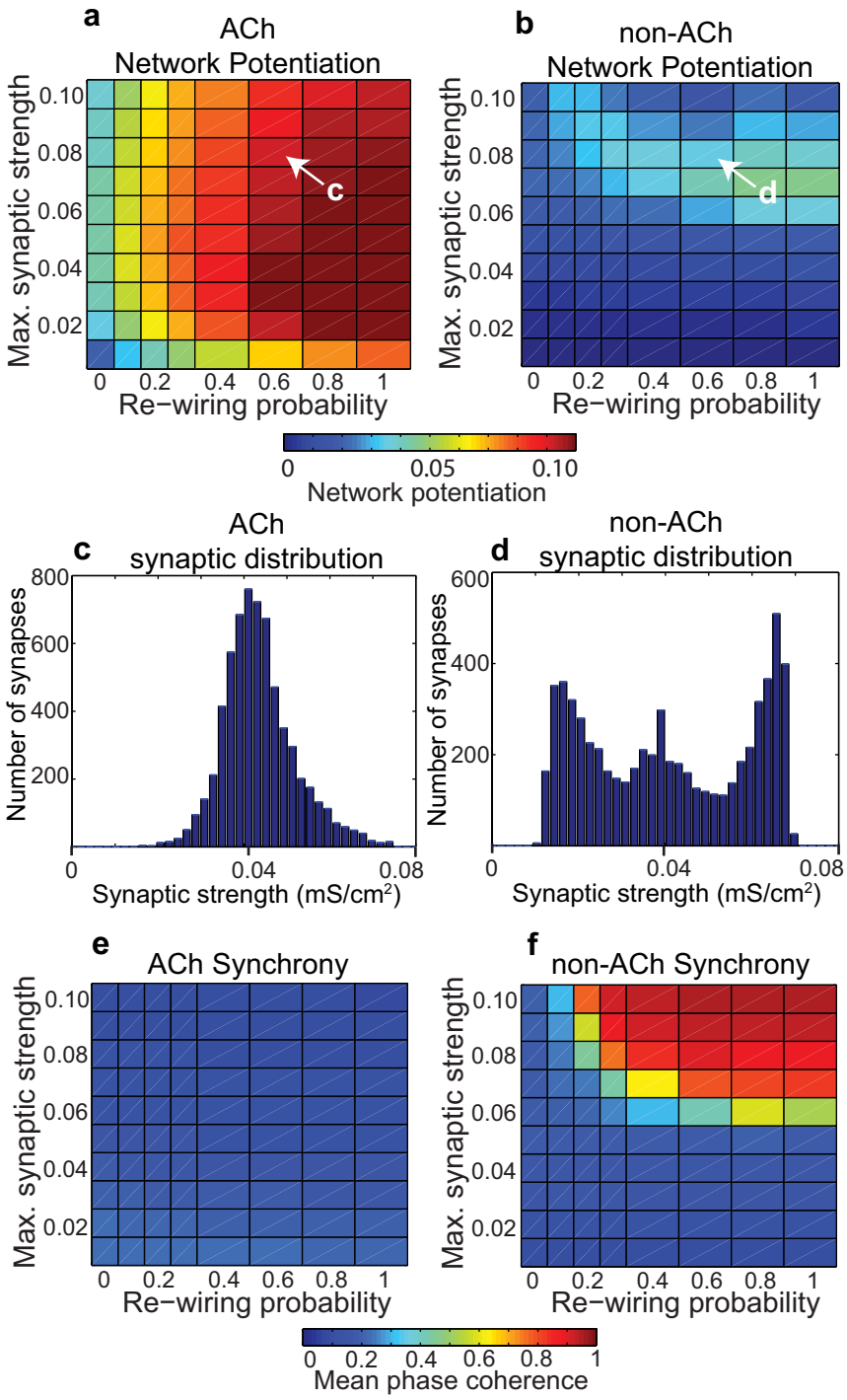

Figure 4.8: Effects of acetylcholine on network potentiation (a,b) and synchronization (e,f) for varied network parameters with a multiplicate (weight-dependent) STDP rule. As found in previous results, the distribution of synaptic weights is not bimodal (c,d). Nevertheless, ACh modulation promotes overall network potentiation as illustrated in the asymmetry of the distribution profile (c).

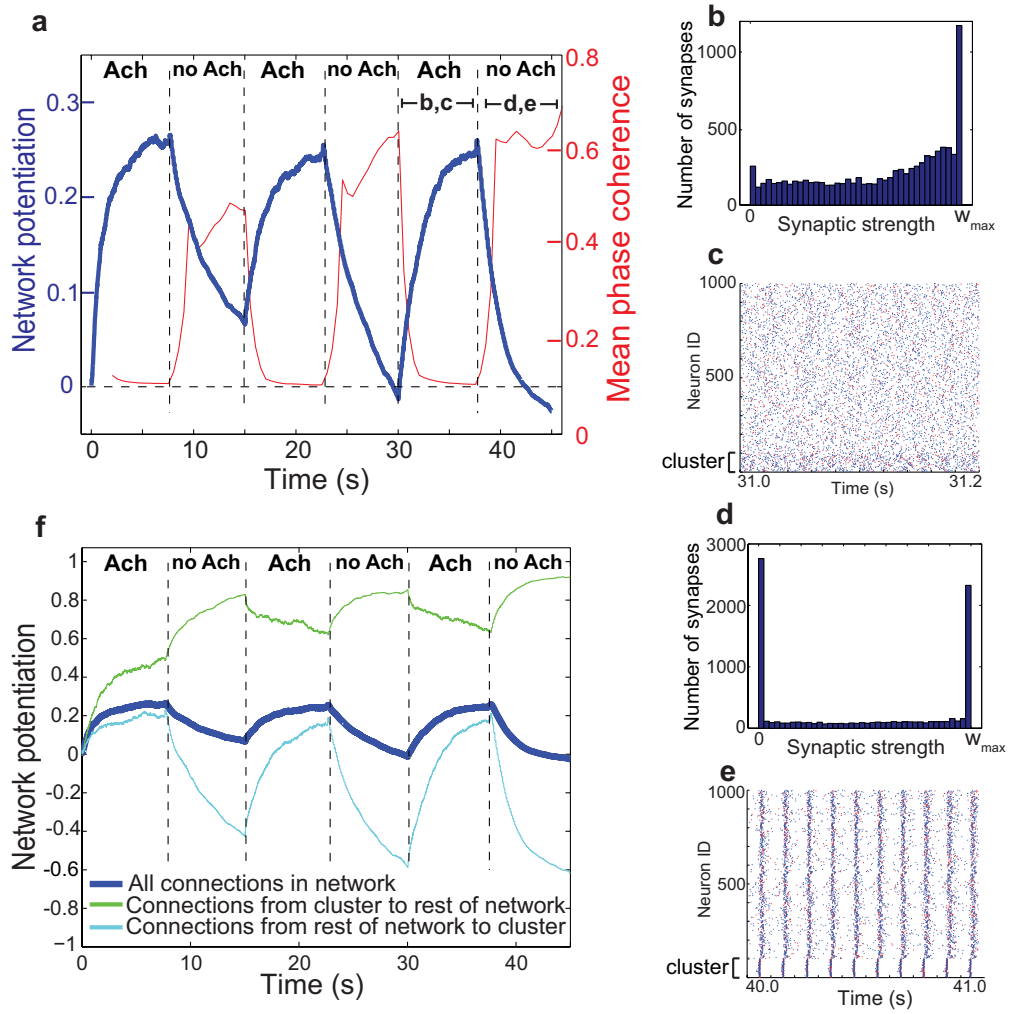

Figure 4.9: Effects of alternately switching between the presence and absence of cholinergic modulation in a cortical network with an embedded cluster. (a) Network potentiation and synchronization (as measured by mean phase coherence) of the cortical network as a function of time as the presence and absence of simulated ACh was alternated (different intervals are demarcated by dashed lines). (b) Distribution of synaptic strength values at the end of the last cholinergic interval. (c) Representative raster plot of network activity during the last cholinergic interval. The first 50 neurons comprise the cluster. (d) Distribution of synaptic strength values at the end of the last non-cholinergic interval. Note how the number of connections whose synaptic strength went to 0 is greater than the number that went to w_{max}. (e) Representative raster plot of network activity during the last non-cholinergic interval. Note how the tight bursting of the cluster drove activity in the rest of the network. (f) Network potentiation computed from distributions of synaptic weights for all synaptic connections (heavy blue curve, as shown in (a)), for synapses originating in the cluster and projecting outside the cluster (green curve), and for synaptic connections originating outside the cluster and projecting to the cluster (light blue curve). During the non-cholinergic intervals, the connections originating outside the cluster and projecting to the cluster showed extreme depotentiation due to the driving of the rest of the network by the cluster.

CHAPTER V

Summmary and conclusions

This dissertation has followed the paradigm of modern neuroscience in seeking to understand the physical substrates of behavior and cognition. Though it is a daunting task to sift through the $\sim 10^{15}$ connections of the human brain in search of universal principles, the progress that has already been made offers hope for future investigation. We know, first of all, that the neuron is the building block of the brain and that its primary function is to transmit electrochemical signals. We know that individual neurons may encode information in their firing rates, and that populations of neurons with complementary tuning curves can perform tasks as diverse as mapping spatial environments, processing visual signals, and coordinating movements. We also know that neuronal synchronization supports the integration of disparate sensory input into unified perceptions, and that memory formation results from plastic changes in the strengths of synapses. This dissertation has focused upon extending our understanding of these last two themes, beginning with an investigation of how network synchrony interacts with network firing frequency, and concluding with a study of how the function of sleep may depend upon the plastic changes in connection strength that result from switching synchronization states.

In Chapter II, we described how phase response curves help to predict network

synchronization, and specifically how network synchronization is affected by modulation of network firing frequency. Using the Morris-Lecar neuron model, we showed that while both Type I and Type II PRC amplitudes are attenuated as frequency increases, Type II PRCs show an asymmetric attenuation, with the phase delay region being affected much more than the phase advance region. Because it is the presence of the phase delay region that endows Type II neurons with enhanced synchronization capabilities, this suggested that Type II neuronal synchronization might decrease with increased frequency. Our network simulations showed that this is in fact the case. As a control, we also investigated how Type I network synchronization changes with increased synchrony, and found no parameter regime where synchronization appreciably decreased with increased network frequency. This was consistent with PRC analysis, since the Type I PRC showed relatively uniform attentuation with increasing frequency.

Chapter III continued the investigation of frequency's effect upon synchrony using a more realistic neuron model. This neuron model was particularly interesting because it was based upon the first ever experimental demonstration that neuromodulation can switch neuronal PRC type [96] (application of acetylcholine switches the PRCs of cortical pyramidal cells from Type II to Type I). In this model, too, increased frequency produced much greater attenuation of phase delays than phase advances for Type II PRCs. We showed that this was a result of the slow speed of hyperpolarizing potassium currents relative to depolarizing sodium currents, then proceeded to demonstrate that network synchrony decreased with increased frequency in networks composed of Type II neurons. Neurons with Type I PRCs were again used as a control, with the same result as before: frequency modulation had relatively little effect upon network synchrony for most network parameters. Together, the results from

Chapters II and III suggest that PRCs are excellent tools for predicting and understanding the synchronization properties of large-scale neuronal networks. The results also suggest a possible method by which the brain may restrict synchronization to low frequency bands.

In Chapter IV, we proposed a potential biophysical mechanism to support the synaptic renormalization hypothesis. This was a dynamical mechanism which depended upon the effects of cholinergic modulation on network synchronization. Using the pyramidal neuron model from Chapter III, we modeled waking by simulating cholinergic modulation in a network of 1000 cells. This modulation induced asynchronous network dynamics, which in turn resulted in elevated network potentiation due to spike-timing dependent plasticity. The fact that asynchronous dynamics could lead to elevated network potentiation was counterintuitive, but it made sense once we showed that network activity was not entirely random: post-synaptic neurons were more likely to fire shortly after (as opposed to shortly before) pre-synaptic neurons. Sleep was modeled by simulating the absence of cholinergic modulation, which resulted in highly synchronous network dynamics because the neurons had Type II PRCs. This synchronous network activity led to depressed network potentiation relative to simulated waking, effectively reproducing the results predicted by the synaptic renormalization hypothesis. Our simulations therefore suggest that experimentalists should investigate the dynamical effects of acetylcholine as a potential mechanism for synaptic renormalization.

Taken together, this work emphasizes the importance of understanding neuronal dynamics in order to elucidate brain function. The phase response curve has proven to be a very useful tool in this endeavor. The insight it provides into the synchronization of thousands of neurons is powerful, especially considering that it characterizes

the dynamics of just individual neurons. To make further progress in understanding the brain, theorists and experimentalists alike must continue to develop powerful, innovative tools to characterize neuronal dynamics, for it is only by seeking fundamental principles governing the quadrillions of interactions in the brain that we may hope to fully understand the physical basis for behavior and cognition.

BIBLIOGRAPHY

BIBLIOGRAPHY

[1] E Kandel. In *In Search of Memory: The Emergence of a New Science of Mind*. Norton & Company, 2006.

[2] E Kandel, J Schwartz, and T Jessel. In *Principles of Neural Science*. McGraw-Hill Medical, 2000.

[3] G Buzsaki. In *Rhythms of the Brain*. Oxford University Press, USA, 2006.

[4] J Hawkins and S Blakeslee. In *On Intelligence*. Henry Holt and Company, 2004.

[5] TP Trappenberg. In *Fundamentals of Computational Neuroscience*. Oxford University Press, 2010.

[6] ED Adrian. The impulses produced by sensory nerve endings. part I. *Journal of Physiology-London*, 61:49–72, 1926.

[7] RJ Snowden, S Treue, and RA Andersen. The response of neurons in areas V1 and MT of the alert rhesus monkey to moving random dot patterns. *Experimental Brain Research*, 88:389–400, 1992.

[8] J O'Keefe and J Dostrovsky. The hippocampus as a spatial map: Preliminary evidence from unit activity in the freely-moving rat. *Brain Research*, 34:171–175, 1971.

[9] AD Ekstrom, MJ Kahana, JB Caplan, TA Fields, EA Isham, EL Newman, and I Fried. Cellular networks underlying human spatial navigation. *Nature*, 425:184–187, 2003.

[10] AP Georgopoulos, AB Schwartz, and RE Kettner. Neuronal population coding of movement direction. *Science*, 233:1416–1419, 1986.

[11] DM Taylor, SI Helms Tillery, and AB Schwartz. Direct cortical control of 3D neuroprosthetic devices. *Science*, 296:1829–1832, 2002.

[12] LR Hochberg, D Bacher, B Jarosiewicz, NY Masse, JD Simeral, J Vogel, S Haddadin, J Liu, SS Cash, P vander Smagt, and JP Donoghue. Reach and grasp by people with tetraplegia using a neurally controlled robotic arm. *Nature*, 485:372–375, 2012.

[13] JP Bacon and RK Murphey. Receptive fields of cricket giant interneurones are related to their dendritic structure. *Journal of Physiology*, 352:601–623, 1984.

[14] O Tudusciuc and A Nieder. Contributions of primate prefrontal and posterior parietal cortices to length and numerosity representation. *Journal of Neurophysiology*, 101:2984–2994, 2009.

[15] K Takeda and S Funahashi. Prefrontal task-related activity representing visual cue location or saccade direction in spatial working memory tasks. *Journal of Neurophysiology*, 87:567–588, 2002.

[16] MA Montemurro, MJ Rasch, Y Murayama, NK Logothetis, and S Panzeri. Phase-of-firing coding of natural visual stimuli in primary visual cortex. *Current Biology*, 18:375–380, 2008.

[17] E Salinas and TJ Sejnowski. Correlated neuronal activity and the flow of neural information. *Nature Reviews Neuroscience*, 2:539–550, 2001.

[18] CE Carr and M Konishi. A circuit for detection of interaural time differences in the brain stem of the barn owl. *Journal of Neuroscience*, 10:3227–3248, 1990.

[19] K MacLeod, A Backer, and G Laurent. Who reads temporal information contained across synchronized and oscillatory spike trains? *Nature*, 395:693–698, 1998.

[20] M Stopfer, S Bhagavan, BH Smith, and G Laurent. Impaired odor discrimination on desynchronization of odour-encoding neural assemblies. *Nature*, 390:70–74, 1997.

[21] PN Steinmetz, A Roy, PJ Fitzgerald, SS Hsiao, KO Johnson, and E Niebur. Attention modulates synchronized neuronal firing in primate somatosensory cortex. *Nature*, 404:187–190, 2000.

[22] U Rutishauser, IB Ross, AN Mamelak, and EM Schuman. Human memory strength is predicted by theta-frequency phase-locking of single neurons. *Nature*, 464:903–907, 2010.

[23] CM Gray. The temporal correlation hypothesis of visual feature integration: Still alive and well. *Neuron*, 24:31–47, 1999.

[24] PM Milner. Model for visual shape recognition. *Psychological Review*, 81:521–535, 1974.

[25] C von der Malsburg. Nervous structures with dynamic links. *Berichte der Bunsengesellschaft fr physikalische Chemie*, 89:703–710, 1985.

[26] CM Gray, P Konig, AK Engel, and W Singer. Oscillatory responses in cat visual cortex exhibit inter-columnar synchronization which reflects global stimulus properties. *Nature*, 338:334–337, 1989.

[27] G Pareti and M de Palma. Does the brain oscillate? the dispute on neuronal synchronization. *Neurological Sciences*, 25:41–47, 2004.

[28] R Levy, WD Hutchison, AM Lozano, and JO Dostrovsky. High-frequency synchronization of neuronal activity in the subthalamic nucleus of Parkinsonian patients with limb tremor. *Journal of Neuroscience*, 20:7766–7775, 2000.

[29] W Penfield, H Jaspers, and F McNaughton. In *Epilepsy and the Functional Anatomy of the Human Brain*. Boston: Little Brown, 1954.

[30] TI Netoff and SJ Schiff. Decreased neuronal synchronization during experimental seizures. *J Neurosci*, 22:7297–7307, 2002.

[31] LG Dominguez, RA Wennberg, W Gaetz, D Cheyne, OC Snead, and JLP Velasquez. Enhanced synchrony in epileptiform activity? - Local versus distant phase synchronization in generalized seizures. *Journal of Neuroscience*, 25:8077–8084, 2005.

[32] PH Uhlhaas and W Singer. Neural synchrony in brain disorders: relevance for cognitive dysfunctions and pathophysiology. *Neuron*, 52:155–168, 2006.

[33] J Brock, CC Brown, J Boucher, and G Rippon. The temporal binding deficit hypothesis of autism. *Development and Psychopathology*, 14:209–224, 2002.

[34] KM Stiefel, BS Gutkin, and TJ Sejnowski. The effects of cholinergic neuromodulation on neuronal phase-response curves of modeled cortical neurons. *J Comput Neurosci*, 26:289–301, 2009.

[35] D Hansel, G Mato, and C Meunier. Synchrony in excitatory neural networks. *Neural Comput*, 7:307–337, 1995.

[36] B Ermentrout. Type i membranes, phase resetting curves, and synchrony. *Neural Comput*, 8:979–1001, 1996.

[37] CC Canavier, RJ Butera, RO Dror, DA Baxter, JW Clark, and JH Byrne. Phase response characteristics of model neurons determine which patterns are expressed in a ring circuit model of gait generation. *Biol Cybern*, 77:367–380, 1997.

[38] R Dror, CC Canavier, RJ Butera, JW Clark, and JH Byrne. A mathematical criterion based on phase response curves for stability in a ring of coupled oscillators. *Biol Cybern*, 80:11–23, 1999.

[39] SK Maran and CC Canavier. Using phase resetting to predict 1:1 and 2:2 locking in two neuron networks in which firing order is not always preserved. *J Comput Neurosci*, 24:37–55, 2008.

[40] C Luo, JW Clark, CC Canavier, DA Baxter, and JH Byrne. Multimodal behavior in a four neuron ring circuit: Mode switching. *IEEE T Bio-Med Eng*, 51:205–218, 2004.

[41] C van Vreeswijk, LF Abbott, and GB Ermentrout. When inhibition not excitation synchronizes neural firing. *Journal of Computational Neuroscience*, 1:313–321, 1994.

[42] RM Smeal, GB Ermentrout, and JA White. Phase-response curves and synchronized neural networks. *Philosophical Transactions of the Royal Society B*, 365:2407–2422, 2010.

[43] AA Sharp, MB O'Neil, LF Abbott, and E Marder. The dynamic clamp: artificial conductances in biological neurons. *Trends in Neuroscience*, 16:389–394, 1993.

[44] AA Sharp, MB O'Neil, LF Abbott, and E Marder. Dynamic clamp: computer-generated conductances in real neurons. *Journal of Neurophysiology*, 69:992–995, 1993.

[45] TI Netoff, MI Banks, AD Dorval, CD Acker, JS Haas, N Kopell, and JA White. Synchronization in hybrid neuronal networks of the hippocampal formation. *Journal of Neurophysiology*, 93:1197–1208, 2005.

[46] A Bogaard, J Parent, M Zochowski, and V Booth. Interaction of cellular and network mechanisms in spatiotemporal pattern formation in neuronal networks. *J Neurosci*, 29:1677–1687, 2009.

[47] XJ Wang and G Buzsaki. Gamma oscillation by synaptic inhibition in a hippocampal interneuronal network model. *Journal of Neuroscience*, 16:6402–6413, 1996.

[48] N Masuda and K Aihara. Global and local synchrony of coupled neurons in small-world networks. *Biological Cybernetics*, 90:302–309, 2004.

[49] CC Hilgetag, GAPC Burns, MC O'Neill, JW Scannell, and MP Young. Anatomical connectivity defines the organization of clusters of cortical areas in the macaque monkey and the cat. *Philosophical Transactions of the Royal Society of London Series B-Biological Sciences*, 355:91–110, 2000.

[50] DJ Watts and DH Strogatz. Collective dynamics of "small-world" networks. *Nature*, 393:440–442, 1998.

[51] S Boccaletti, V Latora, Y Moreno, M Chavez, and DU Hwang. Complex networks: Structure and dynamics. *Physics Reports*, 424:175–308, 2006.

[52] O Sporns and JD Zwi. The small world of the cerebral cortex. *Neuroinformatics*, 2:145–162, 2004.

[53] DO Hebb. In *The Organization of Behavior*. Wiley, 1949.

[54] TVP Bliss and T Lomo. Long-lasting potentiation of synaptic transmission in dentate area of anesthetized rabbit following stimulation of perforant path. *Journal of Physiology-London*, 232:331–356, 1973.

[55] In T Bliss, G Collingridge, and R Morris, editors, *LTP:Long-Term Potentiation*. Oxford University Press, 2003.

[56] SGN Grant, TJ O'Dell, KA Karl, PL Stein, and ER Kandel. Impaired long-term potentiation, spatial learning, and hippocampal development in fyn mutant mice. *Science*, 258:1903–1910, 1992.

[57] AJ Silva, R Paylor, JM Wehner, and S Tonegawa. Impaired spatial learning in alpha-calcium-calmodulin kinase II mutant mice. *Science*, 257:206–211, 1992.

[58] SJ Martin, PD Grimwood, and RGM Morris. Synaptic plasticity and memory: An evaluation of the hypothesis. *Annual Review of Neuroscience*, 23:649–711, 2000.

[59] S Corkin. Lasting consequences of bilateral medial temporal lobectomy: Clinical course and experimental findings in h.m. In *Seminars in Neurology*. Thieme-Stratton Inc., 1984.

[60] D Marr. A theory for cerebral neocortex. *Proceedings of the Royal Society of London B*, 176:161–234, 1970.

[61] D Marr. Simple memory: a theory for archicortex. *Philosophical Transactions of the Royal Society of London B*, 262:23–81, 1971.

[62] MA Wilson and BL McNaughton. Reactivation of hippocampal ensemble memories during sleep. *Science*, 265:676–679, 1994.

[63] KL Hoffman and BL McNaughton. Coordinated reactivation of distributed memory traces in primate neocortex. *Science*, 297:2070–2073, 2002.

[64] G Girardeau, K Benchenane, SI Wiener, G Buzsaki, and MB Zugaro. Selective suppression of hippocampal ripples impairs spatial memory. *Nature Neuroscience*, 12:1222–1223, 2009.

[65] V Ego-Stengel and MA Wilson. Disruption of ripple-associated hippocampal activity during rest impairs spatial learning in the rat. *Hippocampus*, 20:1–10, 2010.

[66] PW Frankland and B Bontempi. The organization of recent and remote memories. *Nature Reviews Neuroscience*, 6:119–130, 2005.

[67] D Ji and MA Wilson. Coordinated memory replay in the visual cortex and hippocampus during sleep. *Nature Neuroscience*, 10:100–107, 2007.

[68] G Bi and M Poo. Synaptic modifications in cultured hippocampal neurons: Dependence on spiking timing, synaptic strength, and postsynaptic cell type. *Journal of Neuroscience*, 18:10464–10472, 1998.

[69] S Song and LF Abbott. Cortical development and remapping through spike-timing dependent plasticity. *Neuron*, 32:339–350, 2001.

[70] E Oja. A simplied neuron model as a principal component analyzer. *Journal of Mathematical Biology*, 15:267–273, 1982.

[71] A Kepecs, MCW van Rossum, S Song, and J Tegner. Spike-timing-dependent plasticity: common themes and divergent vistas. *Biological Cybernetics*, 87:446–458, 2002.

[72] A Rechtschaffen, MA Gilliland, BM Bergmann, and JB Winter. Physiological correlates of prolonged sleep-deprivation in rats. *Science*, 221:182–184, 1983.

[73] A Rechtschaffen and BM Bergmann. Sleep deprivation in the rat: An update of the 1989 paper. *Biological Cybernetics*, 25:18–24, 2002.

[74] K Gumustekin, B Seven, N Karabulutand O Aktas, N Gursan, S Aslan, M Keles, E Varoglu, and S Dane. Effects of sleep deprivation, nicotine, and selenium on wound healing in rats. *International Journal of Neuroscience*, 114:1433–1442, 2004.

[75] A Zager, ML Andersen, FS Ruiz, IB Antunes, and S Tufik. Effects of acute and chronic sleep loss on immune modulation of rats. *American Journal of Physiology-Regulatory Integrative and Comparative Physiology*, 293:R504–R509, 2007.

[76] S Diekelmann and J Born. The memory function of sleep. *Nature Reviews Neuroscience*, 11:114–126, 2010.

[77] AL Loomis, EN Harvey, and G Hobart. Further observations on the potential rhythms of the cerebral cortex during sleep. *Science*, 82:198–200, 1935.

[78] H Schulz. Rethinking sleep analysis. *Journal of Clinical Sleep Medicine*, 4:99–103, 2008.

[79] P Maquet, JM Peters, J Aerts, G Delfiore, C Degueldre, A Luxen, and G Franck. Functional neuroanatomy of human rapid-eye-movement sleep and dreaming. *Nature*, 383:163–166, 1996.

[80] BE Jones. Paradoxical sleep and its chemical/structural substrates in the brain. *Neuroscience*, 40:637–656, 1992.

[81] R Llinas and U Ribary. Coherent 40-Hz oscillation characterizes dream state in humans. *Proceedings of the National Academy of Sciences*, 90:2078–2081, 1993.

[82] R Hess. Sleep and sleep disturbances in the electroencephalogram. *Progress in Brain Research*, 18:127–139, 1965.

[83] MP Walker. In MB Miller and A Kingstone, editors, *Year in Cognitive Neuroscience 2009*. 2009.

[84] D Aeschbach, AJ Cutler, and JM Ronda. A role for non-rapid-eye-movement sleep homeostasis in perceptual learning. *Journal of Neuroscience*, 28:2766–2772, 2008.

[85] L Marshall, H Helgadottir, M Molle, and J Born. Boosting slow oscillations during sleep potentiates memory. *Nature*, 444:610–613, 2006.

[86] A Sirota, J Csicsvari, D Buhl, and G Buzsaki. Communication between neocortex and hippocampus during sleep in rodents. *Proceedings of the National Academy of Science*, 100:2065–2069, 2003.

[87] A Sirota and G Buzsaki. Interaction between neocortical and hippocampal networks via slow oscillations. *Thalamus and Related Systems*, 3:245–259, 2005.

[88] AK Lee and MA Wilson. Memory of sequential experience in the hippocampus during slow wave sleep. *Neuron*, 36:1183–1194, 2002.

[89] G Tononi and C Cirelli. Sleep and synaptic homeostasis: a hypothesis. *Brain Research Bulletin*, 62:143–150, 2003.

[90] G Tononi and C Cirelli. Sleep function and synaptic homeostasis. *Sleep Medicine Reviews*, 10:49–62, 2006.

[91] VV Vyazovskiy, C Cirelli, M Pfister-Genskow, U Faraguna, and G Tononi. Molecular and electrophysiological evidence for net synaptic potentiation in wake and depression in sleep. *Nature Neuroscience*, 11:200–208, 2008.

[92] R Huber, H Maki, M Rosanova, S Casarotto, P Canali, AG Casali, G Tononi, and M Massimini. Human cortical excitability increases with time awake. *Cerebral Cortex*, 2012.

[93] VV Vyazovskiy, U Olcese, YM Lazimy, U Faraguna, SK Esser, JC Williams, C Cirelli, and G Tononi. Cortical firing and sleep homeostasis. *Neuron*, 63:865–878, 2009.

[94] R Huber, SK Esser, F Ferrarelli, M Massimini, MJ Peterson, and G Tononi. TMS-induced cortical potentiation during wakefulness locally increases slow wave activity during sleep. *PLoS ONE*, 2:10.1371/journal.pone.0000276, 2007.

[95] EC Hanlon, VV Vyazoyskiy, U Faraguna, G Tononi, and C Cirelli. Synaptic potentiation and sleep need: Clues from molecular and electrophysiological studies. *Current Topics in Medicinal Chemistry*, 11:2472–2482, 2011.

[96] KM Stiefel, BS Gutkin, and TJ Sejnowski. Cholinergic neuromodulation changes phase response curve shape and type in cortical pyramidal neurons. *PLoS ONE*, 3(e3947), 2008.

[97] NW Schultheiss, JR Edgerton, and D Jaeger. Phase response curve analysis of a full morphological globus pallidus neuron model reveals distinct perisomatic and dendritic modes of synaptic integration. *J Neurosci*, 7:2767–2782, 2010.

[98] CG Fink, V Booth, and M Zochowski. Effects of the frequency dependence of phase response curves on network synchronization. In NW Schultheiss, AA Prinz, and RJ Butera, editors, *Phase Response Curves in Neuroscience*. Springer Science, 2012.

[99] C Morris and H Lecar. Voltage oscillations in the barnacle giant muscle fiber. *Biophys J*, 35:193–213, 1981.

[100] J Rinzel and B Ermentrout. Analysis of neural excitability and oscillations. In C Koch and I Segev, editors, *Methods in Neuronal Modeling*. MIT Press, 1998.

[101] F Mormann, K Lehnertz, P David, and CE Elger. Mean phase coherence as a measure for phase synchronization and its application to the eeg of epilepsy patients. *Physica D*, 144:358–369, 2000.

[102] CG Fink, V Booth, and M Zochowski. Cellulary-driven differences in network synchronization propensity are differentially modulated by firing frequency. *PLoS Computational Biology*, 7:10.1371/journal.pcbi.1002062, 2011.

[103] F Varela, JP Lachaux, E Rodriguez, and J Martinerie. The brainweb: phase synchronization and large-scale integration. *Nat Rev Neurosci*, 2:229–239, 2001.

[104] Roelfsema, AK Engel, P Konig, and W Singer. Visuomotor integration is associated with zero time-lag synchronization among cortical areas. *Nature*, 385:157–161, 1997.

[105] SL Bressler. Interareal synchronization in the visual cortex. *Behav Brain Res*, 76:37–49, 1996.

[106] E Rodriguez. Perceptions' shadow: long-distance synchronization of human brain activity. *Nature*, 397:430–433, 1999.

[107] E Niedermeyer. *Electroencephalography: Basic Principles, Clinical Applications, And Related Fields*. Philadelphia: Lippincott Williams and Wilkins, 2005.

[108] P Brown. The oscillatory nature of human basal ganglia activity: relationship to the pathophysiology of parkinson's disease. *Movement Disord*, 18:357–363, 2003.

[109] CJ Stam, T Montez, BJ Jones, SA Rombouts, Y van der Made, YA Pifnenburg, and P Scheltens. Disturbed fluctuations of resting state eeg synchronization in alzheimer's disease. *Clin Neurophysiol*, 116:708–715, 2005.

[110] JS Kwon, BF O'Donnell, GV Wallenstein, RW Greene, Y Hirayasu, PG Nestor, ME Hasselmo, GF Potts, ME Shenton, and RW McCarley. Gamma frequency-range abnormalities to auditory stimulation in schizophrenia. *Arch Gen Psychiat*, 56:1001–1005, 1999.

[111] B Ermentrout, Matthew Pascal, and B Gutkin. The effects of spike frequency adaptation and negative feedback on the synchronization of neural oscillators. *Neural Comput*, 13:1285–1310, 2001.

[112] BS Gutkin, B Ermentrout, and AD Reyes. Phase response curves give the responses of neurons to transient inputs. *J Neurophysiol*, 94:1623–1635, 2005.

[113] D Golomb and Y Amitai. Propagating neuronal discharges in neocortical slides: Computational and experimental study. *J Neurophysiol*, 78:1199–1211, 1997.

[114] PH Tiesinga and TJ Sejnowski. Rapid temporal modulation of sychrony by competition in cortical interneuron networks. *Neural Comput*, 16:251–275, 2004.

[115] T Tateno and HPC Robinson. Phase resetting curves and oscillatory stability in interneurons of rat somatosensory cortex. *Biophys J*, 92:683–695, 2007.

[116] S Achuthan and CC Canavier. Phase-resetting curves determine synchronization, phase locking, and clustering in networks of neural oscillators. *J Neurosci*, 29:5218–5233, 2009.

[117] BS Gutkin and GB Ermentrout. Dynamics of membrane excitability determine interspike interval variability: A link between spike generation mechanisms and cortical spike train statistics. *Neural Comput*, 10:1047–1065, 1998.

[118] T Tateno and HPC Robinson. Rate coding and spike-time variability in cortical neurons with two types of threshold dynamics. *J Neurophysiol*, 95:2650–2663, 2006.

[119] JA Goldberg, CA Deister, and CJ Wilson. Response properties and synchronization of rhythmically firing dendritic neurons. *J Neurophysiol*, 97:208–219, 2007.

[120] JA Cardin, M Curlen, K Meletis, U Knoblich, F Zhang, K Deisseroth, LH Tsai, and CI Moore. Driving fast-spiking cells induces gamma rhythm and controls sensory responses. *Nature*, 459:663–668, 2009.

[121] RD Traub, MA Whittington, IM Stanford, and JG Jefferys. A mechanism for generation of long-range synchronous fast oscillations in the cortex. *Nature*, 383:621–624, 1996.

[122] RD Traub, JG Jefferys, and MA Whittington. Simulation of gamma rhythms in networks of interneurons and pyramidal cells. *J Comput Neurosci*, 4:141–150, 1997.

[123] MA Whittington, RD Traub, and JG Jefferys. Synchronized oscillations in interneuron networks driven by metabotropic glutamate receptor activation. *Nature*, 373:612–615, 1995.

[124] MA Whittington, HJ Faulkner, HC Doheny, and RD Traub. Neuronal fast oscillations as a target site for psychoactive drugs. *Pharmacol and Therapeut*, 86:171–190, 2000.

[125] T Netoff. How do antiepileptic drugs and epileptogenic mutations change cell and network dynamics? In *The 11th Experimental Chaos and Complexity Conference*. Universite Lille 1-Sciences at Technologies, June 2010.

[126] WD Killgore. Effects of sleep deprivation on cognition. *Prog Brain Res*, 185:105–129, 2010.

[127] MP Walker. Cognitive consequences of sleep and sleep loss. *Sleep Med*, 9 Suppl 1:S29–34, 2008.

[128] C Cirelli and G Tononi. Differential expression of plasticity-related genes in waking and sleep and their regulation by the noradrenergic system. *Journal of Neuroscience*, 20:9187–9194, 2000.

[129] Y Rao, ZW Liu, E Borok, RL Rabenstein, M Shanabrough, M Lu, MR Picciotto, TL Horvath, and XB Gao. Prolonged wakefulness induces experience-dependent synaptic plasticity in mouse hypocretin/orexin neurons. *Journal of Clinical Investigation*, 117:4022–4033, 2007.

[130] ZW Liu, U Faraguna, C Cirelli, G Tononi, and XB Gao. Direct evidence for wake-related increases and sleep-related decreases in synaptic strength in rodent cortex. *Journal of Neuroscience*, 30:8671–8675, 2010.

[131] S Maret, U Faraguna, AB Nelson, C Cirelli, and G Tononi. Sleep and waking modulate spine turnover in the adolescent mouse cortex. *Nature Neuroscience*, 14:1418–1420, 2011.

[132] D Bushey, G Tononi, and C Cirelli. Sleep and synaptic homeostasis: Structural evidence in *Drosophila*. *Science*, 332:1576–1581, 2011.

[133] M Massimini, G Tononi, and R Huber. Slow waves, synaptic plasticity and information processing: insights from transcranial magnetic stimulation and high-definition EEG experiments. *European Journal of Neuroscience*, 29:1761–1770, 2009.

[134] R Huber, S Maatta, SK Esser, S Sarasso, F Ferrarelli, A Watson, F Ferreri, and MJ Petersona nd G Tononi. Measures of cortical plasticity after transcranial paired associative stimulation predict changes in electroencephalogram slave-wave activity during subsequent sleep. *Journal of Neuroscience*, 28:7911–7918, 2008.

[135] U Faraguna, VV Vyazovskiy, AB Nelson, G Tononi, and C Cirelli. A causal role for brain-derived neurotrophic factor in the homeostatic regulation of sleep. *Journal of Neuroscience*, 23:4088–4095, 2008.

[136] N Kemp and ZI Bashir. Long-term depression: a cascade of induction and expression mechanisms. *Progress in Neurobiology*, 65:339–365, 2001.

[137] A Czarnecki, B Birtoli, and D Ulrich. Cellular mechanisms of burst firing-mediated long-term depression in rat neocortical pyramidal cells. *Journal of Physiology-London*, 578:471–479, 2007.

[138] BE Jones. From waking to sleeping: neuronal and chemical substrates. *Trends in Pharmacological Sciences*, 26:578–586, 2005.

[139] BL Jacobs and CA Fornal. Activity of brain serotonergic neurons in the behaving animal. *Pharmacological Reviews*, 43:563–578, 1991.

[140] U Olcese, SK Esser, and G Tononi. Sleep and synaptic renormalization: A computational study. *Journal of Neurophysiology*, 104:3476–3493, 2010.

[141] GH Seol, J Ziburkus, SY Huang, L Song, IT Kim, K Takamiya, RL Huganir, HK Lee, and A Kirkwood. Neuromodulators control the polarity of spike-timing-dependent synaptic plasticity. *Neuron*, 55:919–929, 2007.

[142] KM Stiefel, BS Gutkin, and TJ Sejnowski. Cholinergic neuromodulation changes phase response curve shape and type in cortical pyramidal neurons. *PLoS ONE*, 3:10.1371/journal.pone.0003947, 2008.

[143] KM Stiefel, BS Gutkin, and TJ Sejnowski. The effects of cholinergic neuromodulation on neuronal phase-response curves of modeled cortical neurons. *Journal of Computational Neuroscience*, 26:289–301, 2009.

[144] PE Gold. Acetylcholine modulation of neural systems involved in learning and memory. *Neurobiology of Learning and Memory*, 80:194–210, 2003.

[145] M Sarter, ME Hasselmo, JP Bruno, and B Givens. Unraveling the attentional functions of cortical cholinergic inputs: interactions between signal-driven and cognitive modulation of signal detection. *Brain Research Reviews*, 48:98–111, 2005.

[146] DJ Watts and SH Strogatz. Collective dynamics of 'small-world' networks. *Nature*, 393:440–442, 1999.

[147] J Dubnau, AS Chiang, and T Tully. Neural substrates of memory: From synapse to system. *Journal of Neurobiology*, 54:238–253, 2003.

[148] A Treves and E Rolls. Computational analysis of the role of the hippocampus in memory. *Hippocampus*, 4:374–391, 1994.

[149] P Riekkinen, J Kuitenen, and M Riekkinen. Effects of thalamic and nucleus basalis infusions of nicotine on cortical EEG. *Neuroreport*, 6:1625–1628, 1995.

[150] M Steriade. Acetylcholine systems and rhythmic activities during the waking-sleep cycle. *Progress in Brain Research*, 145:179–196, 2004.

[151] SR Williams, TI Toth, JP Turner, SW Hughes, and V Crunelli. The 'window' component of the low threshold Ca^{2+} current produces input signal amplification and bistability in cat and rat thalamocortical neurones. *Journal of Physiology*, 505:689–705, 1997.

[152] SW Hughes, DW Cope, KL Blethyn, and V Crunelli. Cellular mechanisms of the slow (< 1 Hz) oscillation in thalamocortical neurons in vitro. *Neuron*, 33:947–958, 2002.

[153] E Perez-Reyes. Molecular physiology of low-voltage-activated T-type calcium channels. *Physiological Reviews*, 83:117–161, 2003.

[154] SK Esser, SL Hill, and G Tononi. Sleep homeostasis and cortical synchronization: I. Modeling the effects of synaptic strength on sleep slow waves. *Sleep*, 30:1617–1630, 2007.

[155] VV Vyazovskiy, BA Riedner, C Cirelli, and G Tononi. Sleep homeostasis and cortical synchronization: II. a local field potential study of sleep slow waves in the rat. *Sleep*, 30:1631–1642, 2007.

[156] BA Riedner, VV Vyazovskiy, R Huber, M Massimini, S Esser, M Murphy, and G Tononi. Sleep homeostasis and cortical synchronization: III. a high-density EEG study of sleep slow waves in humans. *Sleep*, 30:1643–1657, 2007.

[157] SL Rogers, MR Farlow, RS Doody, R Mohs, LT Friedhoff, B Albala, B Baumel, G Booker, J Dexter, M Farmer, JP Feighner, S Ferris, B Gordon, DG Gorman, G Hanna, LE Harrell, R Hubbard, J Kennedy, J McCarthy, DW Scharre, F Schaerf, L Schneider, B Seltzer, A Siegal, SR Stark, A Strauss, and TM Walshe. A 24-week, double-blind, placebo-controlled trial of donepezil in patients with alzheimer's disease. *Neurology*, 50:136–145, 1998.

[158] EV Lubenov and AG Siapas. Decoupling through synchrony in neuronal circuits with propagation delays. *Neuron*, 58:118–131, 2008.